MÖSSBAUER SPECTROSCOPY

OF

^{57}Fe-DOPED TRANSITION METAL COMPOUNDS

A thesis

submitted for the Degree

of

Doctor of Philosophy in Physics

at the

University of Canterbury

Christchurch, New Zealand

by

Md. Abu Saeed Khan

University of Canterbury

1981

To

Sakib and Swapna

ABSTRACT

Mössbauer absorption spectra of ^{57}Fe doped into polycrystalline samples of MnS_2, $MnSe_2$ and $MnTe_2$ are measured as a function of temperature between 5K and 298K. The hyperfine spectra of these samples are of the pure Fe^{2+} state, and are analysed by diagonalizing the combined magnetic dipole and electric quadrupole Hamiltonian matrix of the first excited state of ^{57}Fe. The variation of isomer shift with temperature is analysed on the Debye model. Also the temperature dependences of the magnetic hyperfine fields and their directions are interpreted in terms of crystal-field theory and of the known spin directions of the Mn^{2+} host ions. Finally, the variation of antiferromagnetic transition temperature and of the spin direction as a function of iron concentration in $MnSe_2$ are investigated.

ACKNOWLEDGEMENTS

I wish to express my gratitude to Professors A.G. McLellan, B.G. Wybourne and W.L. Jones for accepting me as a postgraduate student and for providing me with a Teaching Fellowship position.

I am particularly grateful to my supervisor Dr John Ward for his assistance, advice, interest, and patience during the course of this research.

I would like to thank my associate supervisor Dr Valda McCann for her assistance, useful suggestions and helpful discussions.

I would also like to thank:

- My fellow postgraduate colleagues; Chris Tomblin, for various help, and Robin Pollard, for many discussions and for allowing me to use some of his programs, including the program which plotted the spectra in this thesis;
- Ross Ritchie and John de Voil for technical assistance;
- Tom Walker for supplying cryogenic refrigerants;
- Mrs van der Borch for tracing some of the diagrams;
- Mrs Janet Warburton for the neat typing of this thesis; and
- Jahangirnagar University, Dacca, Bangladesh for granting my study leave.

Finally I thank my family and wife for their support and understanding.

CONTENTS

LIST OF FIGURES

LIST OF TABLES

CHAPTER 1

INTRODUCTION

1.1 INTRODUCTION TO PRESENT STUDY

This research work involves the investigation of the hyperfine interactions of ^{57}Fe-doped polycrystalline samples of MnS_2, $MnSe_2$ and $MnTe_2$ using Mössbauer spectroscopy. In each case the divalent ferrous ions substitute for the divalent cations and experience a crystalline field of $\bar{3}$ symmetry.

The temperature dependence of the isomer shift data was analysed on the Debye model and the Debye temperatures of the samples were determined.

The temperature dependences of the magnetic hyperfine fields together with the hyperfine angles were analysed in terms of crystal-field theory and values of crystal-field parameters were determined.

The variation of Néel temperature as a function of iron-concentration in $MnSe_2$ was determined; iron-concentration dependent Mössbauer spectra of $MnSe_2$ at 20K were recorded and analysed.

The major motivation of this work was to investigate the Mössbauer hyperfine interactions in these crystals, to check the spin directions determined by neutron diffraction[1] and previous Mössbauer studies[2,3], and to see whether the Mössbauer parameters could be explained using crystal-field theory.

1.2 CRYSTAL STRUCTURE

Elliott[4] determined the crystal structure of each of these compounds by X-ray diffraction. These compounds crystallize with the pyrite structure and the space group is Pa3, a NaCl-like arrangement of Mn^{2+} and X_2^{2-} groups (where X is S, Se or Te) with the axes of the X_2^{2-} groups parallel to the various body-diagonals, i.e., the cations form an fcc lattice and the axis of each anion pair lies along one of the four <111> directions, which also is the direction of the $\bar{3}$ principal symmetry axis at the Mn^{2+} sites. Each cation is surrounded by six anions forming an octahedron, while each anion is tetrahedrally coordinated to three cations and one anion[1] as shown in Fig. 1.1.

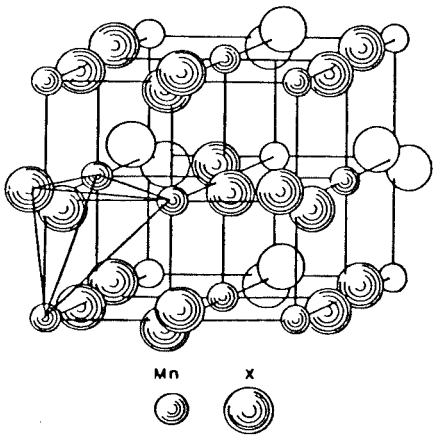

Figure 1.1 The pyrite structure.

The positions of the Mn^{2+} ions are at (000), $(\frac{1}{2}\frac{1}{2}0)$, $(\frac{1}{2}0\frac{1}{2})$ and $(0\frac{1}{2}\frac{1}{2})$ and the X ions are at $\pm$(uuu), $\pm(u+\frac{1}{2}\ \frac{1}{2}-u\ \bar{u})$, $\pm(\bar{u}\ u+\frac{1}{2}\ \frac{1}{2}-u)$ and $\pm(\frac{1}{2}-u\ \bar{u}\ u+\frac{1}{2})$. Elliott's values of the position parameter u are included in Table 3.4 together with other crystallographic data.

1.3 MAGNETIC SPIN ARRANGEMENTS

The magnetic properties of the manganese dichalcogenides have been studied by many investigators over the last two decades. The low temperature antiferromagnetic structures of MnS_2, $MnSe_2$ and $MnTe_2$ were deduced by Hastings et al.[1] at 4.2K from neutron diffraction data, assuming a collinear (single axis) spin arrangement. They concluded that, in MnS_2, the manganese ion has four parallel and eight antiparallel nearest neighbour spins and four parallel and two antiparallel second nearest neighbour spins; it also has sixteen parallel and eight antiparallel third nearest neighbour spins. This spin arrangement is consistent with ordering of the third kind.[5] The spin axis was deduced to be along [100]. The magnetic unit cell of this crystal is equal to twice the chemical unit cell. The spin structure can be regarded as a stacking of antiferromagnetic (200) planes in the sequence $AB\bar{A}\bar{B}$ ..., the bar indicating spin reversel (see Fig. 1.2).

In $MnSe_2$, a mixture of third and first kind of spin ordering was deduced. This arrangement has the same nearest neighbour spin directions as in MnS_2 i.e. four parallel and eight antiparallel spins. However, one third of the cations have four parallel and two antiparallel second nearest neighbour spins and two-thirds have five parallel and one antiparallel second nearest neighbour spins. Of the third nearest neighbour spins, sixteen are parallel and eight antiparallel. The spin direction of $MnSe_2$ was deduced to be the same as MnS_2 i.e. along [100].

In this crystal the magnetic unit cell size is three times the chemical unit cell and this structure is given by the stacking sequence $AB\bar{A}\bar{B}\bar{A}BA...$ (Fig. 1.2), A and B as in MnS_2.

In $MnTe_2$ a spin arrangement of the 1st kind was deduced. This arrangement can be represented by an ABA... stacking sequence (Fig. 1.2). The exact direction of the spin axis could not be determined from the neutron diffraction data, but it was deduced to lie in the (001) plane.

Later work modified this picture for $MnTe_2$. Pasternak and Spijkervet[2] took ^{125}Te (35.6 keV transition) Mössbauer spectra in $MnTe_2$, and measured θ, the angle between the z principal axis of the electric field gradient at the Mössbauer nucleus (EFG), and the magnetic hyperfine field at the nucleus (H). The values obtained (near 30° at 4.2K, near 0° at 77.3K just below the Néel temperature (T_N)) were not consistent with the spin array described above. In a later paper, Hastings et al.[3] resolved this inconsistency between the Mössbauer and the neutron diffraction results, and suggested a revised non-collinear spin structure in $MnTe_2$ just below T_N. In this revised structure the magnetic and chemical unit cells are the same size, and the four Mn^{2+} ions in each unit cell have their spins pointing along one of the four <111> directions, i.e. along [111], $[1\bar{1}\bar{1}]$, $[\bar{1}1\bar{1}]$ and $[\bar{1}\bar{1}1]$ (Fig. 1.3).

This results in each Mn^{2+} ion having 12 nearest neighbour spins at an angle of $\cos^{-1}(-\frac{1}{3}) = 109.47°$, 6 second nearest neighbours with parallel spins, and 24 third nearest neighbour

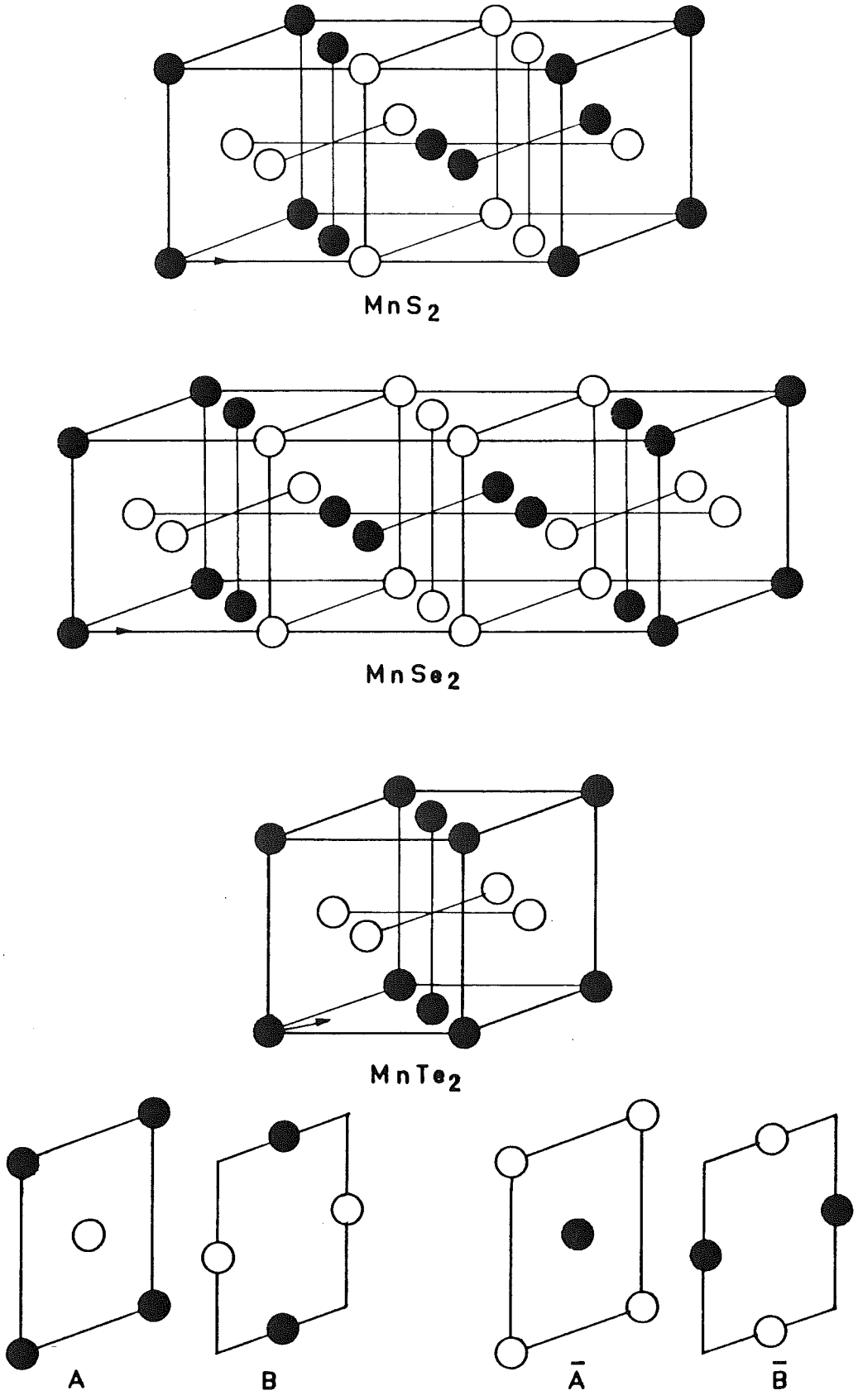

Figure 1.2 Magnetic structures of MnS_2, $MnSe_2$ and $MnTe_2$ and planes A,B,$\bar{A}$ and $\bar{B}$ as determined by Hastings et al.[1]. Black and white spheres represent opposite spin directions of the Mn^{2+} ions.

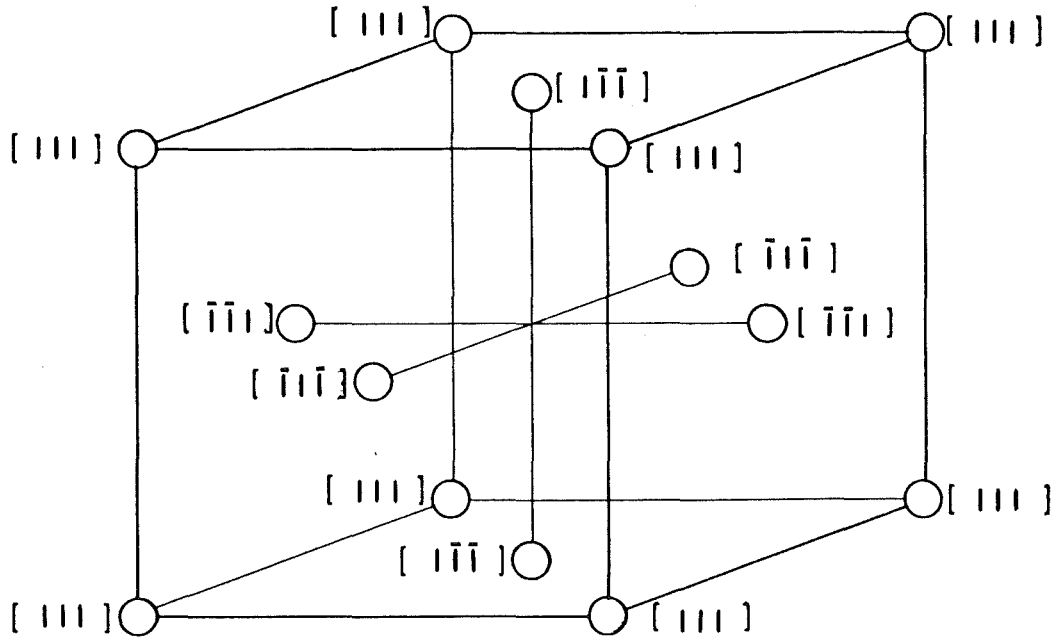

Figure 1.3 Magnetic structure of $MnTe_2$ as determined by Pasternak et al.[2] and Hastings et al.[3].

spins also at 109.47°. At 4.2K, where θ is ~ 30°, no unique spin structure could be determined; however, having the spins along [110],[1$\bar{1}$0], [$\bar{1}$10] and [$\bar{1}\bar{1}$0], or other crystallographically equivalent directions, would give a θ of $\cos^{-1}(\sqrt{2/3}) = 35.26°$.

The main features of Pasternak et al's results were confirmed by Nishihara and Ogawa[6], who measured ^{125}Te Mössbauer spectra of $MnTe_2$ with improved resolution. They also observed that at 60K H and the quadrupole splitting (QS) change discontinuously with increasing temperature and that θ increases from 23° at 4K to 30° at 60K and then decreases to 0° at 70K. They suggested that the most likely cause of this behaviour is that the positional parameter u of the crystal lattice changes at 60K in $MnTe_2$.

1.4 REVIEW OF OTHER RELEVANT PROPERTIES

1.4.1 Néel Temperature and Order of the Transition

In this section we briefly summarize the measurements of T_N, and deductions about the order of the transition, in Table 1.1.

The order of a transition can be inferred from e.g. the specific heat versus temperature curve. A 1st-order transition is very sharp (Fig. 1.4) and is accompanied by the emission of latent heat; in a 2nd-order transition the heat is emitted over a finite range of temperature.

Table 1.1 Néel temperatures and order of the transition in MnS_2, $MnSe_2$ and $MnTe_2$.

Compound	T_N,K	T_B,K	Order	Method	Reference
MnS_2	47.93			C_p	(7)
	47.6,48.1	65	1st	ND	(8)
	48.2			χ	(9)
$MnSe_2$	47.4		1st	χ,α	(10)
	$51 \leqslant T_N \leqslant 56$	90	1st(?)	ND	(11)
$MnTe_2$	87			ρ	(12)
	83			C_p	(7)
	83.8			Mössbauer	(13)
	87.2			χ	(9)
	85			ρ,χ	(6)
	87			χ	(14)

T_B = expected transition temperature, extrapolated from the low-temperature values of critical parameters.

T_N = actual transition temperature (Néel temperature)

C_p = heat capacity

ND = neutron diffraction

χ = magnetic susceptibility

ρ = electrical resistivity

α = linear thermal expansion coefficient.

A critical parameter such as the exchange field or ND line intensity follows a Brillouin function right up to, or very close to, the transition temperature, if the transition is 2nd-order. If the transition is 1st-order the critical parameter follows the function at low temperatures and appears to be heading for a zero value at the temperature T_B where the Brillouin function (Appendix C) goes to zero; instead, the quantity goes rapidly to zero before this temperature is reached, the actual transition temperature T_N being $< T_B$ (see Fig. 1.5).

MnS_2

Hastings et al.[8] showed from a ND study that the transition is 1st-order with about ½°C magnetic hysteresis, that is, magnetic order appeared at ~ 47.6K on cooling and disappeared at 48.1K on warming. The temperatures obtained by the other two groups listed in Table 1.1 are consistent with these values.

$MnSe_2$

Corliss et al.[11] did not measure T_N but presented a transition range and suggested that the magnetic transition was very likely first order. Recently Itoh and Miyahara[10] measured T_N = 47.4K from the magnetic susceptibility and the linear thermal expansion coefficient of this crystal with good resolution and determined a 1st-order transition.

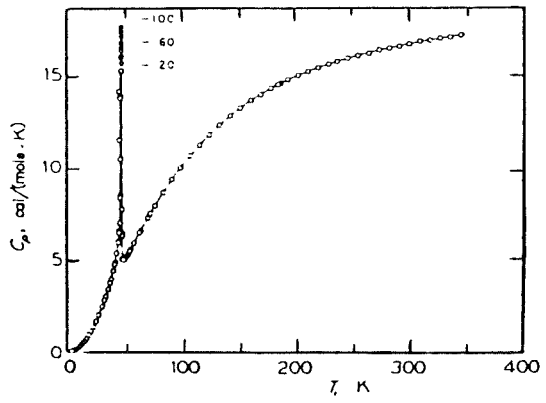

Figure 1.4 First-order magnetic phase transition in MnS_2 at T_N [7].

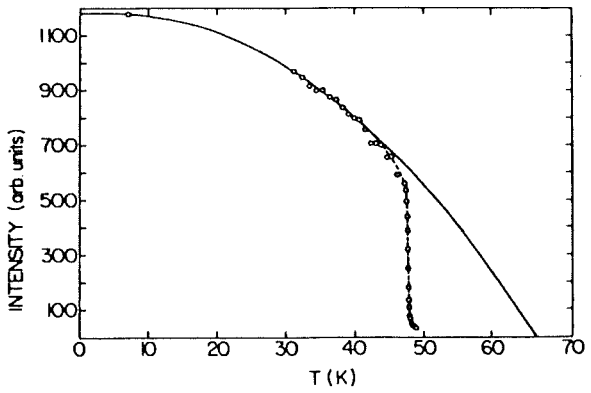

Figure 1.5 Temperature dependence of the intensity of the $(\frac{1}{2}01)$ antiferromagnetic reflection in MnS_2 [8]. Solid curve is the Brillouin function for $S = \frac{5}{2}$.

$MnTe_2$

Different groups observed T_N at various temperatures between 83 and 87.2K in this crystal. Westrum and Gronvold[7] used an under - stoichiometric sample. Pasternak's[13] extrapolation T_N value, taken from the temperature dependences of the normalized magnetic field, perhaps could be greater than the value he quoted (83.8K). Nishihara and Ogawa[6] did not supply details of their determination. Sawaoka and Miyahara's[12] result is doubtful because of their exceptionally high lattice parameter. Okada and Miyadai's [14] experimental points are far apart. Considering these facts Lin and Hacker's[9] T_N = 87.2K is more acceptable than others.

1.4.2 Exchange Constants

van Kalkeren et al.[15] published two papers on magnetic ordering in manganese pyrites. In their first paper, exchange constants for nearest neighbour (J_1), second nearest neighbour (J_2) and third nearest neighbour (J_3) interactions were calculated from a 3-ion model i.e. in terms of $Mn^{2+}-X_2^{2-}-Mn^{2+}$ indirect interactions. These parameters were in fair agreement with experimental values, but their calculated T_N values predicted antiferromagnetic ordering of the second kind for all three compounds, which was not in agreement with what was observed (3rd kind for MnS_2, mixture of 1st and 3rd kind for $MnSe_2$ and 1st kind for $MnTe_2$). In their second paper they considered indirect exchange interactions in a 4-ion model i.e., $Mn^{2+}-X_2^{2-}-X_2^{2-}-Mn^{2+}$ and calculated J_1 and J_2 (J_3 had been found to be much less than J_1 and J_2 and

was therefore ignored in their second paper). This time, their calculated T_N predicted the correct magnetic ordering, however, these exchange constants were quite different from the experimental values. The experimental and theoretical results are summarized in Table 1.2. Experimental values can be derived from the values of T_N and χ using the molecular field model.

Table 1.2 Calculated and experimental values of Mn^{2+}-Mn^{2+} exchange constants for MnS_2, $MnSe_2$ and $MnTe_2$.

Compound		Exchange constants (K)			Reference
		J_1	J_2	J_3	
MnS_2	exp.	-5.73	-6.06		(9)
	calc.	-2.8 & -3.3	-0.2 & -0.4		(15)
$MnSe_2$	calc.	-2.8 & -3.5	0		(15)
$MnTe_2$	exp.	-6.44	-1.2		(9)
	exp.	-7.1	1.3		(14)
	exp.	-4.5	-1	-1	(16)
	calc.	-3.0 & -3.8	0.3 & 0.4		(15)

1.5 STRUCTURE OF THE THESIS

Chapter 2 consists of two major sections. The first section contains an account of the theory of Mössbauer spectroscopy; this includes the Hamiltonian interactions appropriate for ^{57}Fe and their associated parameters. The second section of this chapter contains a summary of the crystal-field theory needed to interprete the results of Mössbauer spectroscopy of an Fe^{2+} ion in a trigonal environment.

The experimental details and instruments involved for Mössbauer spectroscopy are described in Chapter 3; sample preparation is also included in this chapter.

In Chapter 4 representative Mössbauer spectra together with the results are presented and the data are analysed in terms of the crystal-field theory presented in Chapter 2.

Finally, the results are summarized and suggestions for further work are given in Chapter 5.

CHAPTER 2

THEORY

2.1 INTRODUCTION

This chapter describes particular aspects and theories of Mössbauer spectroscopy and crystal-field calculations which provide a foundation for the discussion presented in the later chapters.

2.2 THEORY OF MÖSSBAUER SPECTROSCOPY

2.2.1 Introduction

Mössbauer spectrocopy is based on the resonance absorption of a γ-ray photon by a nucleus, as discovered by R.L. Mössbauer in 1957[17]. Since then it has become a valuable technique in various fields of investigation. The salient feature of this γ-ray photon is its very narrowly defined energy spectrum that can be used to resolve minute energy differences. This is one of the most useful techniques for investigating the hyperfine fields in solids. The number of lines in the Mössbauer spectrum, their positions and their relative intensities, are determined by the hyperfine interactions of the nucleus with its surrounding electrons. References (18) to (24) are general reference books covering all aspects of Mössbauer spectroscopy.

2.2.2 Nuclear Emission and Absorption of Gamma-rays

It is well known that when a nucleus decays from an excited state E_e to its ground state E_g, its excess energy can be emitted in the form of a γ-ray photon. On emitting this γ-ray, the nucleus recoils with energy E_R, thus the γ-ray has less than the expected energy $(E_e - E_g)$.

When an atom of mass M moving with velocity V_x, emits a γ-ray of energy E_γ in the +x direction, then conservation of momentum gives,

$$MV_x = M(V_x - V_R) + E_\gamma/c$$

where V_R is the change in velocity of the atom.

In this case

$$\text{Initial kinetic energy} = \tfrac{1}{2}MV_x^2$$

$$\text{Final kinetic energy} = \tfrac{1}{2}M(V_x - V_R)^2$$

So conservation of energy gives

$$\text{change in K.E} = \tfrac{1}{2}MV_R^2 - MV_xV_R$$

$$= E_R - E_D$$

where

$E_R = \tfrac{1}{2}MV_R^2$ is called the recoil energy and

$E_D = MV_xV_R$ is a velocity dependent Doppler energy.

If we assume a Maxwellian distribution of V_x values, the average energy loss on γ-emission is E_R. For the inverse process, where a γ-ray is absorbed by a nucleus, a further increment of energy E_R is necessary since the γ-ray must provide both the nuclear excitation energy and the recoil energy of the absorbing atom i.e. it must provide $(E_t + E_R)$, where E_t is the nuclear transition energy $(E_e - E_g)$.

The recoil energy E_R shifts the emitted photon energy from E_t to E_γ, and E_D results in a thermal broadening of the line if the atom's velocity V_x is the result of thermal excitation (Fig. 2.1).

For a random thermal motion, the mean kinetic translational energy of an atom is

$$\bar{E}_k = \frac{3}{2}kT = \frac{1}{2}M\bar{V}_x^2$$

Hence

$$\sqrt{\bar{V}_x^2} = \sqrt{\frac{3kT}{M}} = \sqrt{\frac{2\bar{E}_k}{M}}$$

is the root mean square velocity of the atom in the direction of observation;

k is the Boltzmann constant,

and

T is the absolute temperature.

So the mean Doppler broadening

$$\bar{E}_D = MV_R\sqrt{\bar{V}_x^2}$$

$$= 2\sqrt{\bar{E}_K E_R} \quad .$$

Hence the Doppler broadening is proportional to the square root of the product of the thermal energy $\bar{E}_K$ and the recoil energy E_R. For ^{57}Fe, $E_\gamma = 14.4$ keV and $M = 56.935$ u; this gives $E_R = 1.96 \times 10^{-3}$ eV and $\bar{E}_D \simeq 1.40 \times 10^{-2}$ eV at 300K.

2.2.3 Heisenberg Natural Linewidth

The Heisenberg uncertainty relation between energy and time determines the γ-ray energy distribution. The lifetime of an excited state can be expressed in terms of its width. According to the energy-time uncertainty relation, since a nucleus survives in an excited state only for an average life-time τ of the state, then its energy in the state can be specified only within an energy range Γ_s known as the natural linewidth, satisfying approximately the relation

$$\Gamma_s = \frac{\hbar}{\tau} \qquad (2.1)$$

where $\hbar = \frac{h}{2\pi}$, h is Planck's constant. Excited states are, therefore, not perfectly sharp; instead, they are spread over an energy range of width Γ_s. A detailed treatment shows that eqn. (2.1) is actually satisfied exactly, providing Γ_s is the full-width at half-maximum of the energy profile of the state.

The first excited state of ^{57}Fe (14.4 keV) has a half-life $t_{\frac{1}{2}}$ = 97.7 ns. Thus the natural line-width is $\Gamma_s = 4.67 \times 10^{-9}$ eV, which is 10^6 - 10^7 times smaller than the values of E_R and $\bar{E}_D$ for a free atom as shown in Fig. 2.1.

2.2.4 Recoil Free Fraction

In section 2.2.2 it is shown that since the γ-rays have a momentum equal to E_γ/c, the recoil energy loss $E_R = E_\gamma^2/2Mc^2$ = 1.96×10^{-3} eV for ^{57}Fe. This recoil energy is supplied from the initial excitation energy E_e of the nucleus. Although E_R is only a tiny fraction of the γ-ray energy (one part in 10^7 for ^{57}Fe), it is much larger than the width of the nuclear level, typically 10^{-7} eV. Thus, the γ-rays emitted from a freely recoiling nucleus are far too low in energy to be resonantly absorbed by a nucleus of the same type initially at rest. Mössbauer spectroscopy overcomes this difficulty by binding the nucleus in a solid, where the recoil energy loss can be eliminated for a fraction of the decays. This recoilless or recoil free fraction of the source of the γ-rays is denoted by f_s and its value can be as high as 0.7 or 0.8 in favourable cases.

Similarly, if the absorbing nuclei are bound in a solid material, a fraction f_a of the absorptions are recoilless. It is possible to relate f to the vibrational properties of the crystal lattice by[20]

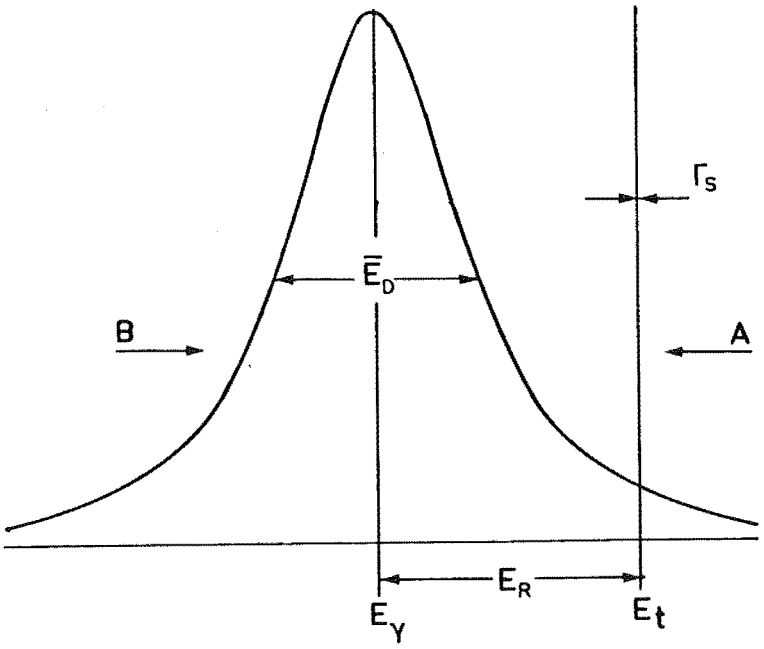

Figure 2.1 The statistical energy distribution of the emitted γ-ray showing the interrelationship of E_γ, E_t, E_R and $\bar{E}_D$. Γ_s is << E_R and $\bar{E}_D$; the emitted γ-ray spectrum is therefore represented by a line only.
Curve A: γ-ray emission spectrum from fixed ^{57}Fe nuclei.
Curve B: γ-ray emission spectrum from ^{57}Fe nuclei moving with thermal velocities at 300K.

$$f = \exp\left(\frac{-4\pi^2\langle x^2\rangle}{\lambda^2}\right) = \exp\left(\frac{-E_\gamma^2\langle x^2\rangle}{(\hbar c)^2}\right)$$

where λ is the wavelength of the γ-ray (0.863 Å for the 14.4 keV energy of ^{57}Fe) and $\langle x^2\rangle$ is the mean square vibrational amplitude of the emitting or absorbing nucleus in the solid.

2.2.5 Production and General Features of a Mössbauer Spectrum

A Mössbauer absorption spectrum is produced by counting the γ-rays, that pass through an absorber containing Mössbauer nuclei (^{57}Fe in the case of this research), as a function of the γ-ray energy. Since the line widths for recoilless emission and absorption are so small, energy variation can be achieved simply by moving the source (at v mm s^{-1}, say) towards the absorber, thus Doppler shifting the γ-ray energies by $E_\gamma(v/c)$, c being the velocity of light.

A schematic diagram of the apparatus and the spectrum produced is shown in Fig. 2.2, taken partly from reference 23. The curves shown are the recoilless emission spectrum of the source at zero velocity I(E,0), the probability of a recoilless absorption by the absorber $\sigma(E)$, and the resultant spectrum recorded in the detector. The total γ-ray intensity absorbed is given by $\int_{-\infty}^{\infty} I(E,v)\sigma(E)dE$ and will be small unless curves I(E,v) and $\sigma(E)$ are brought into coincidence. It can be shown[23] that the Mössbauer spectrum line width is given by $\Gamma = \Gamma_s + \Gamma_a$ if source and absorber are both thin.

It will be shown in the following sections that the Mössbauer spectra at and just below room temperature consist

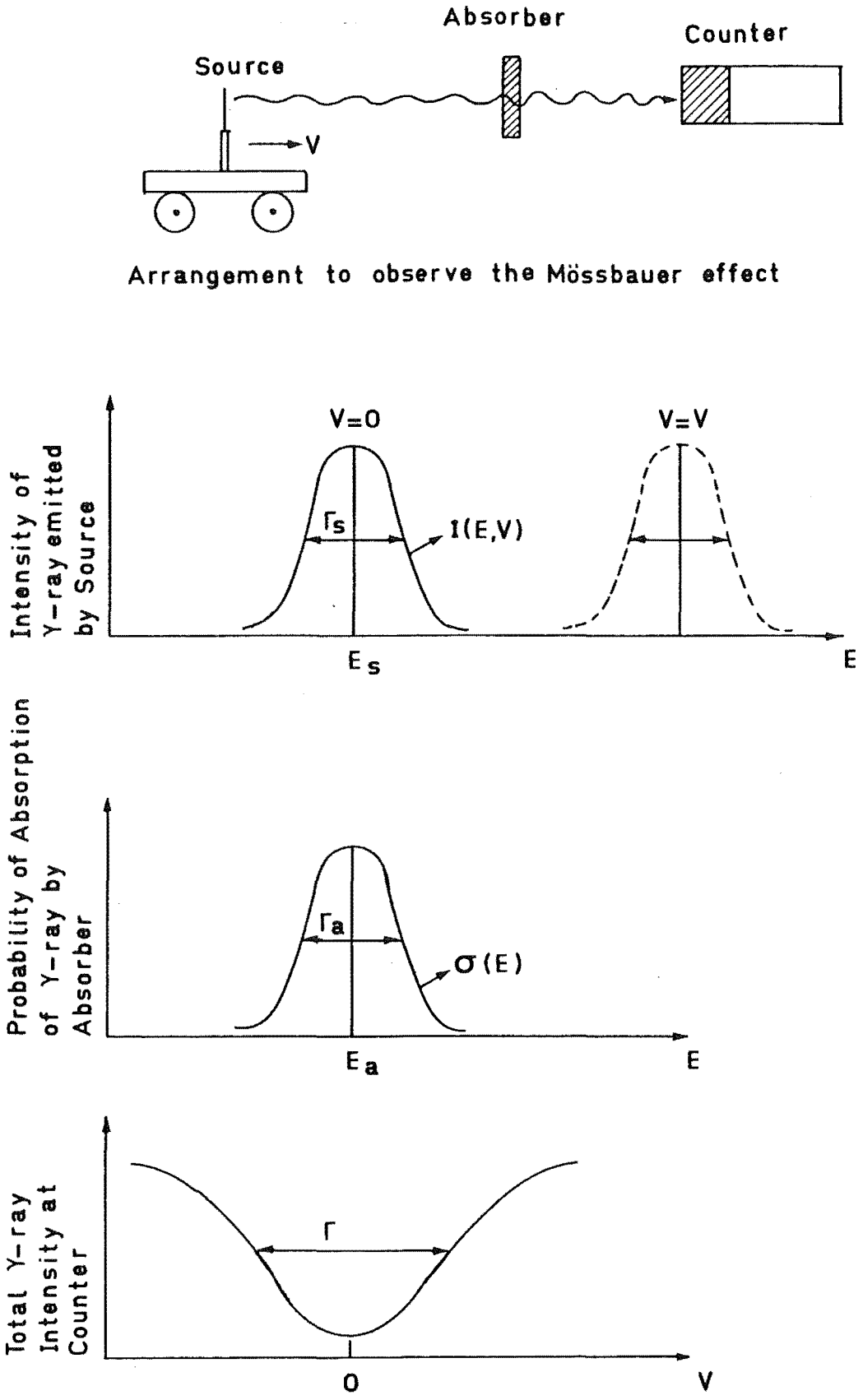

Figure 2.2 Mössbauer effect experimental setup, emission and absorption lines, and velocity spectrum in a Mössbauer transmission experiment.

of two lines with equal width and depth for all polycrystalline homogeneous samples used in this study. This spectrum is referred to as a "pair" in the rest of this thesis. Below the magnetic transition temperature the spectrum consists of a group of eight lines of different intensity. These are referred to as a "bunch" of lines in this thesis.

2.2.6 Isomer Shift

In Mössbauer spectroscopy a change in the electronic environment of a nucleus causes a change in the energy of the ground and excited states. This phenomenon is known as the isomer shift (IS) or the centre shift.

If the s-electron density is different for the absorber and source, the difference in γ-ray energies $E_a - E_s$ is defined as the isomer shift[49]

$$IS = E_a - E_s = \frac{2}{5} \pi Z e^2 (R_e^2 - R_g^2) [|\psi(0)_a|^2 - |\psi(0)_s|^2]$$

where R_e and R_g are the nuclear radii of the excited and ground states and $|\psi(0)_a|^2$ and $|\psi(0)_s|^2$ are the total s-electron densities at the nucleus for absorber and source respectively.

If IS > 0 a positive velocity (towards the absorber) has to be applied to the source to achieve resonance. Isomer shifts in this thesis are expressed in terms of the E_s of a source in natural Fe at 298K.

2.2.7 Electric Quadrupole Interaction

The nuclear energy levels are split by the quadrupole coupling between the nuclear electric quadrupole moment and the electric field gradient (EFG) at the nucleus; this is known as the quadrupole interaction.

The Hamiltonian describing the quadrupole interaction is[20]

$$\mathcal{H}_Q = \frac{e^2qQ}{4I(2I-1)} [(3I_z^2 - I(I+1) + \frac{\eta}{2}(I_+^2 + I_-^2)]$$

where

e is the charge of proton,

eQ is the nuclear electric quadrupole moment,

eq is one of the principal components of the EFG at the nucleus, V_{zz}, and

η is the asymmetry parameter of the EFG $(V_{xx} - V_{yy})/V_{zz}$ (V_{ii} is defined in sec. 2.2.7.1)

I is the nuclear total angular momentum quantum number,

$I_\pm = I_x \pm iI_y$ are the nuclear raising and lowering operators

I_x, I_y and I_z are the operators for the nuclear total angular momentum components.

The eigenvalues of the Hamiltonian are[20]

$$E_Q = \frac{e^2qQ}{4I(2I-1)} [3m_I^2 - I(I+1)](1 + \eta^2/3)^{\frac{1}{2}}$$

where m_I = I, I-1, ... -I is the nuclear magnetic spin quantum number. The effect of the electric quadrupole interaction in ^{57}Fe is depicted in Fig. 2.3. The excited state ($I = \frac{3}{2}$) is split into two doubly degenerate substates $|\frac{3}{2}, \pm\frac{3}{2}>$ and $|\frac{3}{2}, \pm\frac{1}{2}>$ of energies $E_Q = \pm\frac{1}{4} e^2qQ(1 + \eta^2/3)^{\frac{1}{2}}$. The ground state has spin $I = \frac{1}{2}$ and is spherically symmetric and therefore has no quadrupole moment. If $\eta = 0$ (axial EFG; this is the case with the compounds studied in this research at all temperatures above T_N), the difference in energy between the two substates is

$$QS = E_Q(\pm\tfrac{3}{2}) - E_Q(\pm\tfrac{1}{2}) = \frac{e^2qQ}{2} .$$

2.2.7.1 Electric Field Gradient

The EFG at the nuclear site originates from the electric charges surrounding the nucleus. There are two principal sources of this external charge which contribute to the total EFG:

(a) non-cubic electron distribution directly associated with the Mössbauer atom or ion, usually called the valence electron contribution.

(b) charges on other ions, surrounding the Mössbauer atom in non-cubic symmetry, usually denoted as the ligand or lattice contribution.

The potential V at the Mössbauer nucleus due to a point charge q located at a distance $r = (x^2 + y^2 + z^2)^{\frac{1}{2}}$ is

$$V = q/r$$

The electric field $\underline{E}$ at the nucleus is the negative gradient of this potential - $\underline{\nabla}V$ and finally the gradient of the electric field at the nucleus $\underline{\nabla}\underline{E}$ is given by

$$EFG = \underline{\nabla}\ \underline{E} = -\ \nabla^2 V = -\begin{vmatrix} V_{xx} & V_{xy} & V_{xz} \\ V_{yx} & V_{yy} & V_{yz} \\ V_{zx} & V_{zy} & V_{zz} \end{vmatrix}$$

where

$$V_{ij} = \frac{\partial^2 V}{\partial_i \partial_j} \qquad (i,j = x,y,z)$$

Thus, the EFG is the negative second derivative of the potential at the nucleus of all surrounding electric charge.

Only five out of nine EFG parameters are independent, namely, three of the off-diagonal elements (because of the symmetric form of the EFG tensor i.e. $V_{xy} = V_{yx}$, etc.) and two diagonal elements, because they are related by Laplace's equation

$$V_{xx} + V_{yy} + V_{zz} = 0$$

It is laborious to work out the five independent elements. A unique set of axes known as 'the principal axes of the EFG tensor' can always be defined such that the off-diagonal elements are zero and the diagonal elements are ordered as

$$|V_{zz}| \geqslant |V_{yy}| \geqslant |V_{xx}|$$

Using the principal axes, the EFG tensor is described by two independent parameters, V_{zz} = eq and the asymmetry parameter η, defined by

$$\eta = \frac{V_{xx} - V_{yy}}{V_{zz}} \quad .$$

With the above conventions, η is restricted to $0 \leqslant \eta \leqslant 1$. For a three-, four- or six- fold axis passing through the Mössbauer nucleus, it can be shown that $V_{xx} = V_{yy}$[20] and therefore $\eta = 0$, and the EFG is called axially symmetric (or axial).

2.2.8 Magnetic Hyperfine Interaction

A nucleus with spin $I > 0$ has a nuclear magnetic moment $\underline{\mu}$, which can interact with a magnetic field $\underline{H}$ at the nucleus giving rise to a hyperfine splitting. The Hamiltonian describing the magnetic dipole interaction is[20]

$$\mathcal{H}_M = - \underline{\mu} \cdot \underline{H} = - g_N \mu_N \underline{I} \cdot \underline{H}$$

where

g_N is the nuclear g-factor ($\mu/I\mu_N$),

μ_N is the nuclear Bohr magneton ($e\hbar/2Mc$),

and

M is the mass of the proton.

The eigenvalues of the above equation are

$$E_M = - g_N \mu_N m_I H$$

The magnetic dipole interaction splits a nuclear state $|I>$ into 2I+1 equally spaced substates characterized by the nuclear magnetic quantum number $m_I = I, I-1, \ldots, -I$. The ground state of ^{57}Fe has a spin $I = \frac{1}{2}$ and the 14.4 keV excited state has $I = \frac{3}{2}$. Both states have a magnetic dipole moment and will therefore be split by magnetic interaction. The magnetic dipole splitting for ^{57}Fe is shown in Fig. 2.4. γ-ray transitions from the sublevels of the ground state to those of the excited state are subject to the selection rule $\Delta m_I = 0, \pm 1$ and give six lines altogether.

The most general case of a hf interaction is the combined effect of magnetic dipole and electric quadrupole interactions. In this case the sublevels are no longer equally spaced and the eigenstates of the Hamiltonian are mixtures of eigenstates of I_z so transitions between all excited substates and the ground substates are allowed.

Altogether, eight lines are observed (Fig. 2.4). The resultant Hamiltonian will be the sum of the individual Hamiltonians of the magnetic dipole and the electric quadrupole interaction.

$$\mathcal{H} = \mathcal{H}_Q + \mathcal{H}_M \tag{2.2}$$

where

$$\mathcal{H}_Q = \frac{e^2qQ}{4I(2I-1)} [3I_z^2 - I(I+1) + \frac{\eta}{2}(I_+^2 + I_-^2)]$$

and

$$\mathcal{H}_M = -g_N \mu_N H [I_z \cos \theta + (I_x \cos \phi + I_y \sin \phi) \sin \theta]$$

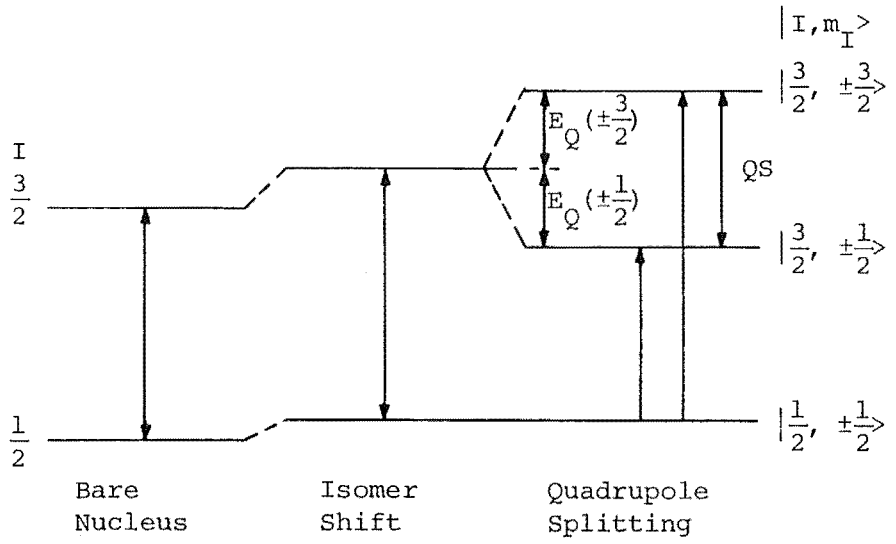

Figure 2.3 Isomer shift and quadrupole splitting for ^{57}Fe. E_Q is assumed to be > 0.

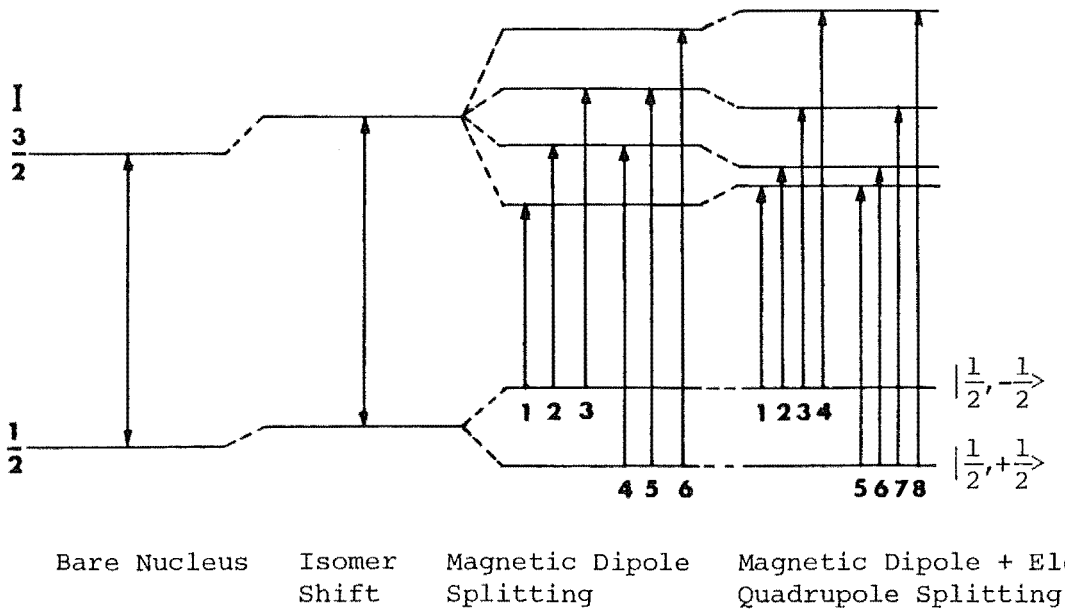

Figure 2.4 Magnetic dipole and the combined effect of the magnetic dipole and the electric quadrupole interaction in ^{57}Fe for H not parallel to z-axis.

Here the XYZ axes are the EFG principal axes and the magnetic field $\underline{H}$ is specified by the polar angle θ and the azimuthal angle ϕ as shown in Fig. 2.5.

The energy levels must be obtained by numerical diagonalisation of the matrix for $\mathcal{H}$. The matrix elements are listed in Appendix A.

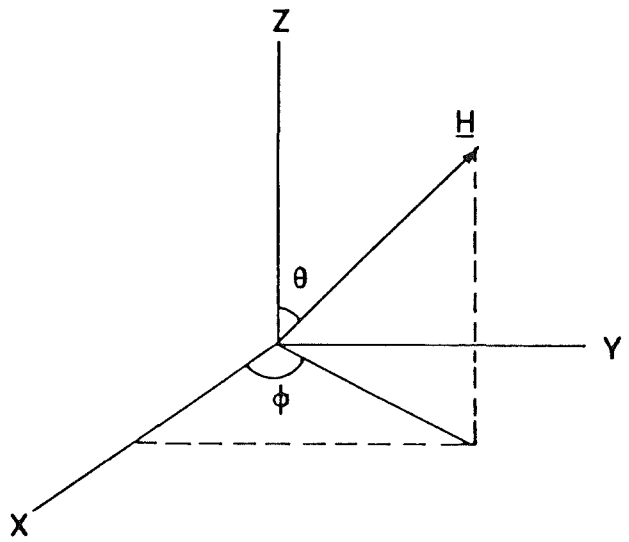

Figure 2.5 Direction of the magnetic field H relative to the EFG principal axes.

In this thesis magnetic field is denoted by H and expressed in units of tesla.

2.2.9 Relative Intensities of Absorption Lines

The interpretation of a Mössbauer spectrum requires knowledge of the relative intensities of its various absorptio lines. Once the energy levels of the magnetic or quadrupole Hamiltonian have been calculated, it is possible to calculate the line intensities from the theory of angular momentum coupling.

The relative intensity of a $|\frac{3}{2},m'>$ to $|\frac{1}{2},m">$ Mössbauer transition has been studied by Kündig[25], who has given formulae that we have used in our fitting program.
The expressions make use of the eigenvector coefficients $C^{m'}_{(\frac{3}{2},i)}$ for the excited state and $C^{m"}_{(\frac{1}{2},j)}$ for the ground state; the relative intensities for absorption of a photon travelling in the direction with polar and azimuthal angles (ϑ,φ) in the principal axis system is:

$$P(\vartheta,\varphi;\tfrac{3}{2},i;\tfrac{1}{2},j) = \Bigg| \sum_{m"=-\frac{1}{2}}^{+\frac{1}{2}} \sum_{m'=-\frac{3}{2}}^{+\frac{3}{2}} C^{m"*}_{(\frac{1}{2},j)} \; x$$

$$C^{m'}_{(\frac{3}{2},i)} \; <\tfrac{1}{2},m";L,m|\tfrac{3}{2},m'>X^{m}_{L}\Big|^2$$

where $<\ |\ >$ is the Clebsch-Gordon coefficient coupling the three vectors $\underline{I}_{\frac{1}{2}}$, $\underline{L}$ and $\underline{I}_{\frac{3}{2}}$. (L = 1 for ^{57}Fe since it is a magnetic dipole transition). The quantity X^{m}_{L} is a vector spherical harmonic which describes the photon polarization.

For a polycrystalline sample (such as all our samples were) P must be integrated over all possible ϑ and φ values. An explicit formula for the line intensities

$$P'(\tfrac{3}{2},i;\tfrac{1}{2},j) = \int_{\vartheta=0}^{\pi}\int_{\varphi=0}^{2\pi} P(\vartheta,\varphi;\tfrac{3}{2},i;\tfrac{1}{2},j)\sin\vartheta\, d\vartheta\, d\varphi$$

is given in Appendix A.

2.2.10 Energy Conversion of Mössbauer Spectrum

It has become customary to represent Mössbauer parameters of isomer shift, quadrupole splitting and line-width in terms of Mössbauer units or velocity units of mm s^{-1} and the conversion can be made through the equation:

$$\epsilon(eV) = \left(1 + \frac{v(mm\ s^{-1})}{c(mm\ s^{-1})}\right) E_{\gamma}(eV)$$

Here $\epsilon(eV)$ is the energy of a Mössbauer absorption line.

2.3 CRYSTAL-FIELD THEORY

2.3.1 Introduction

In the case of a free ion, the interaction among the 3d electrons results in the formation of electron states which can be assigned the spectroscopic term ^{2S+1}L, known as the free ion states, when the ion is part of a solid, the effect of the electrostatic potential of the neighbouring ions (known as the crystal-field) must be taken into account and this causes a splitting of the free ion levels.

The magnetic hyperfine field and the electric field gradient at a nucleus is produced by the surrounding electrons and ions. The origins of the variations with temperature of the magnetic hyperfine field and EFG can be explained through

the splitting of the electronic levels for different materials. After obtaining the energies of the electronic levels of ^{57}Fe ions in the crystals by diagonalizing the perturbation matrix, we can calculate the contributions of each level to the magnetic hyperfine field at the ^{57}Fe nucleus. We also want to compare our results of temperature dependences of the magnetic hyperfine field obtained from Mössbauer analysis with the results of this crystal-field calculation and this comparison will allow us to determine the crystal-field constants and the nuclear/electron interaction parameters.

For trigonal site symmetry the crystal-field V_{CF} can be separated into cubic and trigonal parts:

$$V_{CF} = V_{cubic} + V_{trig}$$

with $V_{cubic} >> V_{trig}$. According to Hund's rule a free Fe^{2+} ion belongs to the $3d^6$ configuration with a ^5D ground state. The cubic potential term splits this state into doublet (E_g) and triplet (T_{2g}) substates with energy separation $\sim 10^4$ cm^{-1}[26,27]. Due to this large separation the upper states are not populated at ordinary temperatures and so their contribution to the magnetic hyperfine field and EFG can be neglected[26]. The splitting due to the trigonal field is 200 cm^{-1} - 300 cm^{-1} for the compounds studied (Fig. 2.6).

The T_{2g} orbital states are to be used as basis states and can be written for trigonal symmetry as[27]

$$|\psi_{+1}> = -\left[\sqrt{\frac{2}{3}}\,|2,-2> + \sqrt{\frac{1}{3}}\,|2,1>\right]$$

$$|\psi_{0}> = |2,0>$$

$$|\psi_{-1}> = \sqrt{\frac{2}{3}}\,|2,2> - \sqrt{\frac{1}{3}}\,|2,-1>$$

The state $|\psi_{+1}>$ is the negative of that given in ref. 27. This was changed for computational convenience as the matrices for L_i (i = x,y,z) in the basis given above are formally the same as those of $-L_i'$ (i = x,y,z) in the basis $|L'M_L'>$ where L' = 1. The subscript on the ψ's is the value of M_L' for the corresponding state in the $|L'M_L'>$ basis.

Considering the ionic ground state spin S = 2, the T_{2g} level has a degeneracy of 15, with wave functions $\psi_i\chi_j$, (i = 0, $\pm$1; j = 0, $\pm$1, $\pm$2). With this representation we find the eigenfunctions and eigenvalues of the perturbation Hamiltonian,

$$\mathcal{H}' = \mathcal{H}_{trig} + \mathcal{H}_{s.o} + \mathcal{H}_{ex}$$

The terms in $\mathcal{H}'$ are defined in the following sections. The energy levels resulting from these interactions for $MnTe_2$ are shown in Fig. 2.6.

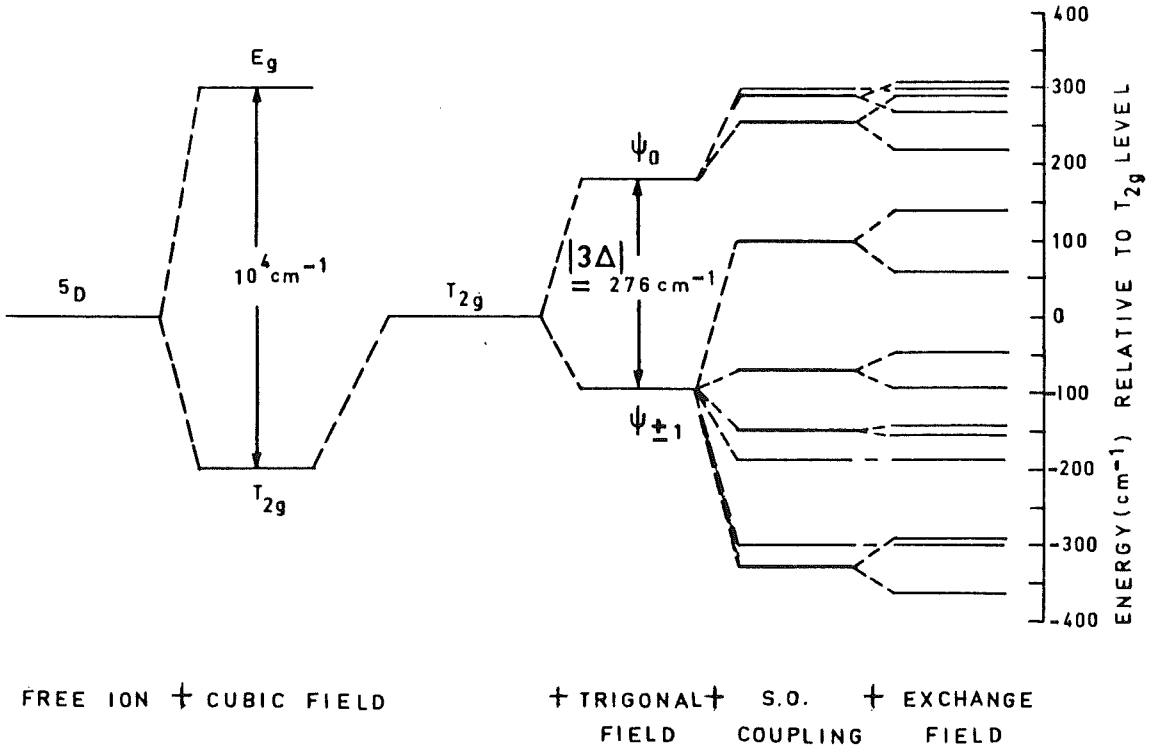

Figure 2.6 Energy levels resulting from trigonal field, spin-orbit coupling and exchange field parallel to the trigonal axis for $MnTe_2$.

2.3.2 Trigonal Crystal-Field - $\mathcal{H}_{trig}$

The trigonal crystal-field potential can be represented as $V_{trig} \propto 3z^2-r^2$ and the matrix elements found in terms of equivalent operators[28,29]

$$\mathcal{H}_{trig} \propto 3L_z^2 - L(L+1) = \Delta[L_z^2 - \tfrac{1}{3} L(L+1)]$$

The effect of $\mathcal{H}_{trig}$ considered by itself is to split the T_{2g} level into two levels - an orbital doublet ($\psi_{\pm 1}$) and orbital singlet (ψ_0) - which are separated by an energy of $|3\Delta|$.

2.3.3 Spin-Orbit Coupling - $\mathcal{H}_{s.o}$

The spin-orbit coupling is the product of total spin and orbital angular momenta and has the form $\lambda \underline{L}.\underline{S}$ with the spin-orbit coupling parameter λ being the product of the free-ion value λ_o ($\lambda_o = -103$ cm^{-1} for a free Fe^{2+} ion) and a covalency factor α^2, which is decreased below 1.0 due to the covalency effect.

$$\mathcal{H}_{s.o} = \lambda \, \underline{L}.\underline{S} = \alpha^2\lambda_o[L_zS_z + \tfrac{1}{2}(L_+S_- + L_-S_+)]$$

where L_z and S_z are the projections of $\underline{L}$ and $\underline{S}$ along z-axis and $L_\pm$ and $S_\pm$ are the orbital and spin raising and lowering operators.

2.3.4 Exchange Interaction - $\mathcal{H}_{ex}$

Below the Néel temperature, the spin-exchange interaction must be included and the spin-exchange Hamiltonian of the Fe^{2+} spin in the host lattice, expressed in Heisenberg exchange form as [27]

$$\mathcal{H}_{ex} = -2 \sum_i J_i \, \underline{S}_i \cdot \underline{S},$$

can be represented by an effective field $\underline{H}_{ex} = -2 \sum_i J_i \, \underline{S}_i$. Thus $\mathcal{H}_{ex} = \underline{H}_{ex} \cdot \underline{S}$, where $\underline{S}$ is the spin of the Fe^{2+} ion which is coupled to the surrounding Mn^{2+} spins $\underline{S}_i$ by an exchange integral J_i. Any interaction between pairs of Fe spins is considered negligible.

For a collinear spin structure one may sum over the nearest and second nearest neighbours to the Fe^{2+} ion to get an effective field of magnitude $J'\langle S_i \rangle$ oriented at an angle θ_{ex} with respect to the trigonal axis. Thus θ_{ex} gives the orientation of the Mn^{2+} spins.

The temperature variation of the statistical average spin $\langle S_i \rangle$ of the Mn^{2+} ions can be calculated from the Brillouin function of spin $\frac{5}{2}$. By keeping $\underline{H}_{ex}$ restricted to the xz plane, imaginary components are eliminated from the Hamiltonian matrix as well as from the eigenfunctions. Then the exchange Hamiltonian is

$$\mathcal{H}_{ex} = \underline{H}_{ex} \cdot \underline{S} = J'\langle S_i \rangle (S_z \cos \theta_{ex} + S_x \sin \theta_{ex})$$

$$= J'\langle S_i \rangle [S_z \cos \theta_{ex} + \frac{1}{2} (S_+ + S_-) \sin \theta_{ex}]$$

Only the dominant magnetic interaction is considered and the minor terms such as dipolar interactions with the surrounding spins are neglected.

2.3.5 The Hamiltonian - $\mathcal{H}'$

The perturbation to the cubic crystal-field states of the high spin ferrous ion is expressed in terms of the perturbing Hamiltonian $\mathcal{H}'$

$$\mathcal{H}' = \lambda \underline{L}.\underline{S} + \Delta[L_z^2 - \tfrac{1}{3}L(L+1)]$$

$$+ J'\langle S_i\rangle[S_z \cos\theta_{ex} + \tfrac{1}{2}(S_+ + S_-)\sin\theta_{ex}]$$

The effect of the trigonal field, spin-orbit and exchange interactions can now be taken into account. If Ψ_i (i = 1, ... 15) represents the 15 states which are products of the orbital states $\psi_{\pm 1}$, ψ_o and the spin states χ_k (k = -2, -1, ..., +2) defined in 2.3.1, then diagonalization of the matrix $\langle\Psi_i|\mathcal{H}'|\Psi_j\rangle$ will give the energies, E_i, and the wave functions

$$\Phi_i = \sum_{j=1}^{15} a_{ij}\,\Psi_j \qquad (2.3)$$

where the coefficients a_{ij} are real because of the restriction of $\underline{H}_{ex}$ to the xz plane.

2.3.6 Temperature Dependent Expectation Value

From Mössbauer spectra we found the magnetic hyperfine field H at the nucleus, and its orientation θ with respect to the principal EFG axes. Now we want to correlate these observations with the temperature dependent expectation values of the spin and orbital operators for the states Φ_i as obtained in equation (2.3). So the expectation value $<0>$ of the operator 0 at temperature T is

$$<0> = \frac{\sum_{i=1}^{15} <\Phi_i|0|\Phi_i> e^{-E_i/kT}}{\sum_{i=1}^{15} e^{-E_i/kT}}$$

where k is the Boltzmann constant and T is the absolute temperature. The calculation of the observed quantities is outlined below.

2.3.7 Hyperfine Interaction

The observed hyperfine field at the ^{57}Fe nucleus may be described by three main contributions.[26]

$$\underline{H} = \underline{H}_L + \underline{H}_D + \underline{H}_S$$

and can be expressed in terms of the orbital and spin angular momentum operators $\underline{L}$ and $\underline{S}$, 3d-electron radial coordinate r and the Bohr magneton μ_B.

(a) $\underline{H}_L$ is the field produced by the orbital moment of the Fe^{2+} ion,

$$\underline{H}_L = 2\mu_B \langle r^{-3} \rangle \langle \underline{L} \rangle$$

Johnson[30], Ingalls[28] and Hazony[31] point out that covalency will reduce $\langle r^{-3} \rangle$ from its free ion value.

(b) $\underline{H}_D$ is the dipolar field produced by the aspherical spin density due to the net electronic spin moment of Fe^{2+},

$$\underline{H}_D = -\frac{1}{2} \mu_B \langle r^{-3} \rangle \langle (3\underline{S}.\underline{r})\underline{r}/r^2 - \underline{S} \rangle$$

The operator form[29] of which is

$$\underline{H}_D = \frac{1}{21} \mu_B \langle r^{-3} \rangle [\frac{3}{2} \underline{L}(\underline{L}.\underline{S}) + \frac{3}{2}(\underline{L}.\underline{S})\underline{L} - L(L+1)\underline{S}]$$

(c) $\underline{H}_S$, the Fermi contact field, arises from the coupling between the nucleus and the imbalance in the s-electron spin density at the nucleus, and can be written as

$$\underline{H}_S = \frac{1}{2} H_c \langle \underline{S} \rangle$$

where H_c is the contact-term effective field and has been calculated to be about -55 tesla for a free ion[32]. In a solid the magnitude of H_c is expected to be reduced by the effects of covalency. This contribution arises mainly from the polarization of the inner s-electrons by exchange interaction with the 3d electrons.

CHAPTER 3

EXPERIMENTAL

3.1 THE MÖSSBAUER SPECTROMETER

A constant acceleration spectrometer with a 28 mCi ^{57}Co/Rh source was used. ^{57}Co decays to the 136 keV excited state in ^{57}Fe and this in turn decays 91% of the time to the first excited state at 14.4 keV. The Mössbauer γ-ray is emitted when this state decays to the ground state. The decay scheme of ^{57}Co is shown in Fig. 3.1.

In the spectrometer the source is mounted on a velocity transducer driven from a sawtooth wave. In the cases of constant acceleration waveforms, the velocity is linearly related to the channel number.

The detector used is an Xe-CO_2 Reuter Stokes model RS-P3-1605-263 proportional counter, whose resolution is 12.8% at 14.4 keV.

The spectrum can be obtained by repetitive scanning of the velocity. The output from the detector is fed through an ORTEC 109PC preamplifier, which gives a 40 μs wide output pulse to the ORTEC 440A linear amplifier.

An ORTEC 406A single channel analyser separates the Mössbauer γ-ray pulses from other γ and x-ray pulses and stores them in a PDP-8 mini-computer. Each of the computer's available 400 channels stores a γ-ray count corresponding to one single velocity increment. A block diagram of the equipment is shown in Fig. 3.2.

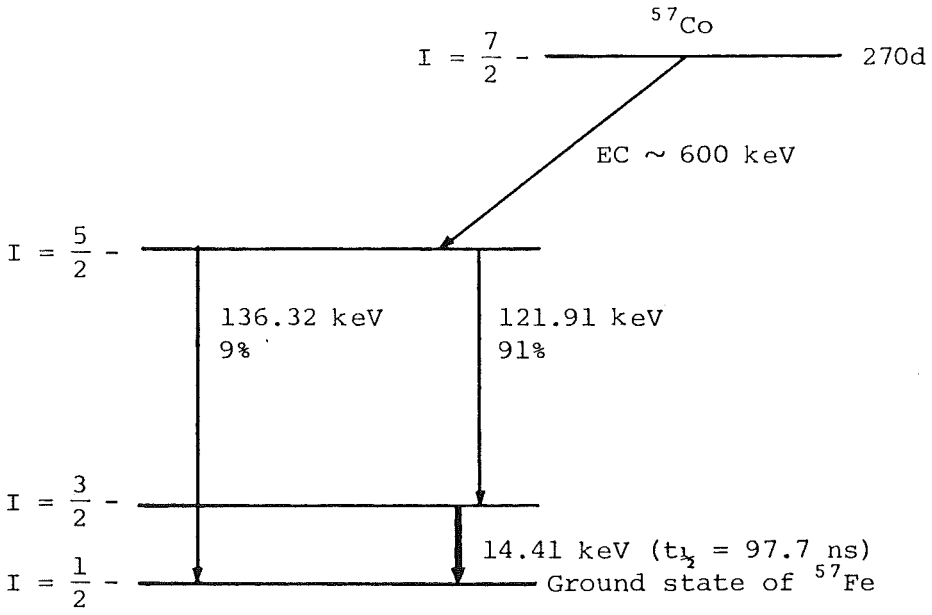

Figure 3.1 Decay scheme of ^{57}Co.

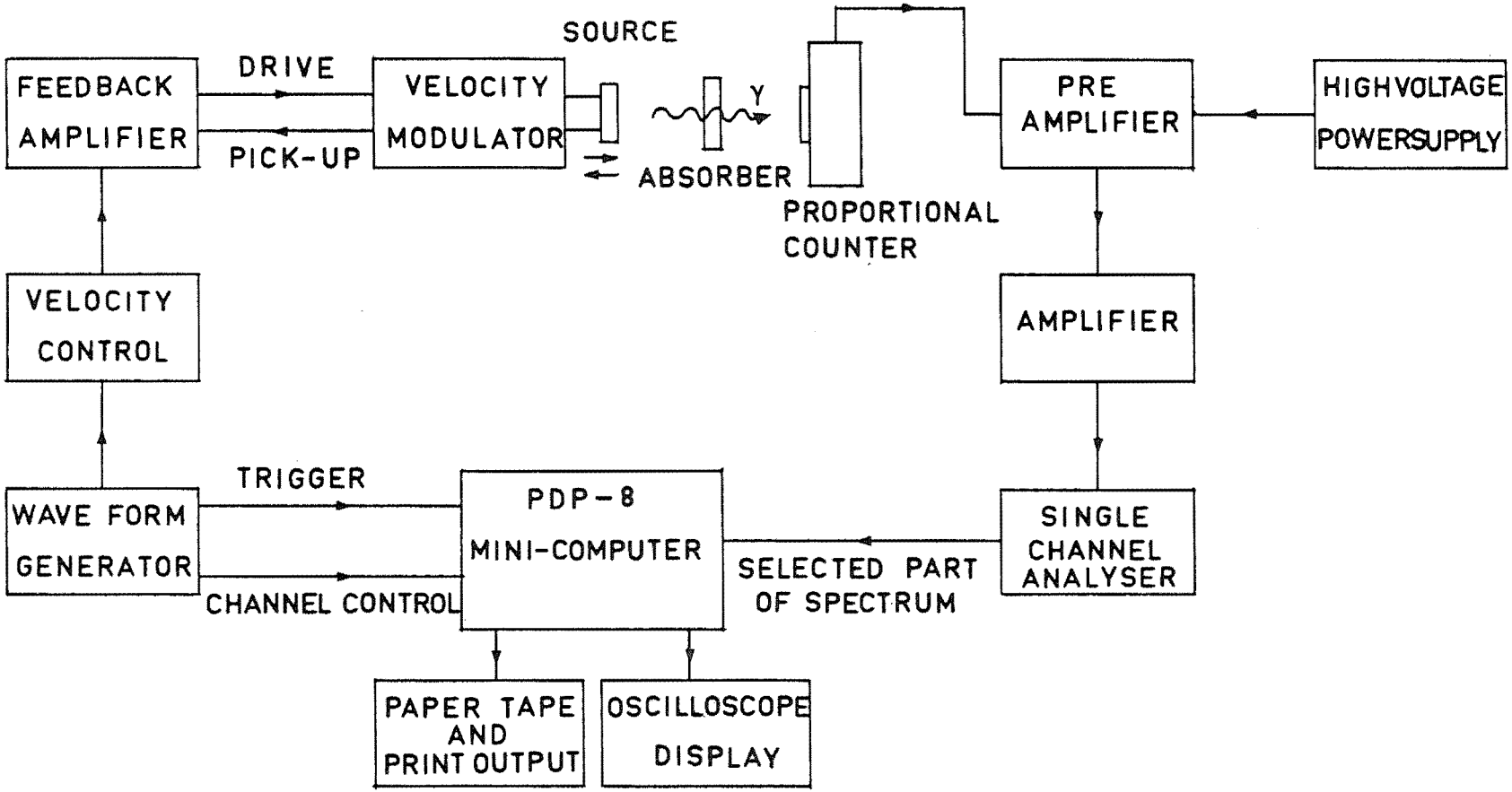

Figure 3.2 Block diagram of the Mössbauer spectrometer.

The spectrum is displayed on an oscilloscope as the counts accumulate during the run. At the end of the run, the total count in each of the 400 channels is punched onto paper tape and typed onto a sheet of paper.

3.2 DATA ANALYSIS

The paper-tape data is processed directly in the Burroughs B6718 computer. The computer analysis requires estimates of the relevant parameters as input. The line shape is presumed to be Lorentzian. Above the Néel temperature, the quadrupole interactions are analysed as line-pairs requiring initial estimates of baseline, isomer shifts, quadrupole splittings, line-widths and the total absorption intensity. Below the transition temperature, combined quadrupole and magnetic hyperfine interactions are analysed as "bunches" of lines, which require in addition, estimates of the internal magnetic field H, asymmetry parameter η and the angle θ this field makes with the EFG principal z axis. Initial estimates of these hyperfine parameters were taken from theoretical spectra. These parameters are refined through the iterative process by the least squares fitting program (based on Bent et al.'s[33] program) until the statistical parameter χ^2 is a minimum. χ^2 is the weighted sum over all data points of the squared difference between the postulated Lorentzian functions and the experimental data[33]. A good fit will give the minimum value of χ^2 within the 1% and 99% points of the

χ^2 distribution. These limits can be calculated[19] as $n+2.2 \pm 3.3\sqrt{n}$, where n is the number of degrees of freedom, i.e. the number of total channels minus the number of adjustable parameters used in the fitting spectrum.

3.3 CRYOGENIC APPARATUS

The low-temperature spectra were taken with the sample inside a RICOR MCH-5B cryostat. Liquid air, liquid nitrogen or liquid helium was drawn through the vacuum cryostat by suction of the appropriate gas through the outlet to a mechanical vacuum pump. The gas flow was regulated by an automatic temperature controller through main and bleed valves, with series needle and solenoid valves parallel to a needle valve on the mainline and a single needle valve on the bleed line. The temperature of the sample was measured to an accuracy of $\pm$ 0.5K (except where stated) by use of a Gold + 0.07 at.% iron vs chromel thermocouple, keeping the reference junction at ice-temperature. The thermocouple was calibrated by taking emf readings with the measuring junction at room temperature, keeping the reference junction successively in ice and in LN_2. The measured thermoelectric emf's, together with the LHe temperature emf of 1.22 mV (reference junction at LN_2 temperature, supplied by RICOR cryostat manufacturer Ltd.) was compared with a standard table of emf's for this alloy combination.[34] The differences were linearly interpolated, and the expected thermoelectric emf for all temperatures between

4K and 280K were calculated. In the cryostat the thermocouple low-temperature junction is bolted to the sample chamber as shown in Fig. 3.3. The sample chamber is under vacuum and cooled by having the liquid coolant passed around it. The sample holder is made of boron nitride and is pressed against the base of the sample chamber by spring tension. Apiezon-N high vacuum grease was used for better thermal contact between sample holder and the sample ring. The low temperature flow diagram is shown in Fig. 3.4.

3.4 SINGLE CHANNEL ANALYSER GATE

As most Mössbauer sources are not monoenergetic, and emit radiation of higher or lower energy than the Mössbauer γ-ray, the detection system must be set to pass only the Mössbauer radiation. The appropriate γ-ray energy can be selected by setting the SCA gates at each side of the 14.4 keV peak as shown in Fig. 3.5. In this spectrum the amplifiers pulse height voltage is directly proportional to the energy.

3.5 CALIBRATION OF SPECTROMETER

The spectrometer is calibrated as soon as possible after each set of runs so that the velocity scale scanned is unaltered. The absorber is replaced by a standard iron foil[35]. The centroid of the inner-most two lines is taken as the zero isomer shift (or energy point). All

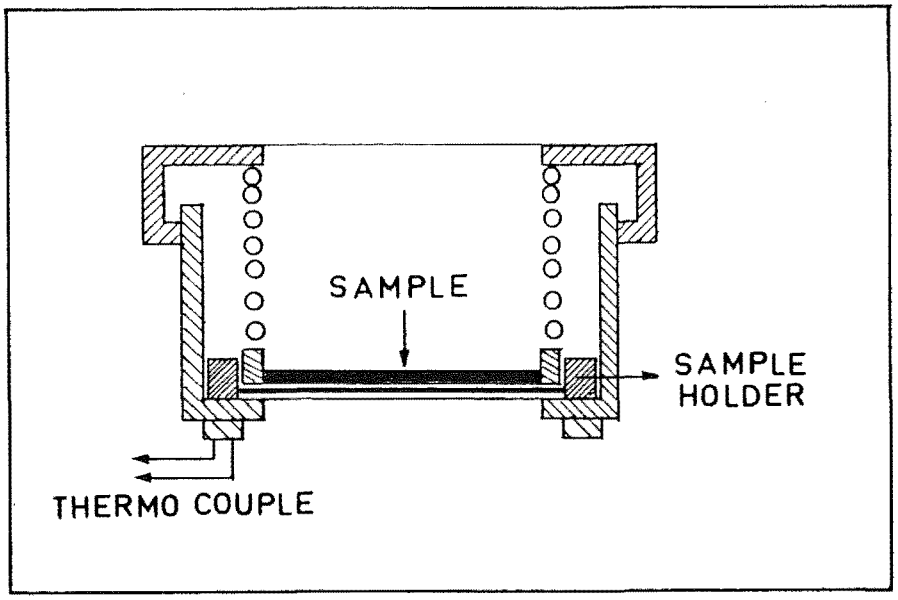

Figure 3.3 Cryostat sample chamber.

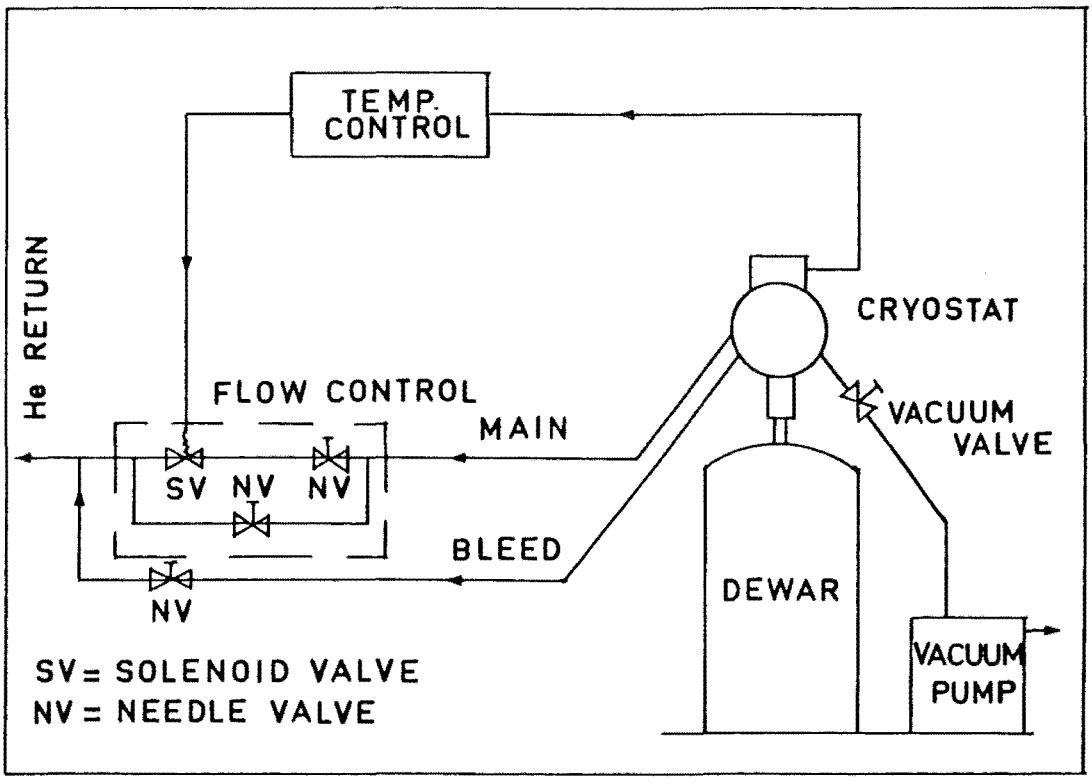

Figure 3.4 Low temperature flow diagram.

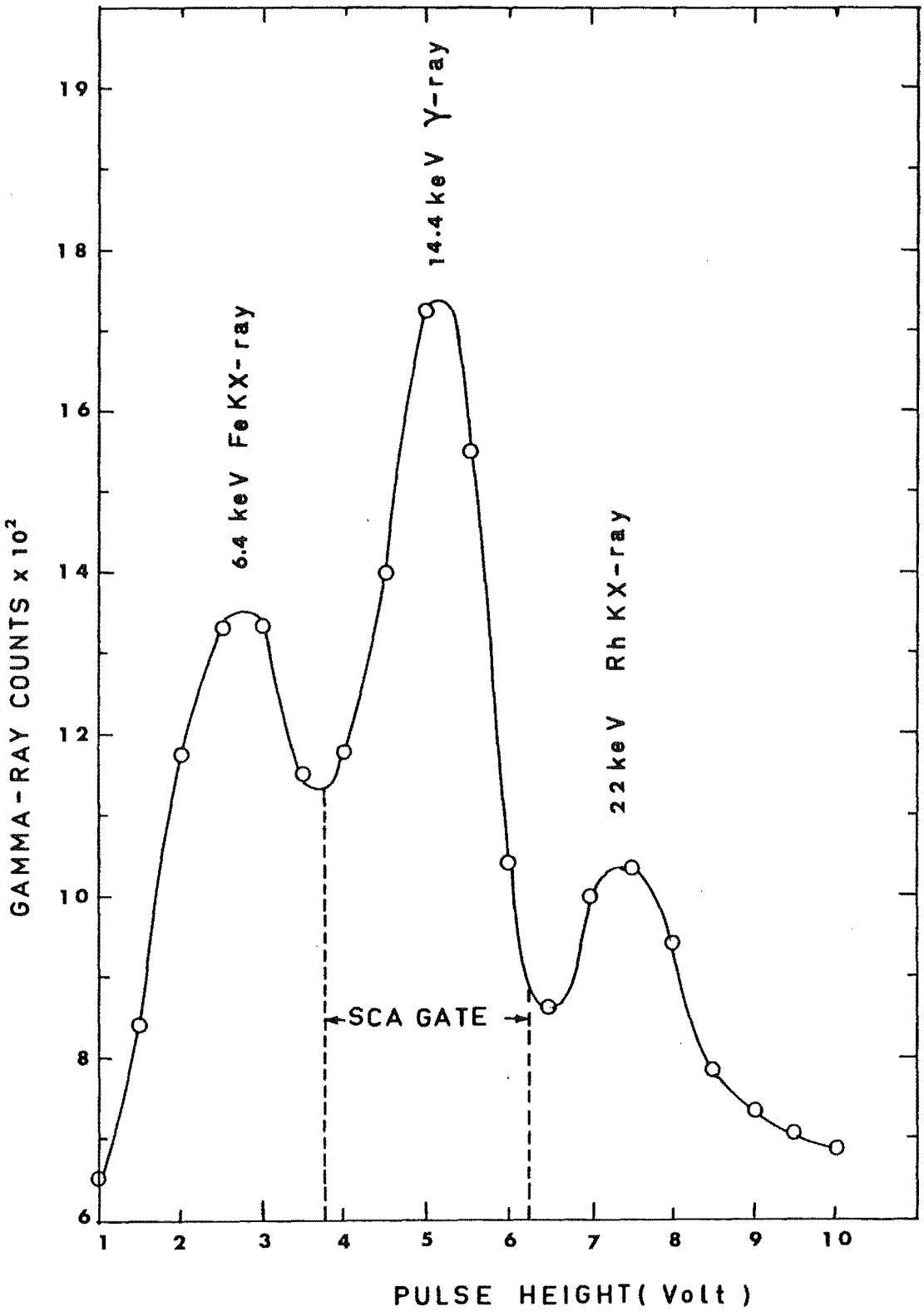

Figure 3.5 Pulse height spectrum of ^{57}Co source. γ-rays have passed through the $MnSe_2$ 2% ^{57}Fe absorber.

the spectra are calibrated in this way with respect to this standard natural iron.

3.6 SAMPLE PREPARATION AND CHARACTERISATION

Considerable care was taken, and time spent, in preparing pure samples. All the samples used in this work were prepared by the author. The starting materials were of high purity and are listed in Table 3.1 with their appropriate origin.

In section 2.2.5 we described the general features of Mössbauer spectra. Bargeron et al.[36] investigated the effect of pressure on the Mössbauer spectra of ^{57}Fe-doped MnS_2, $MnSe_2$ and $MnTe_2$ and reported 2 pairs of lines which they interpreted as being due to the high and low-spin states of Fe^{2+}.

In our observations, the major component (pair I) agreed well with Bargeron et al.'s parameters for the high-spin pair; the less intense component (pair II) agreed well with their parameters for the pair they interpreted as low-spin (Table 4.1). If these pairs are due to high and low spin states, then the variation of temperature should change their relative absorption as happens for example with $Fe(phen)_2(NCS)_2$ and $Fe(phen)_2(NCSe)_2$ (Ref. 18, page 195). We did not observe such an effect. Furthermore, we found that with careful preparation, pair II could be completely or almost completely eliminated in these compounds. In all $MnSe_2$ compositions we observed

Table 3.1 Purity of the starting materials and their origin.

Element	Purity %	Origin
Sulphur Powder	$\geqslant$ 99.99	Koch-Light Labs Ltd.
Selenium Pellets	99.9999	"
Tellurium Lumps	99.999	"
Manganese Flake	$\geqslant$ 99.995	"
Iron Sponge	99.998	"
^{57}Fe	90.42	A.E.R.E. Harwell
Manganese Sulphate	Analar grade	Hopkins and Williams Ltd.
Potassium Polysulphide	"	May and Baker Ltd.

only one pair of lines (Table 4.2). We also noticed that Bargeron et al's. pair II parameters are very close in value to those of the corresponding Fe compound, i.e. to FeS_2, $FeSe_2$ and $FeTe_2$. We therefore conclude that pair II is due to the presence of the Fe compound in the samples, and that Fe doped into the manganese dichalcogenides is normally 100% high-spin at 1 atmosphere. This does not conflict with the general conclusions of Bargeron et al.'s paper, namely the presence of a high to low-spin transition in these compounds when they are pressurized.

The lines in a ^{57}Fe Mössbauer spectrum have a natural line width Γ of 0.19 mm s^{-1}. Experimentally obtained spectra from moderately thick absorbers have slightly wider lines than this, namely 0.22 - 0.23 mm s^{-1}, due to the thickness effect[21], cosine broadening[18], and the inhomogeneus distribution of ^{57}Fe in the sample. So comparing to this, at room temperature, our samples showed quite good linewidths (Tables 4.1 and 4.2).

3.6.1 MnS_2 Sample

Heating the elements together produces only α-MnS even when excess sulphur is present[37]; the MnS_2 was therefore prepared by a hydrothermal method[38,39]. A solution of $MnSO_4.4H_2O$, a solution of potassium polysulphide and powdered sulphur were heated together in a sealed glass tube of 2.85 cm diameter, enclosed in a steel autoclave partly filled with water (Fig. 3.6). The X-ray diffraction

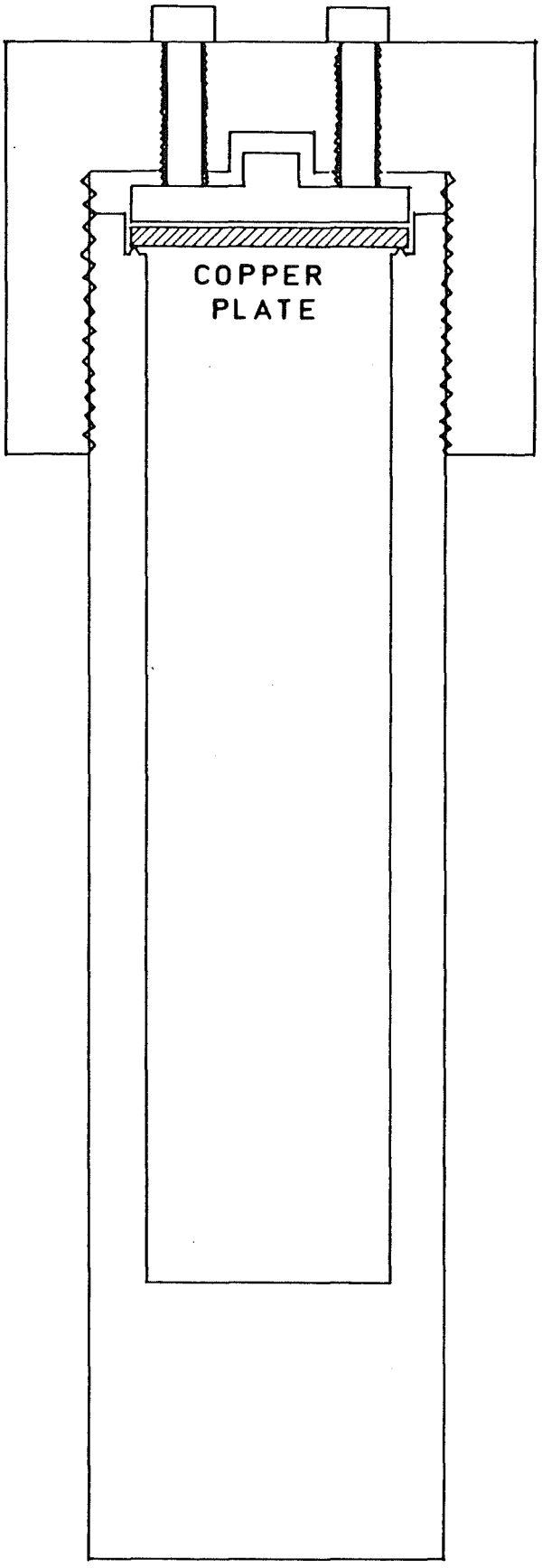

Figure 3.6 Full scale sectional view of steel autoclave.

spectrum of the resulting MnS_2 showed the presence of ~ 38% α-MnS impurity in this initial, undoped sample. In our next attempt we reduced the heating time to 20 hours at 240°C and prepared pure MnS_2. Keeping the preparation conditions unchanged, we next prepared a sample doped with ½ atomic % ^{57}Fe. The ^{57}Fe was dissolved in dilute HCl; excess water and HCl were pumped off under vacuum and the $MnSO_4.4H_2O$ and potassium polysulphide solutions added, together with the powdered sulphur. The air was pumped out and the tube fused shut. After heating, the solution looked as in Fig. 3.7. This sample showed ~ 3% α-MnS in the X-ray diffraction spectrum. We tried twice more, varying temperature and time, and observed higher α-MnS concentrations each time. As insufficient polysulphide might produce α-MnS, we always added excess potassium polysulphide in these preparations. We finally concluded that temperature and time played the major role in the preparation and the best values of these are 240°C and 20 hours respectively. Deviations from these values always increased the α-MnS concentration. The estimated amount of α-MnS and the heating program (temperature and time) are given in Table 3.2. The amounts of α-MnS were estimated from the relative intensities of the Bragg reflections of the X-ray spectra.

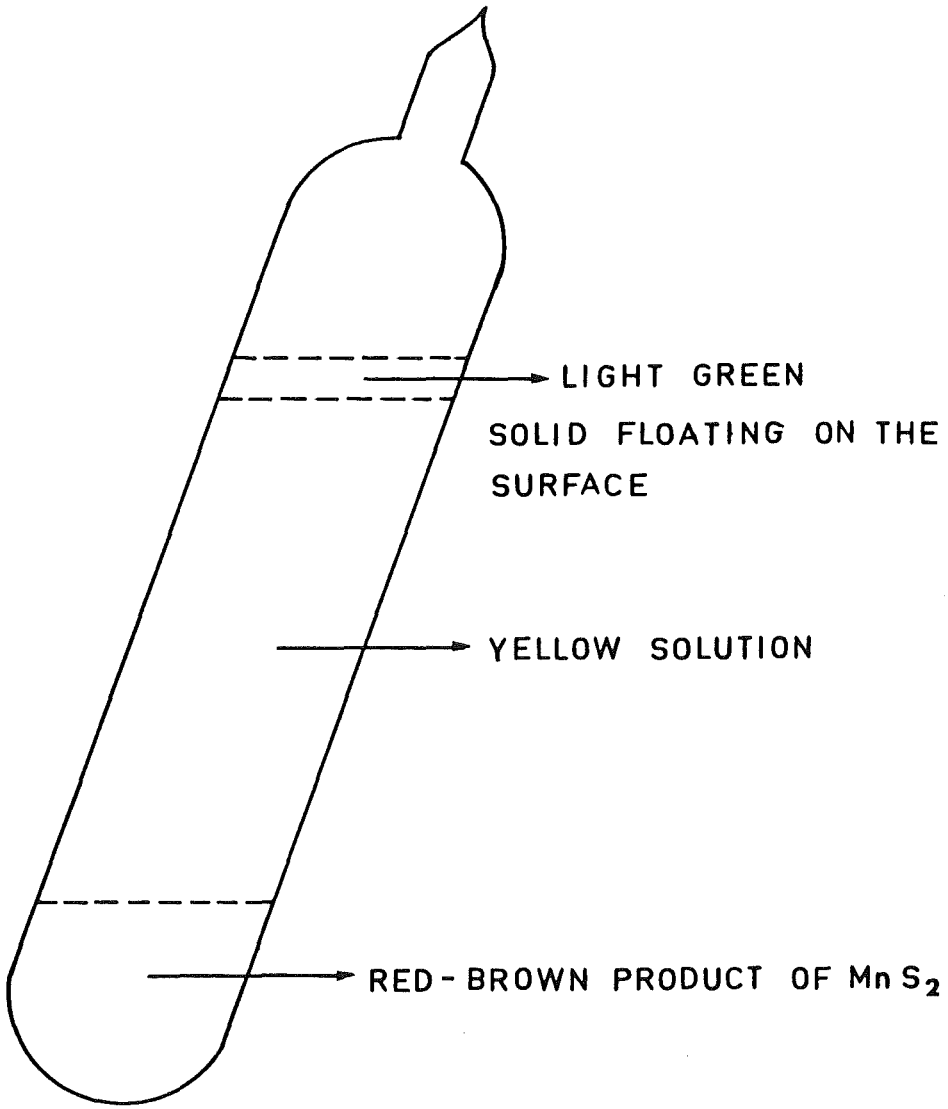

Figure 3.7 Appearance of the sealed glass tube after a successful MnS_2 preparation.

Table 3.2 MnS_2 prepared by hydrothermal method.

Samples	Temp. (°C) ±2	Time (Hour)	Presence of α-MnS (%)
MnS_2	240	24	38 ± 4
MnS_2	240	20	< 1
MnS_2 ½% ^{57}Fe	240	20	3 ± 1
MnS_2 ½% ^{57}Fe	237	18	5 ± 2
MnS_2 ½ ^{57}Fe	230	18	39 ± 7

3.6.2 $MnSe_2$ Sample

Polycrystalline samples were prepared by mixing and heating stoichiometric proportions of the elements. In our first attempts, manganese and selenium were ground and mixed and the ^{57}Fe was added. The mixture was pressed into a pellet of diameter 6 mm and heated at 500°C for 5 days in an evacuated 1 cm diameter vitreous silica tube. The pellet was ground, sieved through a 60 μm diameter mesh, repressed and reheated twice more in the same way and four Mössbauer samples were prepared; all the samples showed extra Mössbauer absorption lines due to Fe_2O_3. We suspect these are due to presence of air trapped inside the pressed pellets. The Fe_2O_3 could not be removed by subsequent heating. In our next attempts the elements were ground, mixed, placed into a previously degassed

vitreous silica tube and the mixture degassed under vacuum at a temperature of ~ 200°C. All the samples were sealed off under a vacuum of 5 - 9 x 10^{-5} Torr and heated at 500°C for 5 days, after which the tubes were quenched into ice-water, opened, and the contents ground and sieved through a 60 μm diameter mesh. They were then degassed and resealed as described above and annealed two more times at 500°C for 5 days. The X-ray diffraction and room-temperature Mössbauer spectra confirmed that the samples contained only $MnSe_2$. A list of pure samples is given in Table 3.3.

Table 3.3 List of ^{57}Fe-doped $MnSe_2$ samples prepared, and their compositions.

Samples (Fe content given in atomic %)
$MnSe_2$ 1% ^{57}Fe
$MnSe_2$ 2% ^{57}Fe
$MnSe_2$ 5% Fe (2% ^{57}Fe + 3% Fe sponge)
$MnSe_2$ 7.5% Fe (2% ^{57}Fe + 5.5% Fe sponge)
$MnSe_2$ 10% Fe (3% ^{57}Fe + 7% Fe sponge)
$MnSe_2$ 20% Fe (3% ^{57}Fe + 17% Fe sponge)
$MnSe_2$ 30% Fe (2% ^{57}Fe + 28% Fe sponge)
$MnSe_2$ 50% Fe (1% ^{57}Fe + 49% Fe sponge)

3.6.3 $MnTe_2$ Sample

Polycrystalline samples of doped $MnTe_2$ were prepared directly from a stoichiometric mixture of Mn, Te and ^{57}Fe. The elements were ground, mixed and sintered at 500°C for 3 days in an evacuated vitreous silica tube. They were ground, mixed and sintered two more times at 500°C for 5 days and 8 weeks respectively. The room temperature Mössbauer spectra showed that the ½ at. % ^{57}Fe-doped sample was pure and 2 at. % sample contained only a very small amount of $FeTe_2$. However, the 1 and 5 at. % samples had more $FeTe_2$. To get rid of the $FeTe_2$ we decided to reheat these samples; however after reheating for a total time of 6 more weeks, we observed that the $FeTe_2$ content was increased. Two further samples doped with 2 at. % ^{57}Fe were prepared using the same technique as with $MnSe_2$, but in each case a sizeable amount of $FeTe_2$ was present. The Mössbauer studies reported in this thesis were accordingly carried out using the original 2 at. % ^{57}Fe sample.

3.7 X-RAY DIFFRACTION

The samples were ground and sieved, spread on a cleaned glass plate and moistened with acetone. X-ray diffraction spectra were taken at room temperature on a Philips PW1050 X-ray diffractometer. A proportional counter was used as detector with a PN4280 analyser. The expected X-ray line-positions of the pyrite-structure crystals with CuKα-radiations were calculated (computer program is listed in Appendix B) and compared with the absorbed positions.

The lattice parameter was calculated from the 2θ value of a high angle line for each sample. The results are listed in Table 3.4, together with those of other workers.

3.8 PREPARATION OF ABSORBERS

The finely ground powder sample was sieved through a 60 μm diameter mesh. A suitable amount of it was taken to prepare a 5-10 mg of natural Fe per sq. cm absorber (i.e. 0.1-0.2 mg of ^{57}Fe as ^{57}Fe is ~ 2% abundant in natural Fe), which was mixed with powdered boric acid (used as a binder) and pressed flat inside a steel ring of area ~ 2.19 cm^2, by applying a hydraulic pressure of ~ 230 MPa.

Table 3.4 Crystallographic data for Mn-pyrites.

Compound	Lattice parameter a(Å)		u
	Others	Our	(4)
MnS_2	6.097(5) [4] 6.09(1) [39] 6.1016 [37]	6.099(5)	0.4012
$MnSe_2$	6.417(5) [4] 6.429(1) [10]	6.427(5)	0.393
$MnTe_2$	6.943(2) [4] 6.950(4) [16] 6.951(2) [40] 6.954(1) [7] 6.958 [12]	6.939(5)	0.386

CHAPTER 4

RESULTS AND ANALYSIS

4.1 THE MÖSSBAUER SPECTRA OF MnS_2, $MnSe_2$ AND $MnTe_2$

4.1.1 Mössbauer Spectra at Room Temperature

The fitted spectra of MnS_2, $MnTe_2$ and $MnSe_2$ at room temperature are shown in Figs. 4.1 and 4.2. In these, and all other spectra shown in this thesis, the square dots are experimental results, and the solid curves are spectra calculated from models described in chapter 2. In the tables error estimates are given in brackets on the last quoted digits, for example, 14.6(1.1) means 14.6 ± 1.1 and 0.832(5) means 0.832 ± 0.005.

The straight line spectra (stick diagrams) indicate line positions and relative intensities for various spectra. In MnS_2 the deepest lines are the absorptions corresponding to the high-spin state of Fe^{2+} in MnS_2; the less intense pair are due to FeS_2. A tiny single line corresponds to the presence of α-MnS in the sample[41]. In $MnTe_2$ the major pair of lines are due to the high-spin state of Fe^{2+} in $MnTe_2$ and other pair corresponds to the compound $FeTe_2$ (this pair was not observed in 0.5% ^{57}Fe sample).

In the case of $MnSe_2$, several samples with different Fe-concentrations were prepared and room temperature spectra were taken, but only representative spectra of 2%, 7.5%, 30% and 50% Fe samples are shown (Fig. 4.2). The X-ray diffraction spectra of the low ^{57}Fe concentration samples

between 2 at. % and 30 at. % showed a single phase pyrite structure. At room temperature, the general nature of the Mössbauer spectra of the 2%, 7.5% and 30% samples are the same and are fitted with a single pair of lines; the stick diagram for the 2% sample is shown. However, the Mössbauer spectrum of the 50% sample is fitted with two pairs of lines and is consistent with the X-ray diffraction result, which showed two phases in this sample. Thus, in the Mössbauer spectrum the extra pair of lines comes from the marcasite phase. In Fig. 4.2 the less intense pair of lines (large quadrupole splitting) corresponds to iron in $MnSe_2$ (pyrite structure) and the other pair arises from $FeSe_2$ (marcasite structure). The fitted parameters are listed in Tables 4.1 and 4.2 together with the results of other workers.

4.1.2 Low Temperature Mössbauer Spectra

We selected samples MnS_2 0.5% ^{57}Fe, $MnSe_2$ 2% ^{57}Fe, $MnSe_2$ 20% Fe and $MnTe_2$ 2% ^{57}Fe for detailed Mössbauer studies. The Néel temperatures (T_N) of these samples were determined as 49 $\pm$ 0.5, 51 $\pm$ 0.5, 85 $\pm$ 1 and 91 $\pm$ 0.5K respectively. In addition, Mössbauer spectra of 1%, 5%, 7.5%, 10% and 30% Fe-concentration samples of $MnSe_2$ were recorded at 20K and fitted. Also the Fe-concentration dependence of T_N for ^{57}Fe-doped $MnSe_2$ was determined through Mössbauer spectroscopy. Below T_N, the samples showed some line-broadening, possibly due to inhomogeneity of the ^{57}Fe in the sample.

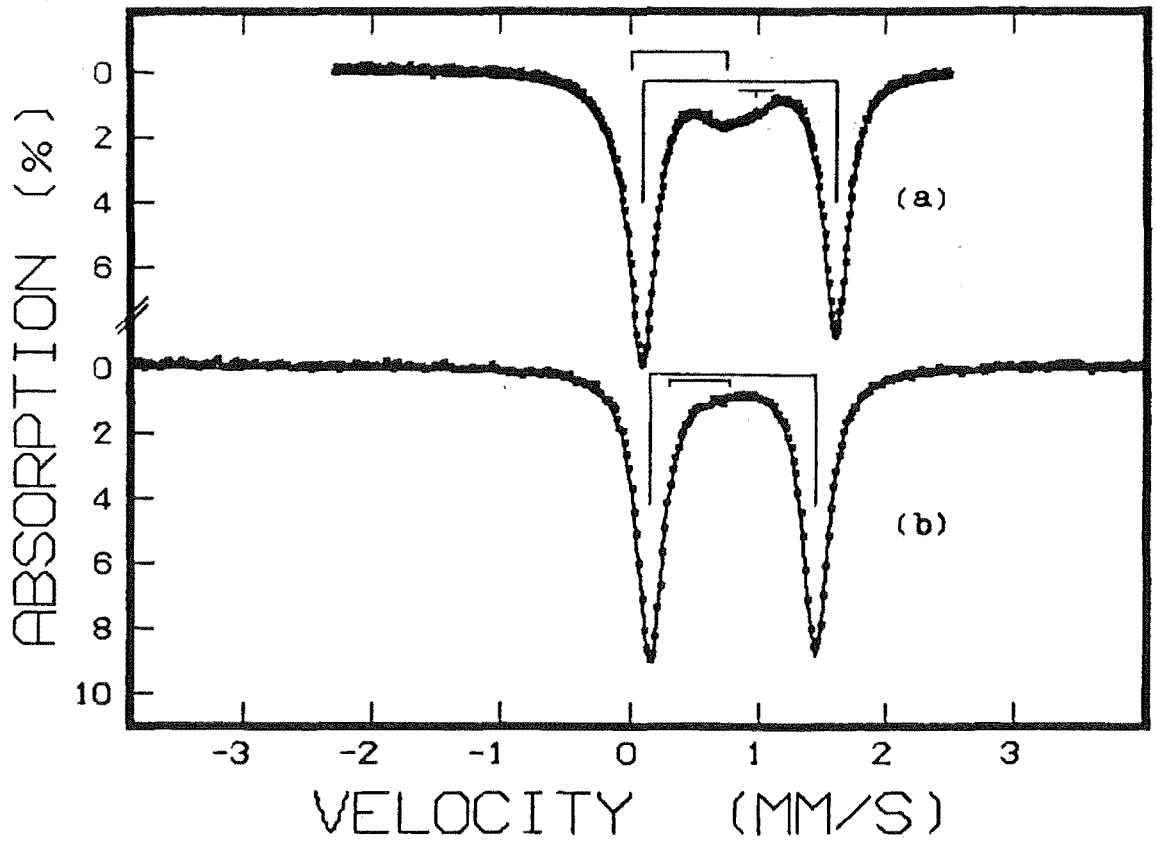

Figure 4.1 Room temperature Mössbauer spectra of (a) MnS_2 0.5% ^{57}Fe and (b) $MnTe_2$ 2% ^{57}Fe.

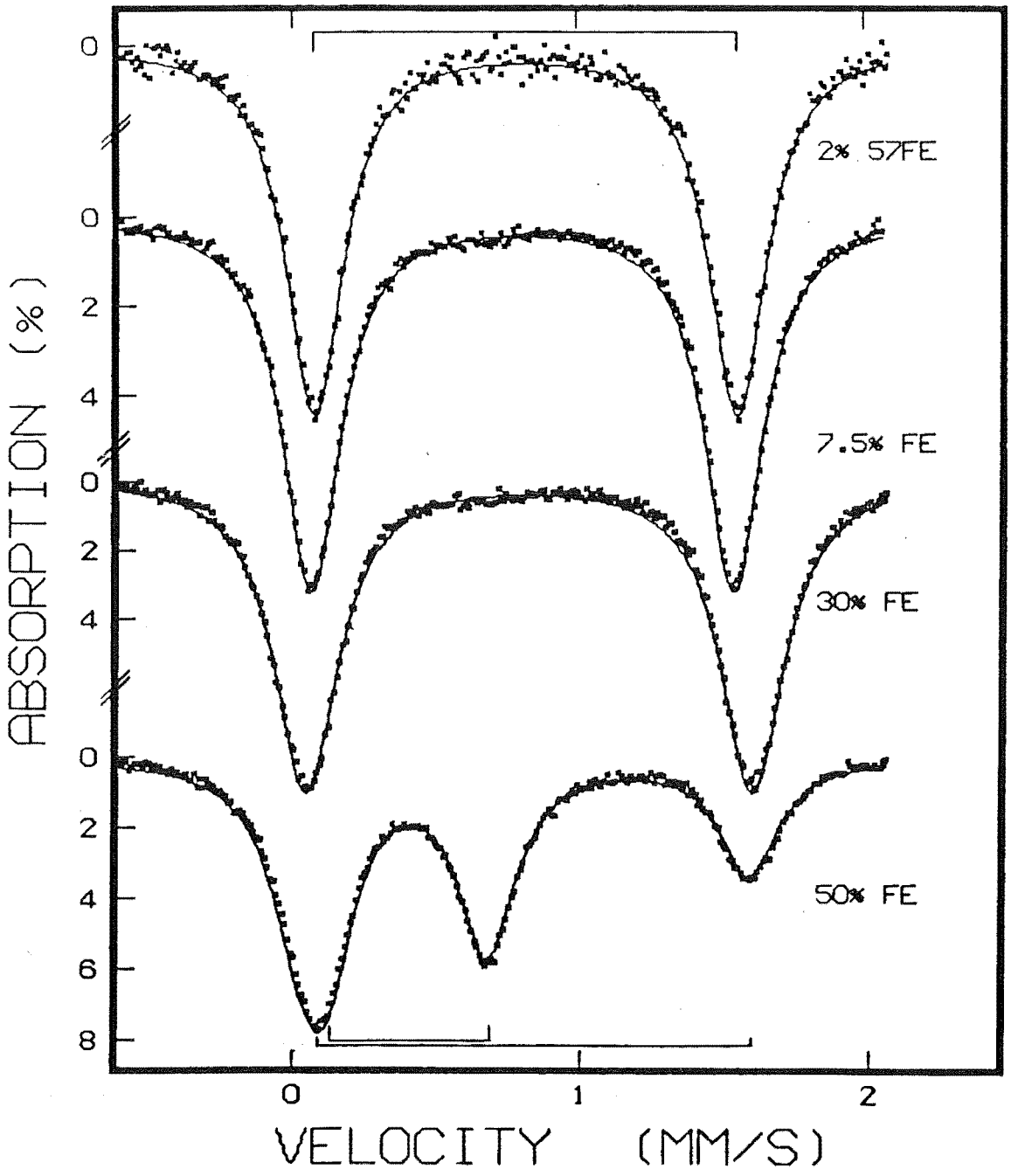

Figure 4.2 Room temperature Mössbauer spectra of $MnSe_2$.

Table 4.1 Room-temperature Mössbauer parameters for ^{57}Fe-doped MnS_2 and $MnTe_2$ and for FeS_2 and $FeTe_2$.

Compound	Fe-conc. (atomic %)	Temperature (K)	Our results				Bargeron et al's results		Others	
			QS (mm s^{-1})	IS (mm s^{-1})	Γ (mm s^{-1})	Fractional absorption	QS (mm s^{-1})	IS (mm s^{-1})	QS (mm s^{-1})	IS (mm s^{-1})
MnS_2 (p)	0.5% ^{57}Fe	296(1)	1.50(1) 0.77(1)	0.832(5) 0.324(6) 0.95(2)	0.219(2) 0.42(2) 0.267(4)	0.157(1) 0.024(1) 0.005(1)				
αMnS	0.5% ^{57}Fe	293(1)								0.95(2) [a]
MnS_2 (p)	2% ^{57}Fe	RT					1.50 0.60	0.84 0.35		
FeS_2 (p)		RT							0.62(1) [b] 0.62(2) [c] 0.614(6) [d]	0.25(1) 0.325(5) 0.314(2)
$MnTe_2$ (p)	0.5% ^{57}Fe	294(2)	1.30(1)	0.789(7)	0.232(5)	0.062(1)				
	2% ^{57}Fe	293(1)	1.29(1) 0.48(7)	0.784(8) 0.54(4)	0.234(2) 0.7(2)	0.172(1) 0.006(1)	1.35 0.48	0.77 0.51		
$FeTe_2$ (m)		300							0.502(11) [d]	0.471(5)

(a) Ref (41) (c) Ref (43) p and m stand for pyrite and marcasite structures respectively.
(b) Ref (42) (d) Ref (44)

Table 4.2 Room-temperature Mössbauer parameters for ^{57}Fe-doped $MnSe_2$ and for $FeSe_2$.

Compound	Fe-conc. (atomic %)	Temperature (K)	Our results				Bargeron et al's results		Others	
			QS (mm s^{-1})	IS (mm s^{-1})	Γ (mm s^{-1})	Fractional absorption	QS (mm s^{-1})	IS (mm s^{-1})	QS (mm s^{-1})	IS (mm s^{-1})
$MnSe_2$(p)	1% ^{57}Fe	291(2)	1.47(1)	0.821(7)	0.235(5)	0.101(2)				
	2% ^{57}Fe	295(1)	1.47(1)	0.815(6)	0.241(5)	0.151(2)	1.51 0.54	0.81 0.48		
	5% Fe	295(1)	1.49(1)	0.816(5)	0.242(2)	0.175(2)				
	7.5% Fe	298(1)	1.47(1)	0.801(5)	0.241(2)	0.165(1)				
	10% Fe	293(2)	1.51(1)	0.816(7)	0.268(5)	0.257(2)				
	20% Fe	291(2)	1.51(1)	0.805(7)	0.280(5)	0.245(2)				
	30% Fe	293(1)	1.54(1)	0.814(5)	0.266(5)	0.178(2)				
	50% Fe	295(1)	1.55(1) 0.56(1)	0.795(7) 0.396(7)	0.247(8) 0.240(5)	0.064(2) 0.105(2)				
$FeSe_2$(m)		300							0.584	0.395 [a]

(a) Ref (44) p and m stand for pyrite and marcarsite structures respectively.

The temperature dependences of the various parameters are discussed in the following sections. In graphing these parameters points with error bars are estimated from the least squares fitting output and from the uncertainties in the standard line positions.

4.1.2.1 MnS_2 0.5% ^{57}Fe Sample

Mössbauer spectra were taken at various temperatures between 5K and 296K and representative spectra at $T \leqslant T_N$ are shown in Figs. 4.3 and 4.4. The spectra below T_N were fitted with a bunch and a pair of lines; the pair represents the compound FeS_2. In the bunch fitted parameters (ϕ assumed to be zero), the η values were all < 0. A value of η in the range $-1 < \eta < 0$ with $\phi = 0$ corresponds to a relabelling of the x,y axes such that $y \rightarrow x$ and $x \rightarrow -y$. Accordingly we list the η values as > 0 and assume that $\phi = 90°$. The stick diagram for the bunch and the pair are drawn for the 5K spectrum in Fig. 4.3. Although the spectra above T_N showed the presence of α-MnS and were fitted with an additional single-line, below the transition temperature this site could not be detected in the fit, perhaps because of its very small absorption effect.

The spectrum at 48K, just below T_N, was fitted with an extra pair of lines that had similar parameters to those of the spectra above T_N. The composite spectrum could be caused by:

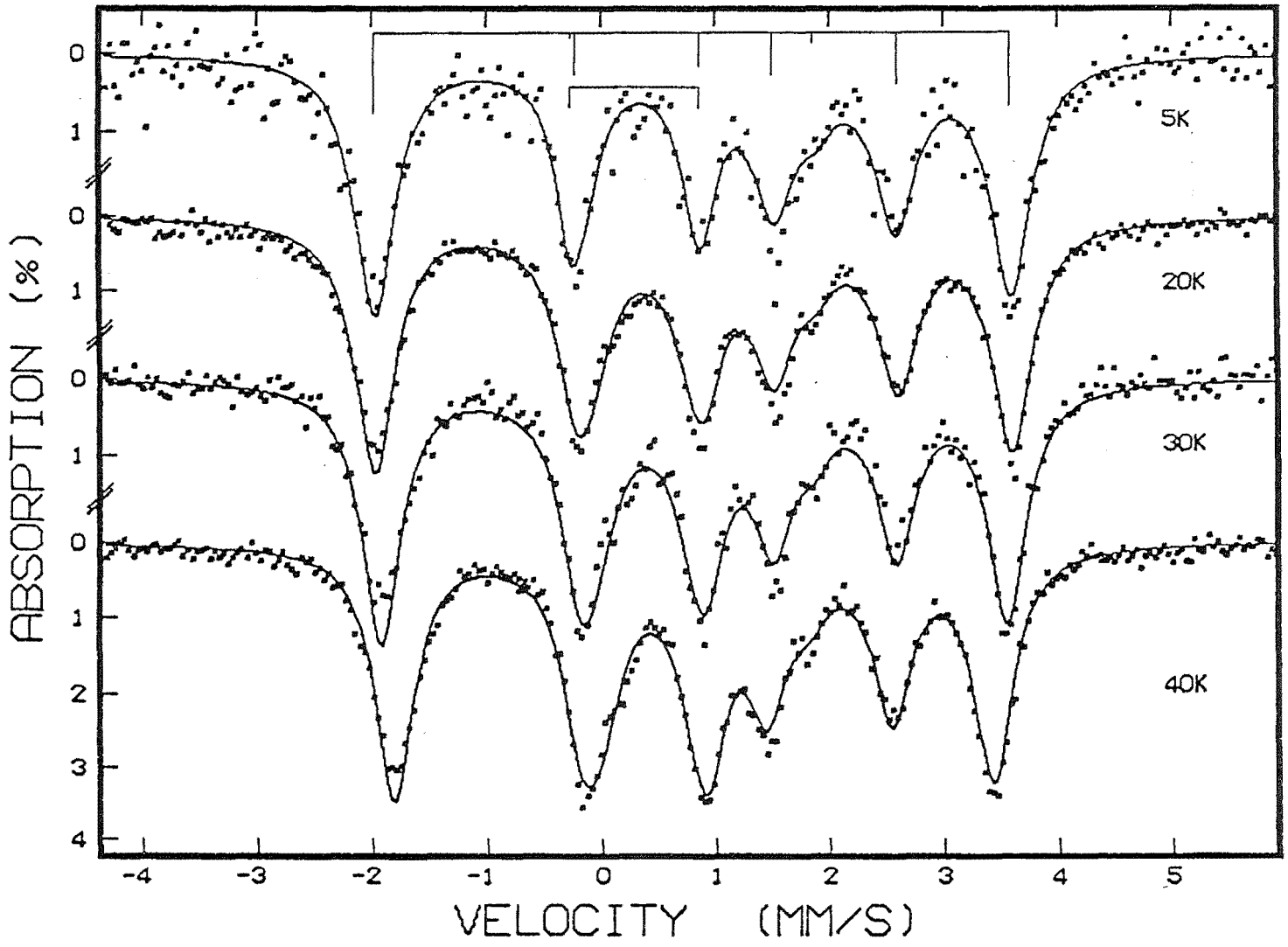

Figure 4.3 Mössbauer spectra of MnS_2 0.5% ^{57}Fe below T_N.

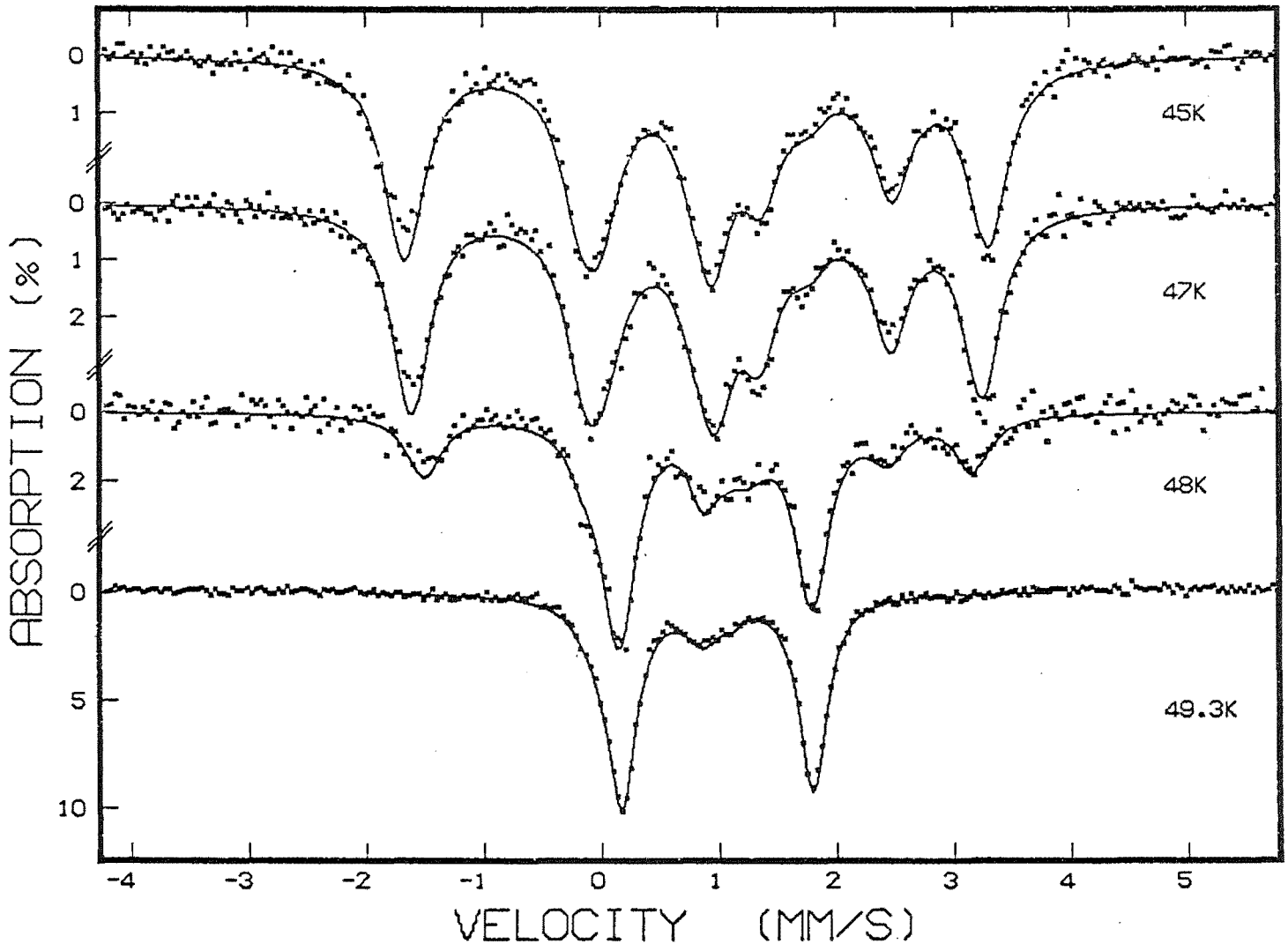

Figure 4.4 Mössbauer spectra of MnS_2 0.5% ^{57}Fe at $T \leqslant T_N$.

(i) Temperature variations during the run switching the sample above and below its T_N, or

(ii) Lack of homogeneity in the ^{57}Fe distribution throughout the sample and consequent T_N variation in different parts of the sample. This effect might be caused by a nearest neighbour (J_1) and second nearest neighbour (J_2) exchange interaction variation between the Fe-Mn ion pairs, and Mn-Mn ion pairs, in the sample. We observed, that doping Fe in the sample increases T_N, so if Fe is inhomogeneously substituted into the MnS_2 the sample could have a range of values for T_N. The best fitted parameters are given in Tables 4.3 and 4.4.

The combined effect of magnetic dipole and electric quadrupole interaction cannot determine a unique solution of η,θ,ϕ and QS, so full range of these parameters was calculated to determine the ambiguity. van Dongen Torman et al.[45] have given a detailed account of this calculation.

For this sample we calculated the ambiguous solutions for the 20K and the 47K spectra. The 20K spectrum gives ranges of, η = 0.2 - 1.0, θ = 67.5° - 72.4°, ϕ = 49.2° - 90° and QS = 1.58 - 1.81 mm s^{-1} and 47K spectrum gives η = 0.15 - 1.0, θ = 70° - 78°, ϕ = 44° - 66° and QS = 1.46 - 1.68 mm s^{-1}. Different sets of values could be determined for QS < 0.

In $MnTe_2$, similar calculations were made; the sign of QS was uniquely determined as positive, with QS ranging from 1.36 to 1.37 mm s^{-1}. We therefore assume that the sign of QS in MnS_2 and $MnSe_2$ is also positive.

IS and QS increase with decreasing temperatures and are plotted in Figs. 4.5 and 4.6 respectively. The temperature dependence of η is plotted in Fig. 4.7. The isomer shift data were computer fitted on the Debye model[46]

$$IS(T) = IS(0) - (3000\,RT/2Mc)D(\theta_D/T)\text{mm s}^{-1}$$

where

$$D(x) = (3/x^3)\int_0^x t^3\,dt/(e^t-1),$$

is the Debye function and θ_D the characteristic Debye temperature The isomer shift at 0K and θ_D were determined as

$$IS(0) = 0.999(3)\text{ mm s}^{-1}$$

$$\theta_D = 211(5)\text{K}$$

The temperature dependence of the magnetic hyperfine field (H) and of the angle θ for MnS_2, $MnSe_2$ and $MnTe_2$ will be discussed in section 4.2.

4.1.2.2 $MnSe_2$ 2% ^{57}Fe Sample

Spectra at various temperatures between 5 - 295K have been measured; the spectra at $T \leqslant T_N$ are shown in Figs. 4.8 and 4.9. Although the observed Mössbauer spectra above T_N showed only one pair of lines, below the transition temperature the spectra clearly indicate the existence of a superposition of two hyperfine structures due to two

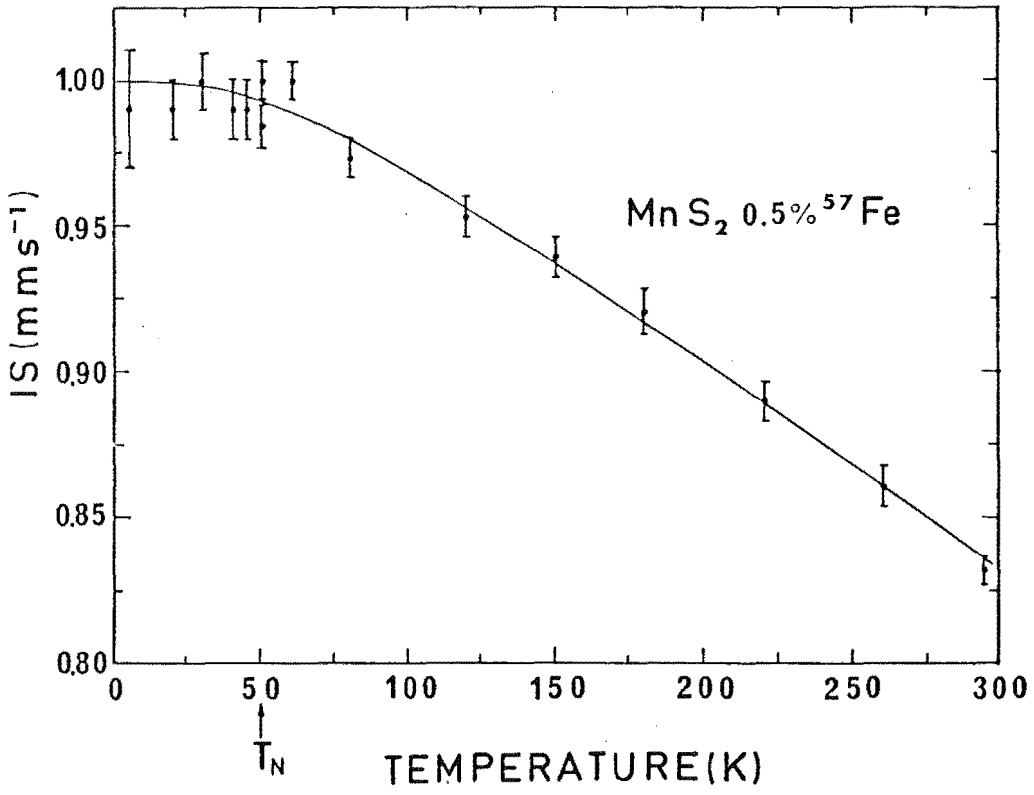

Figure 4.5 Temperature dependence of the isomer shift in MnS_2.

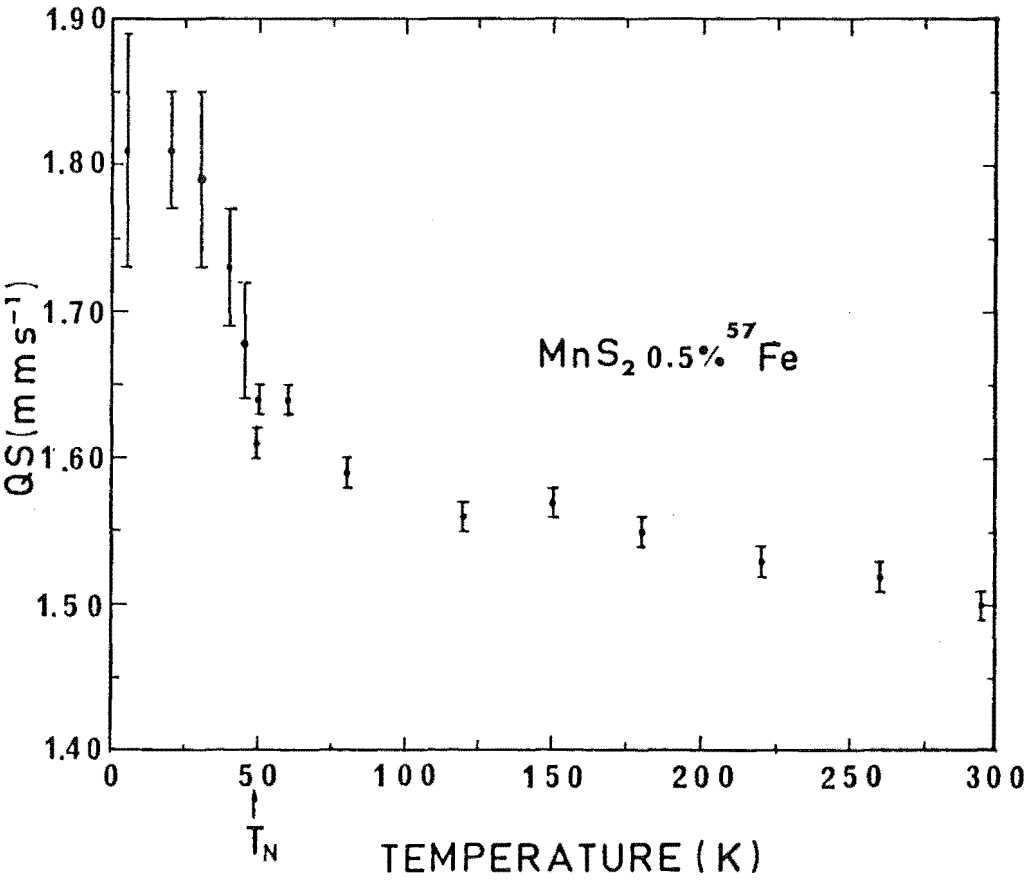

Figure 4.6 Temperature dependence of the quadrupole splitting in MnS_2.

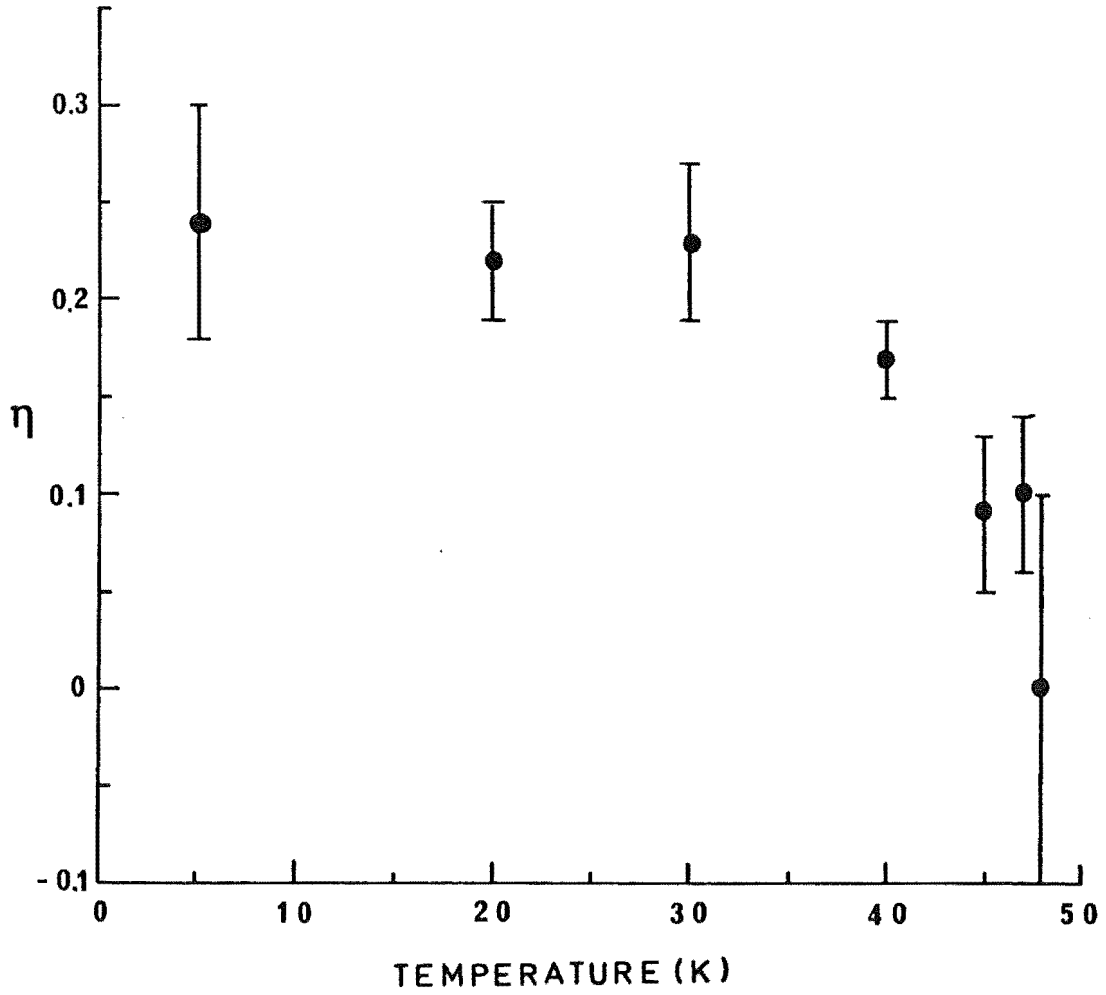

Figure 4.7 Temperature dependence of η in MnS_2 (ϕ = 90°).

Table 4.3 Mössbauer parameters of MnS_2 below T_N ($\phi = 90°$).

Temperature (K)	H (tesla)	QS (mm s^{-1})	IS (mm s^{-1})	η	θ (degree)	Γ (mm s^{-1})	Fractional absorption
5(1)	14.4(4)	1.81(8) 1.1(1)	0.99(2) 0.28(5)	0.24(6)	67(1)	0.43(4) 0.3(1)	0.137(8) 0.015(6)
20	14.5(4)	1.81(4) 0.92(5)	0.99(1) 0.38(4)	0.22(3)	67.5(6)	0.42(2) 0.53(6)	0.142(4) 0.019(2)
30	14.2(4)	1.79(6) 0.92(6)	1.00(1) 0.40(5)	0.23(4)	68(1)	0.41(2) 0.54(8)	0.141(4) 0.024(2)
40	13.6(3)	1.73(4) 0.87(4)	0.99(1) 0.43(2)	0.17(2)	69(1)	0.40(2) 0.47(4)	0.142(4) 0.030(2)
45	12.8(4)	1.68(4) 0.89(4)	0.99(1) 0.46(2)	0.09(4)	70(1)	0.41(2) 0.44(4)	0.144(4) 0.038(2)
47	12.4(4)	1.68(4) 0.87(4)	0.99(1) 0.46(2)	0.10(4)	70(1)	0.38(2) 0.47(4)	0.150(4) 0.039(2)
48	11.6(6)	1.7(1) 1.66(2) 0.64(4)	0.99(2) 0.95(2) 0.54(2)	0.0(1)	71(2)	0.36(6) 0.33(4) 0.26(6)	0.077(8) 0.101(6) 0.037(6)

Table 4.4 Mössbauer parameters of MnS_2 at $T \geqslant T_N$.

Temperature (K)	QS (mm s^{-1})	IS (mm s^{-1})	Γ (mm s^{-1})	Fractional absorption
49	1.61(1) 0.87(3)	0.984(7) 0.43(2) 1.11(4)	0.282(6) 0.37(4) 0.2(1)	0.181(2) 0.037(2) 0.006(2)
50	1.64(1) 0.85(4)	1.000(7) 0.42(2) 1.09(8)	0.261(6) 0.40(6) 0.3(2)	0.184(4) 0.030(4) 0.005(2)
60	1.64(1) 0.79(4)	1.000(7) 0.40(3) 1.10(5)	0.258(8) 0.38(7) 0.2(1)	0.186(4) 0.031(4) 0.007(4)
80	1.59(1) 0.80(3)	0.973(7) 0.43(2) 1.09(6)	0.252(4) 0.42(4) 0.23(15)	0.185(2) 0.029(2) 0.004(2)
120	1.56(1) 0.77(3)	0.953(7) 0.41(2) 1.04(6)	0.243(4) 0.40(4) 0.3(1)	0.182(2) 0.028(2) 0.004(2)
150	1.57(1) 0.77(2)	0.939(6) 0.41(1) 1.03(2)	0.232(2) 0.42(2) 0.40(7)	0.185(2) 0.028(2) 0.006(1)
180	1.55(1) 0.77(2)	0.921(7) 0.38(1) 1.02(3)	0.232(4) 0.42(4) 0.32(7)	0.180(2) 0.028(2) 0.008(2)
220	1.53(1) 0.78(3)	0.890(7) 0.35(2) 0.97(4)	0.221(4) 0.42(5) 0.3(1)	0.172(2) 0.026(2) 0.007(2)
260	1.52(1) 0.77(2)	0.861(7) 0.34(2) 0.98(2)	0.222(4) 0.40(4) 0.25(7)	0.161(2) 0.027(2) 0.008(2)
296(1)	1.50(1) 0.77(1)	0.832(5) 0.324(6) 0.95(2)	0.219(2) 0.42(2) 0.267(4)	0.157(1) 0.024(1) 0.005(1)

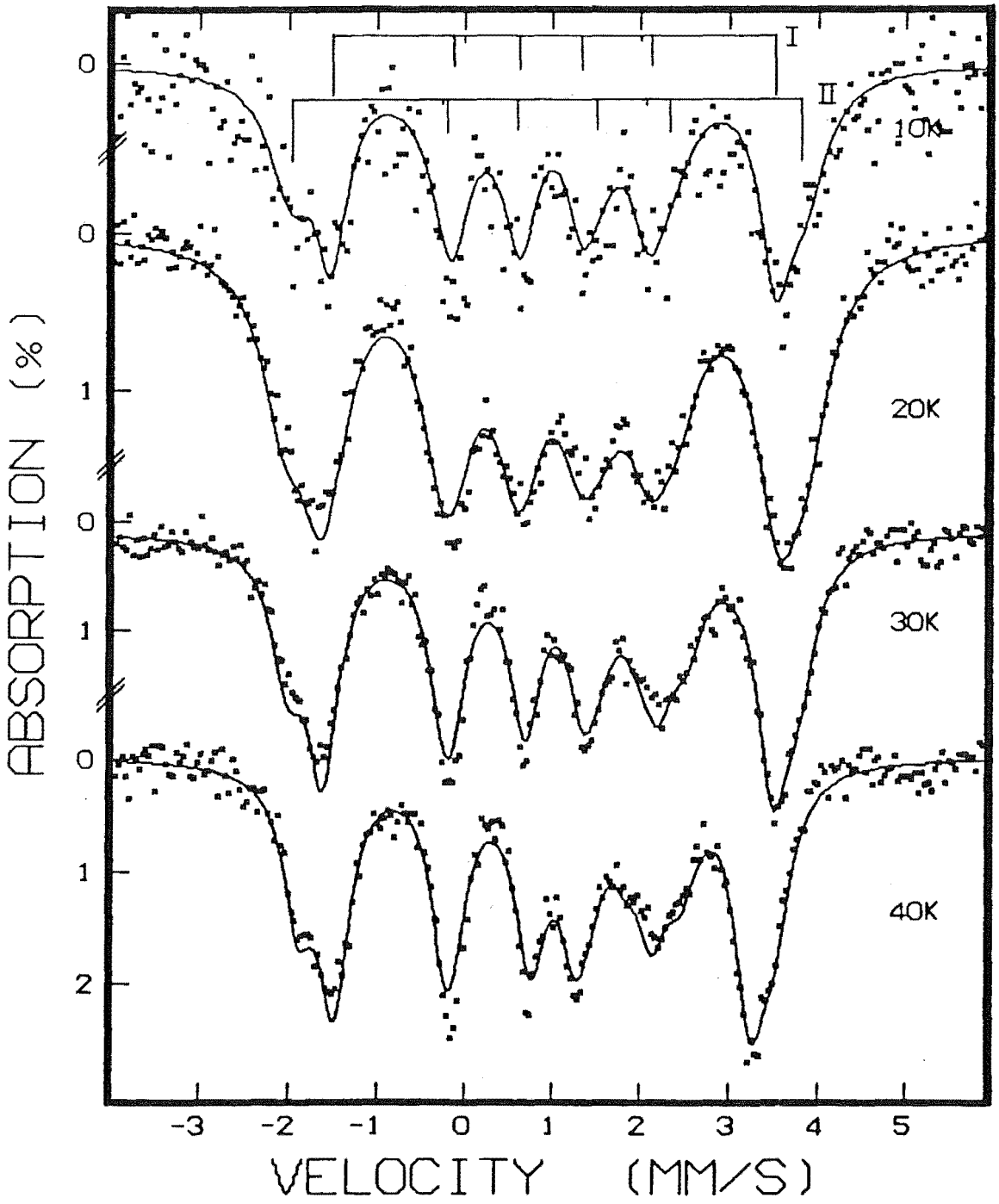

Figure 4.8 Mössbauer spectra of $MnSe_2$ 2% ^{57}Fe below T_N.

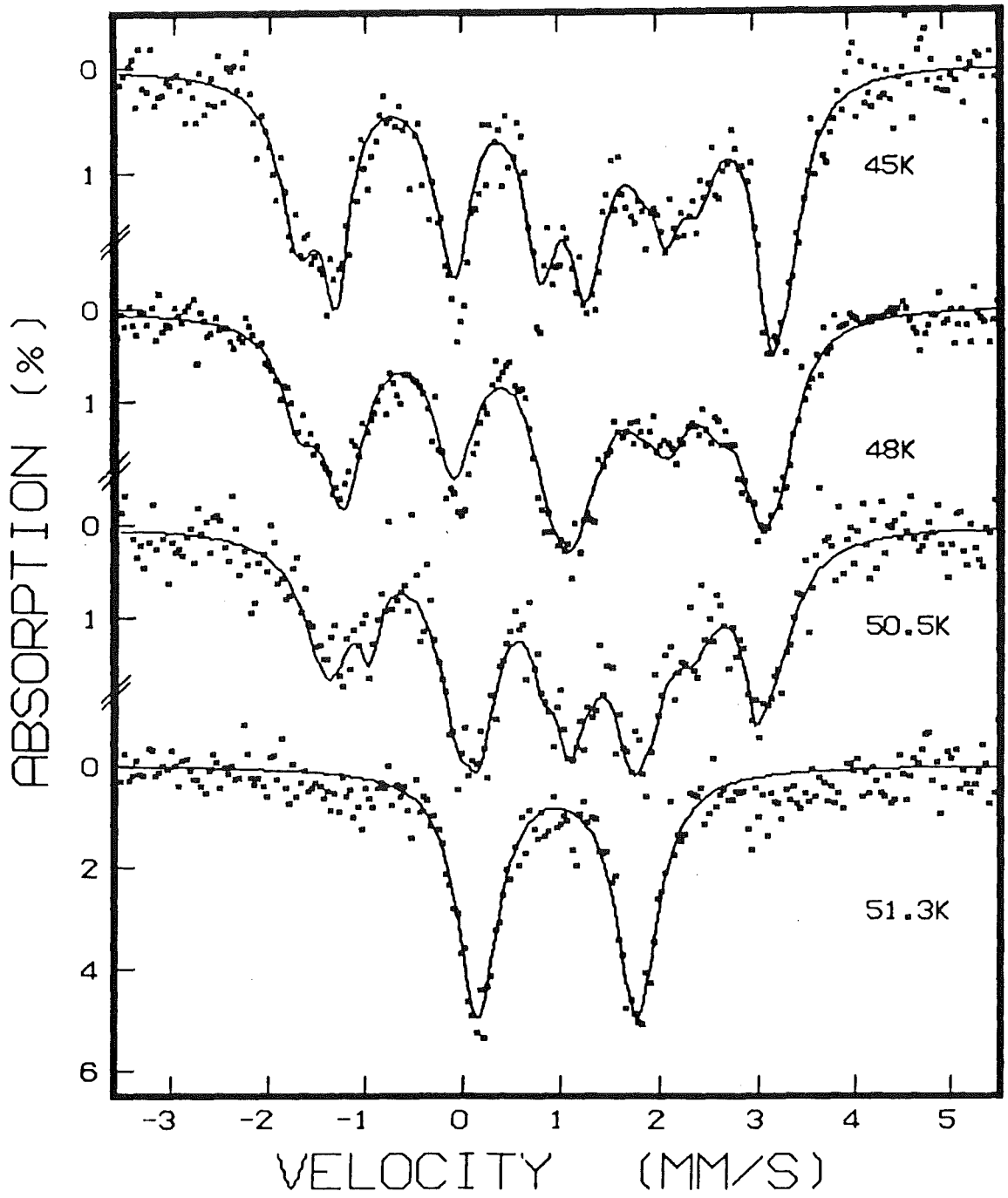

Figure 4.9 Mössbauer spectra of $MnSe_2$ 2% ^{57}Fe at $T \leqslant T_N$.

inequivalent Fe^{2+} sites. We decomposed the complicated spectra into two different hyperfine structures and labelled one of the sites as site I and the other as site II. The relative intensity of site I is approximately twice that of site II. The double spectra of $MnSe_2$ which were not observed in MnS_2 and $MnTe_2$, are almost certainly due to the two different second nearest neighbour environments of the cations in magnetically ordered $MnSe_2$, as explained in section 1.3 and as will be discussed further in section 4.2. The fitted data showed that the values of H and θ of site I and site II are different, but that all other parameters such as IS and QS are the same within experimental accuracy. The stick diagrams for both sites are drawn for the spectra at 10K. The Mössbauer parameters are presented in Tables 4.5 and 4.6. The spectrum at 50.5K just below T_N (51K) showed an extra pair of lines, similar to the corresponding spectrum in MnS_2. The temperature dependence of the isomer shift and of the quadrupole splitting data for both sites are plotted in Figs. 4.10 and 4.11 respectively and the variation of η with temperature for site I and site II is plotted in Figs. 4.12 and 4.13 respectively. The calculated isomer shift and the Debye temperature of the sample were determined. The isomer shift at 0K, and θ_D, are

$$IS(0) = 0.961(3) \text{ mm s}^{-1}$$

$$\theta_D = 306(5)\text{K}$$

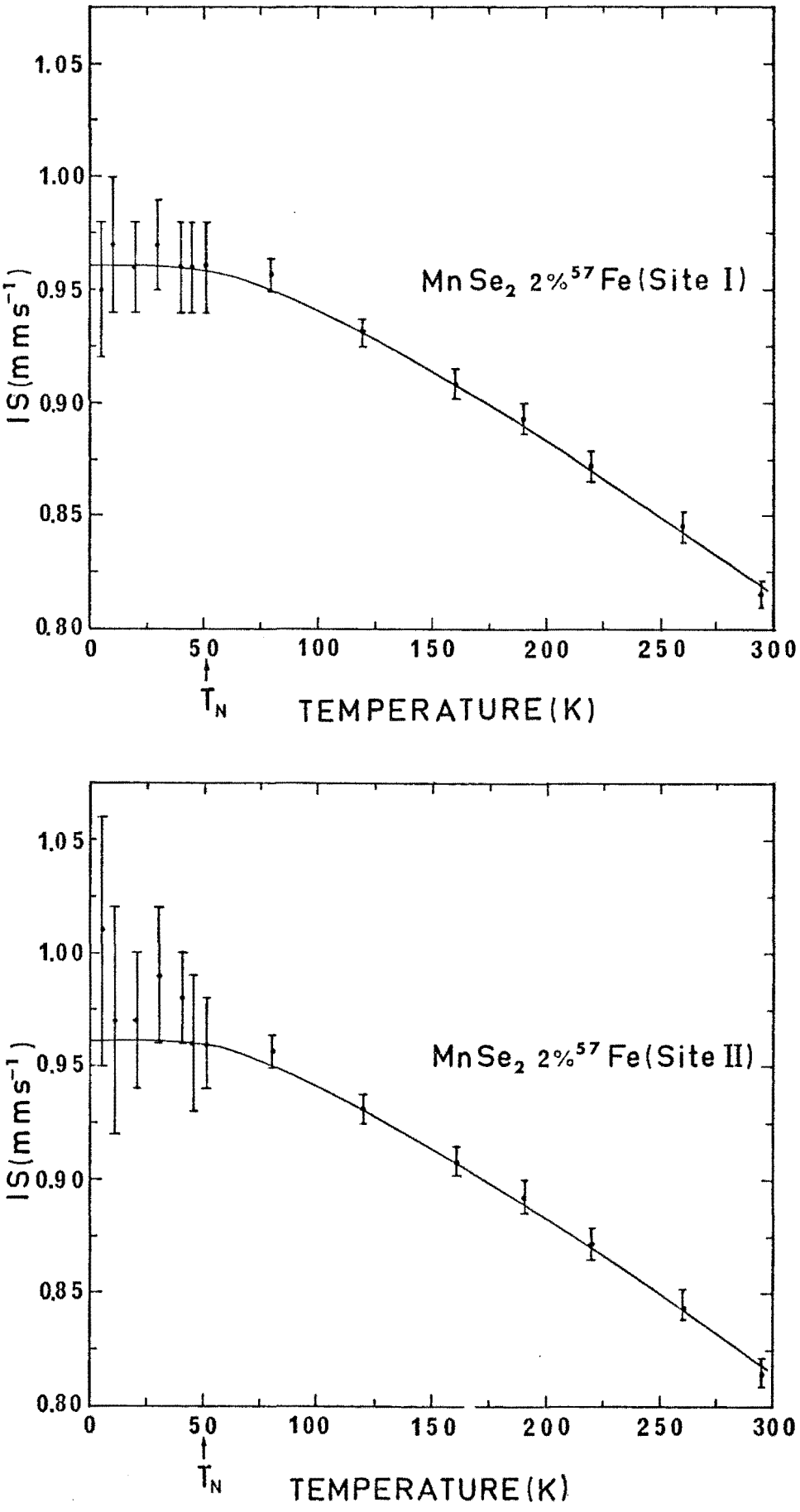

Figure 4.10 Temperature dependences of the isomer shifts in $MnSe_2$ 2% ^{57}Fe.

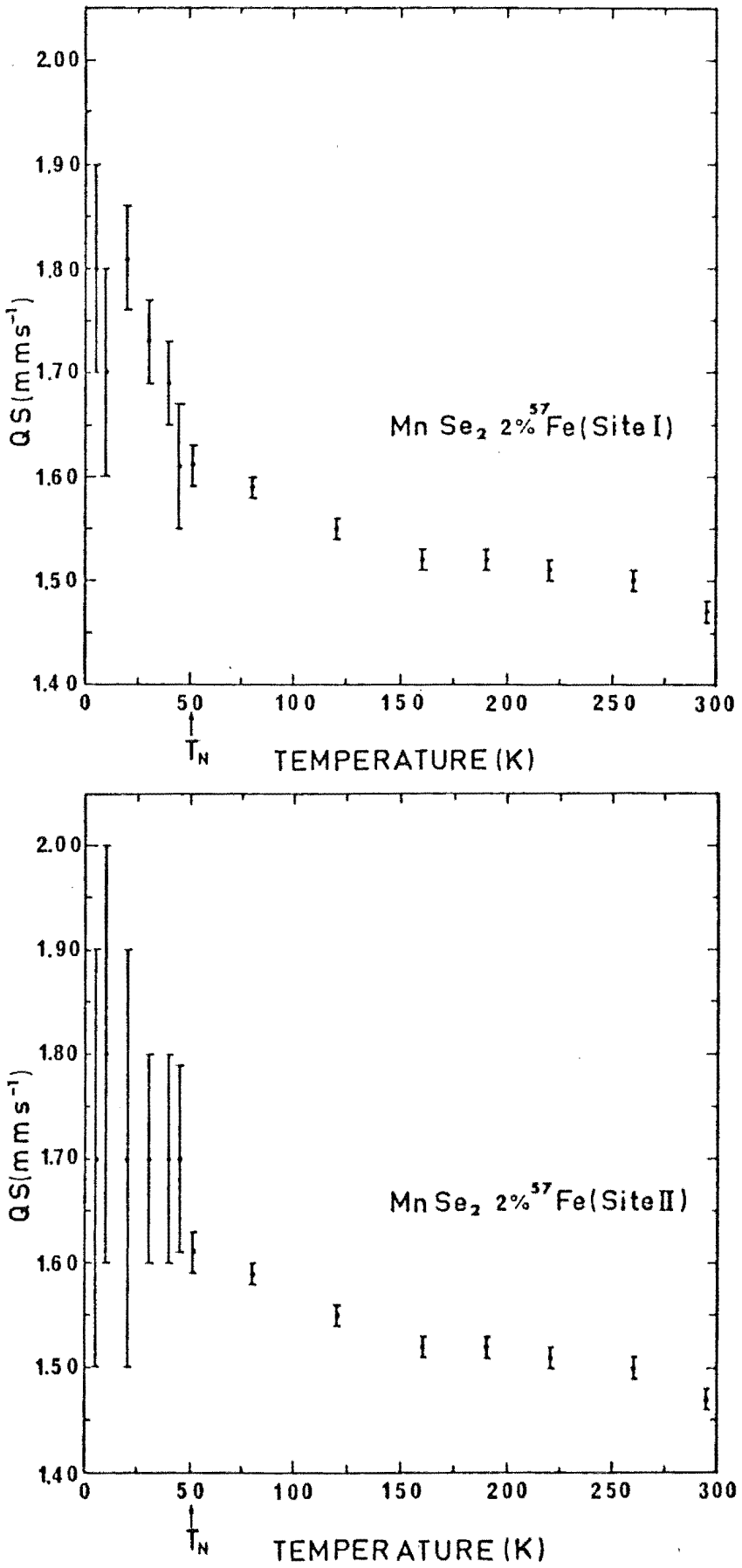

Figure 4.11 Temperature dependences of the quadrupole splittings in $MnSe_2$ 2% ^{57}Fe.

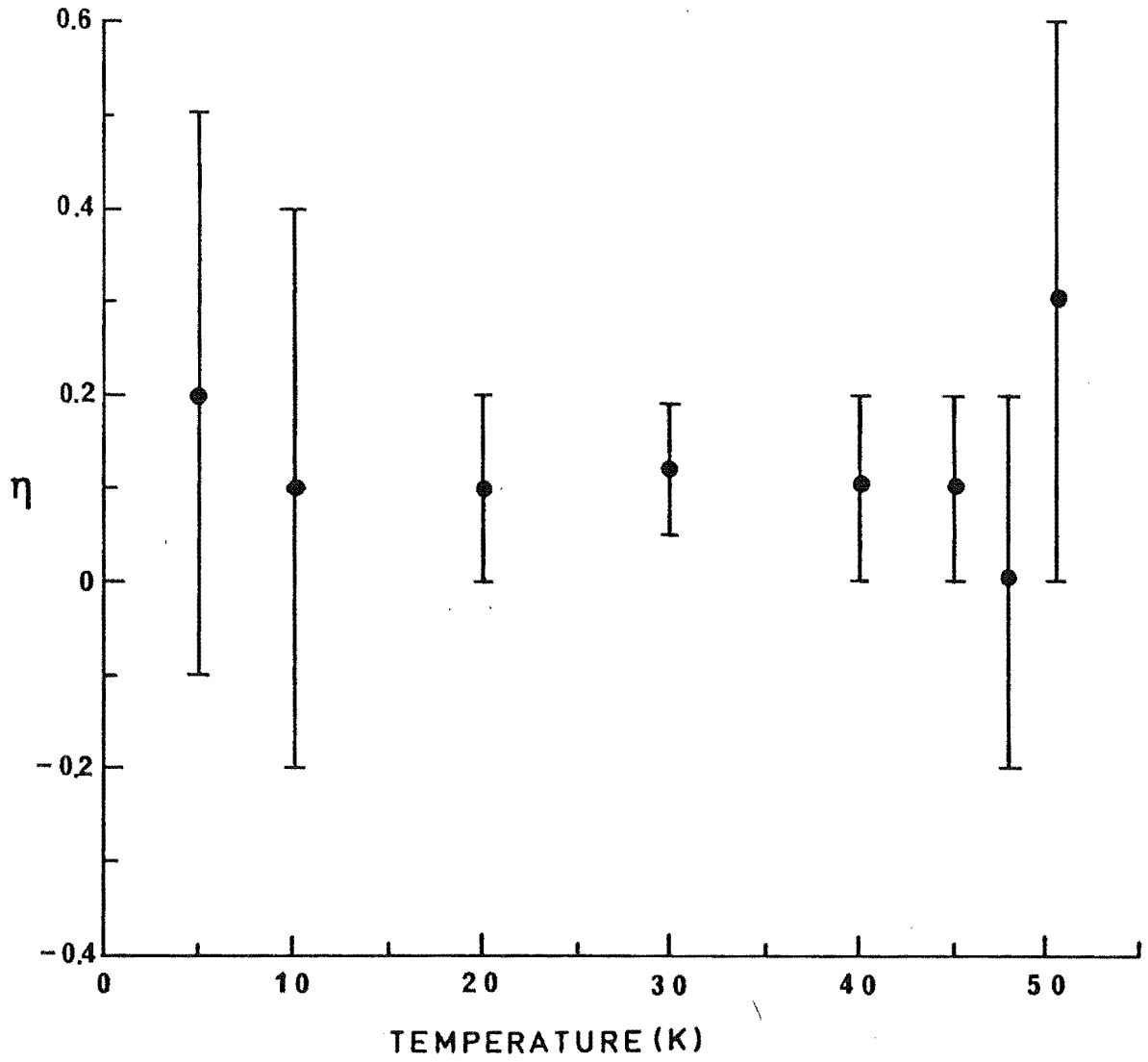

Figure 4.12 Temperature dependence of η in $MnSe_2$ 2% ^{57}Fe (site I).

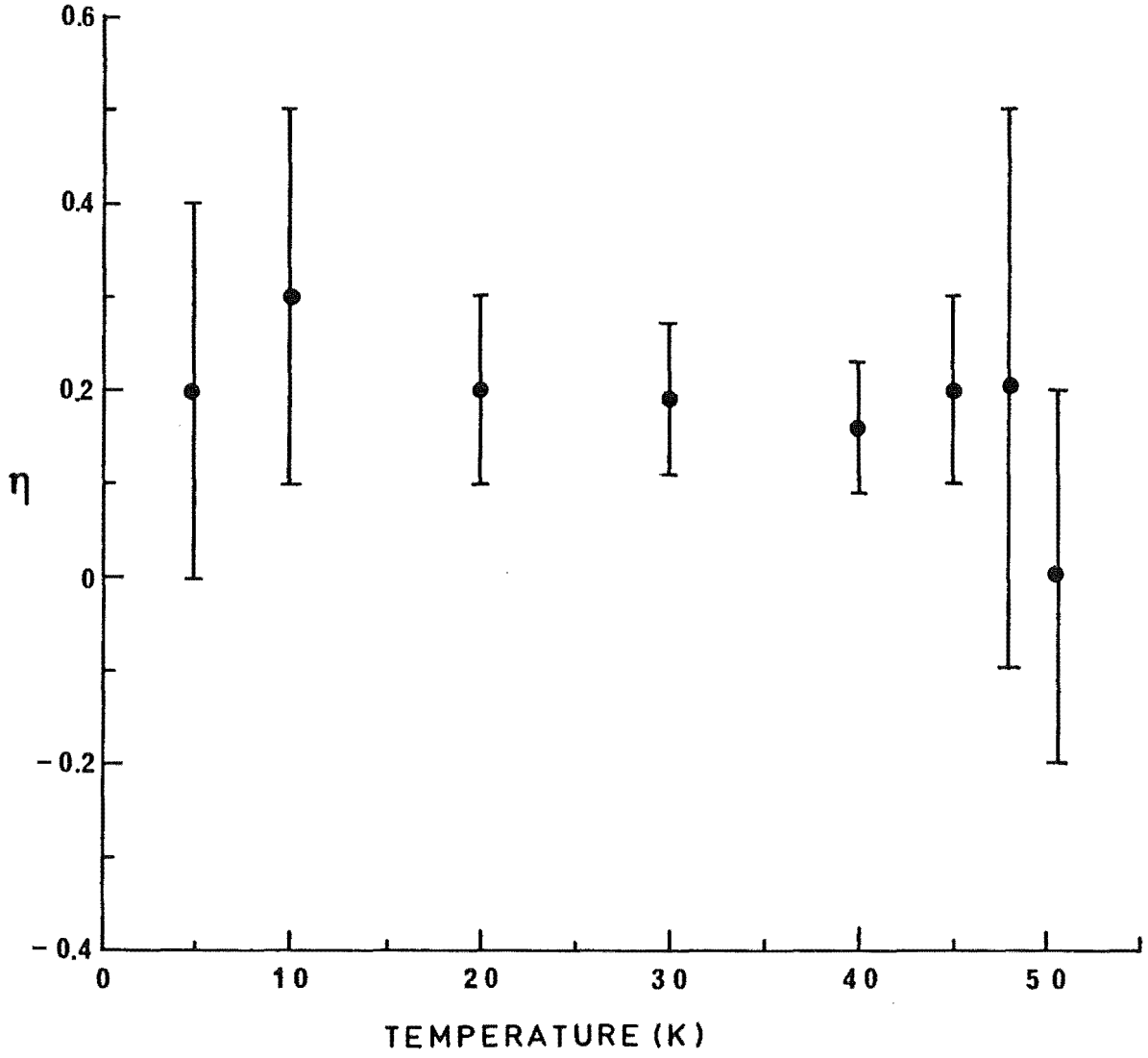

Figure 4.13 Temperature dependence of η in $MnSe_2$ 2% ^{57}Fe (site II).

Table 4.5 Mössbauer parameters of $MnSe_2$ 2% ^{57}Fe below T_N.

Temperature (K)	Magnetic site	H (tesla)	QS (mm s^{-1})	IS (mm s^{-1})	η	ϕ (degree)	θ (degree)	Γ (mm s^{-1})	Fractional absorption
5(1)	I	12.2(1.0)	1.8(1)	0.95(3)	0.2(3)	90	53(4)	0.21(16)	0.07(3)
	II	14.6(1.1)	1.7(2)	1.01(5)	0.2(2)	90	60(4)	0.62(16)	0.07(2)
10	I	12.4(1.0)	1.7(1)	0.97(3)	0.1(3)	90	53(2)	0.40(12)	0.07(2)
	II	14.6(1.6)	1.8(2)	0.97(5)	0.3(2)	90	57(3)	0.63(20)	0.05(2)
20	I	12.6(1.0)	1.81(5)	0.96(2)	0.1(1)	90	54(2)	0.62(6)	0.07(2)
	II	15.6(1.5)	1.7(2)	0.97(3)	0.2(1)	90	58(3)	0.60(8)	0.04(2)
30	I	12.7(5)	1.73(4)	0.97(2)	0.12(7)	90	56(1)	0.42(4)	0.089(8)
	II	15.0(1.0)	1.7(1)	0.99(3)	0.19(8)	90	62(2)	0.46(7)	0.048(6)
40	I	11.8(6)	1.69(4)	0.96(2)	0.1(1)	90	59(1)	0.39(3)	0.088(6)
	II	14.3(8)	1.7(1)	0.98(2)	0.16(7)	90	65(1)	0.43(6)	0.057(6)
45	I	10.8(8)	1.61(6)	0.96(2)	0.1(1)	90	59(2)	0.33(6)	0.08(2)
	II	12.8(1.0)	1.7(1)	0.96(3)	0.2(1)	90	67(2)	0.47(9)	0.06(2)
48	I	10.1(5)	1.67(4)	0.95(2)	0.0(2)	0	61(2)	0.52(5)	0.081(8)
	II	12.6(1.2)	1.8(2)	1.00(5)	0.2(3)	0	73(3)	0.44(12)	0.038(6)
50.5	I	9.5(1.0)	1.6(1)	0.97(3)	0.3(3)	0	56(5)	0.23(14)	0.04(2)
	II	10.9(1.0)	1.7(1)	0.98(3)	0.0(2)	0	67(4)	0.59(12)	0.06(2)
			1.55(3)	0.94(3)				0.47(10)	0.033(4)

Table 4.6 Mössbauer parameters of $MnSe_2$ 2% ^{57}Fe at $T \geqslant T_N$.

Temperature (K)	QS (mm s^{-1})	IS (mm s^{-1})	Γ (mm s^{-1})	Fractional absorption
51.3	1.61(2)	0.96(2)	0.50(4)	0.096(4)
80	1.59(1)	0.956(7)	0.281(2)	0.161(2)
120	1.55(1)	0.931(6)	0.257(2)	0.159(2)
160	1.52(1)	0.908(7)	0.249(4)	0.152(2)
190	1.52(1)	0.893(7)	0.249(6)	0.151(2)
220	1.51(1)	0.872(7)	0.245(4)	0.145(2)
260	1.50(1)	0.845(7)	0.239(8)	0.142(2)
295(1)	1.47(1)	0.815(6)	0.241(4)	0.151(2)

4.1.2.3 $MnSe_2$ 20% Fe Sample

Five spectra of this sample were recorded at $T \leqslant T_N$ (85K). The least squares fitted data (assuming ϕ=0) are listed in Table 4.7 and the spectra are shown in Fig. 4.14. The stick diagram for the spectrum at the lowest recorded temperature is drawn at the top of Fig. 4.14. The spectrum at 80K was fitted with $\eta = 0$.

4.1.2.4 $MnTe_2$ 2% ^{57}Fe Sample

Mössbauer spectra were recorded at a number of temperatures between 8K and 294K and the spectra below T_N (except 90.5K spectrum) were fitted with a bunch of lines (assuming $\phi = 0°$). Although spectra above T_N were fitted with 2 pairs of lines, below the Néel temperature the extra pair due to $FeTe_2$ could not be detected in the fit, perhaps because of its very small line intensity. Representative spectra for $T \leqslant T_N$ are shown in Figs. 4.15 through 4.17 and the fitted data below T_N are given in Table 4.8. Data for $T \geqslant T_N$ are listed in Table 4.9. The spectrum at 90.5K just near T_N showed an extra pair of lines similar to the extra pair observed in MnS_2 and $MnSe_2$. The stick diagram for the bunch is drawn for the 8K spectrum in Fig. 4.15.

When H is parallel to one of the EFG principal axes, there is no ambiguity of QS,η,θ and ϕ values[45], and this is the case with the low temperature spectra in $MnTe_2$. The ambiguous solutions for the 60K spectrum showed ranges of, η = 0.05 - 0.15, θ = 11.2° - 11.8°, ϕ = 6.5° - 68.5° and QS = 1.36 - 1.37 mm s^{-1}, and the sign of the QS was taken

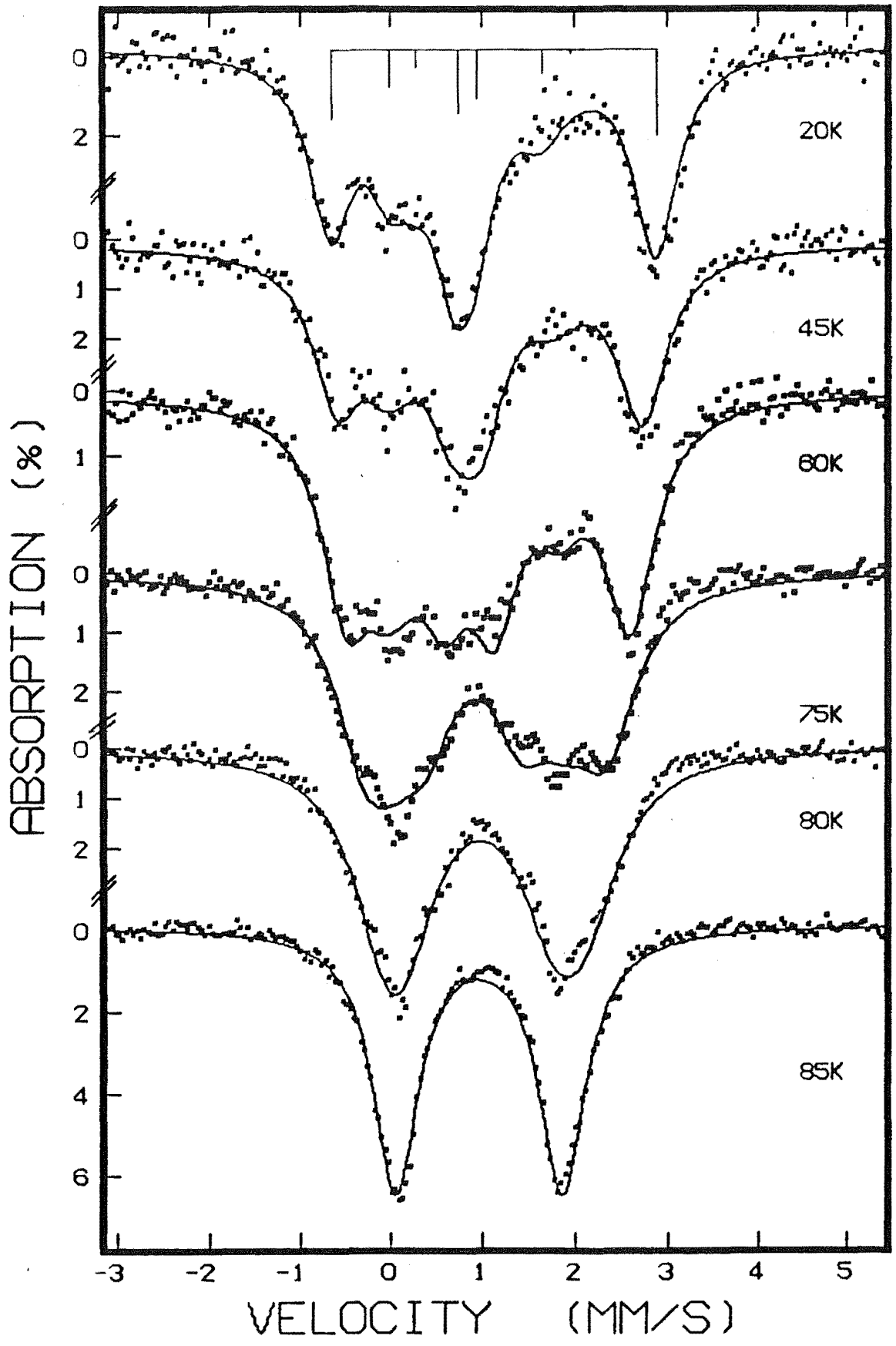

Figure 4.14 Mössbauer spectra of $MnSe_2$ 20% Fe at $T \leqslant T_N$.

Table 4.7 Mössbauer parameters of $MnSe_2$ 20% Fe at $T \leqslant T_N$.

Temperature (K)	H (tesla)	QS (mm s^{-1})	IS (mm s^{-1})	η	θ (degree)	Γ (mm s^{-1})	Fractional absorption
20	7.9(2)	1.49(4)	0.95(2)	0.30(8)	36(2)	0.57(4)	0.21(1)
45	6.3(2)	1.70(6)	0.94(2)	0.4(1)	37(2)	0.64(4)	0.142(8)
60	5.6(2)	1.63(4)	0.95(2)	0.6(1)	44(2)	0.66(4)	0.143(4)
75	3.9(4)	1.58(9)	0.96(2)	0.8(4)	56(8)	0.76(4)	0.111(6)
80	1.4(5)	1.86(2)	0.96(2)	0	38(16)	0.86(8)	0.101(6)
85		1.79(1)	0.93(1)			0.61(2)	0.126(2)

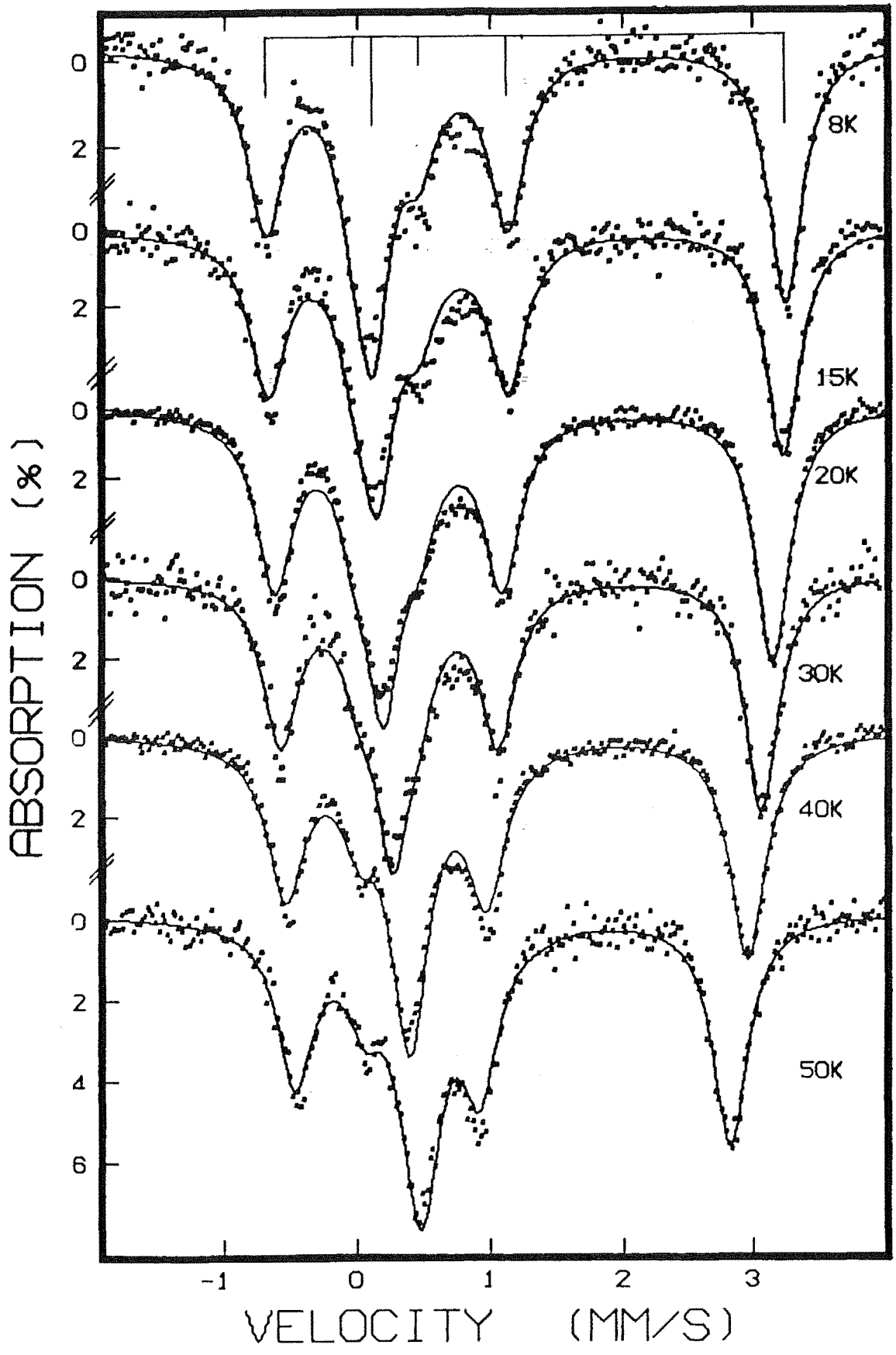

Figure 4.15 Mössbauer spectra of $MnTe_2$ 2% ^{57}Fe below T_N.

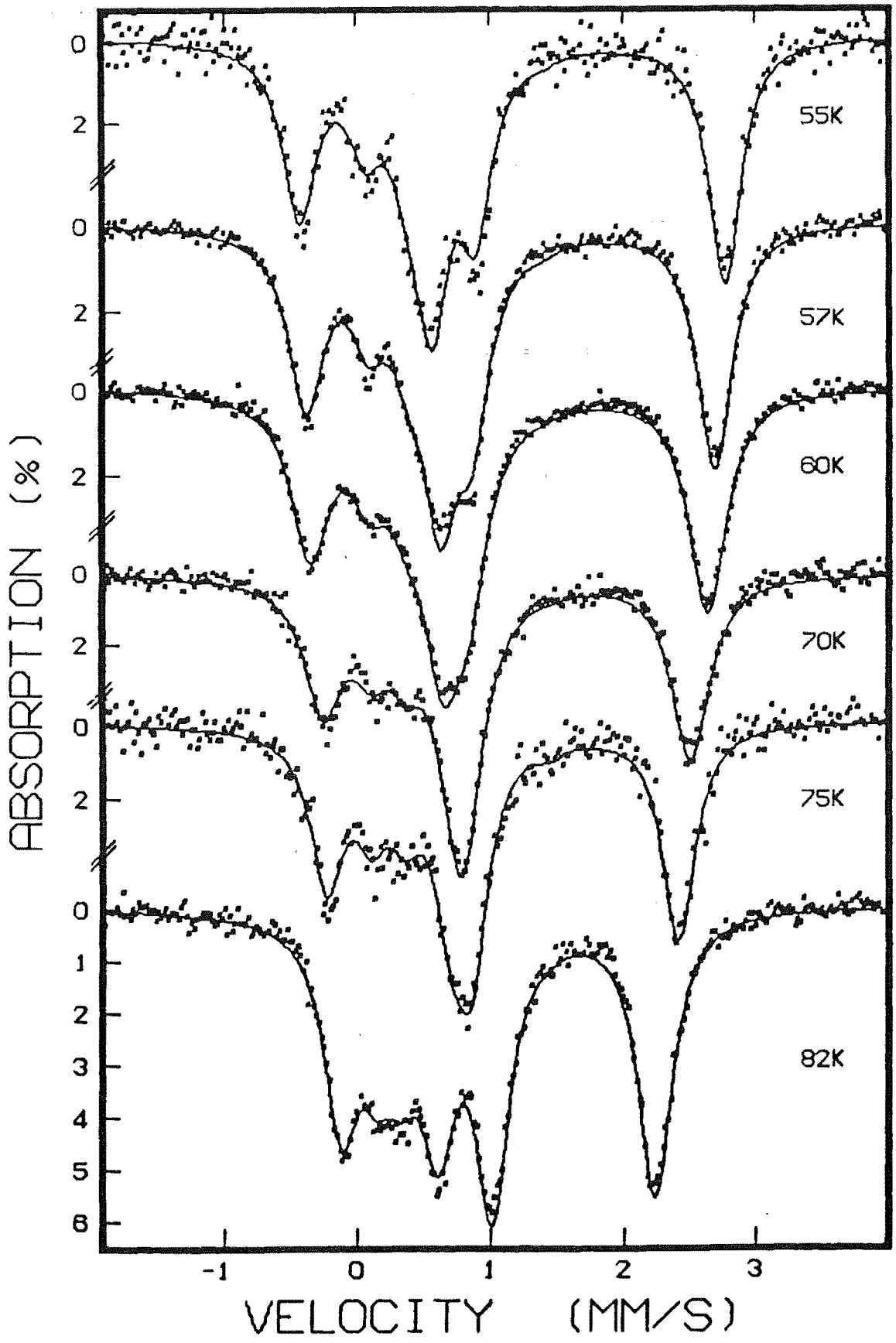

Figure 4.16 Mössbauer spectra of $MnTe_2$ 2% ^{57}Fe below T_N.

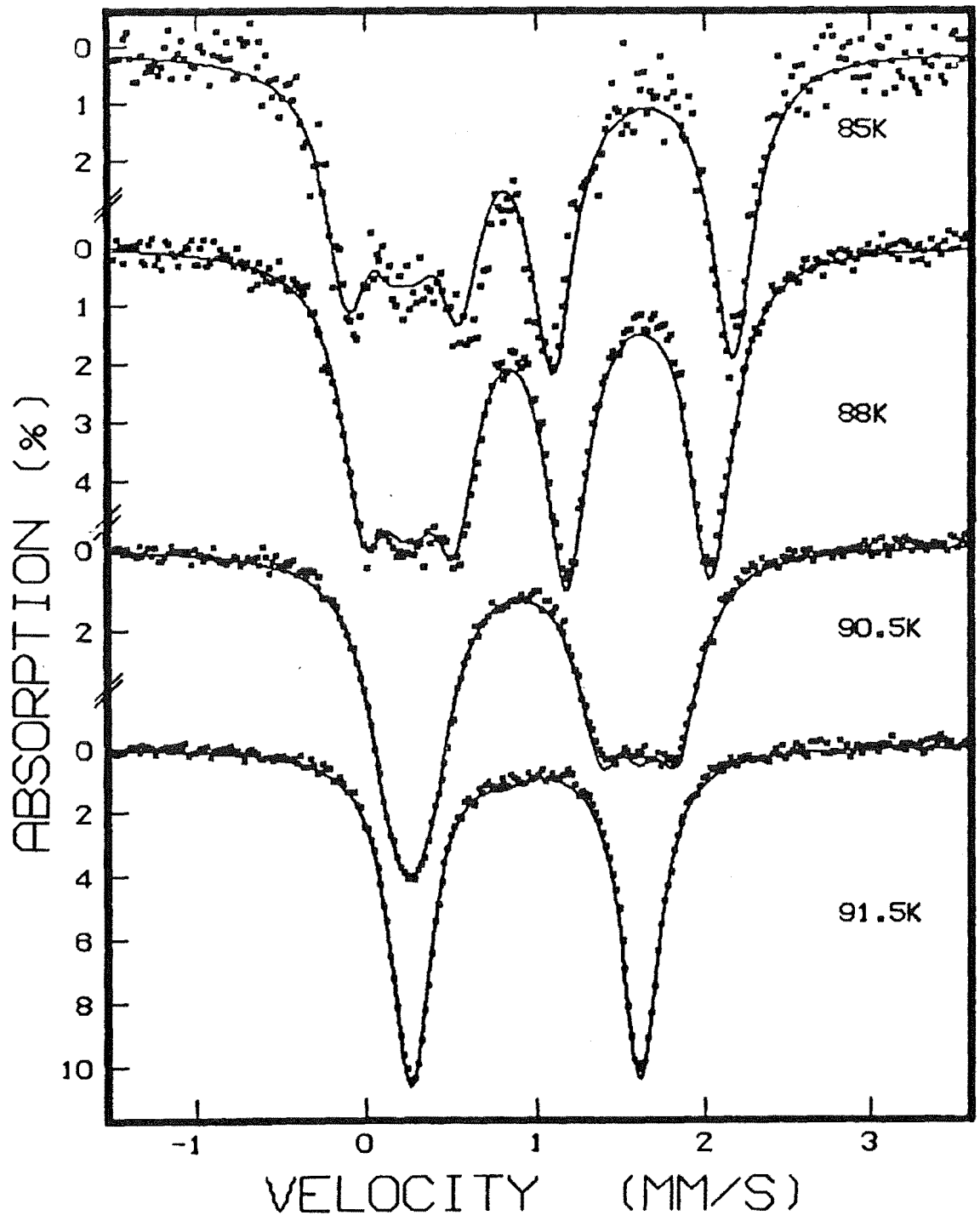

Figure 4.17 Mössbauer spectra of $MnTe_2$ 2% ^{57}Fe at $T \leqslant T_N$.

to be positive (see section 4.1.2.1). In all the spectra below T_N, the ambiguity range of θ is very small.

The temperature dependence of the isomer shift, the quadrupole splitting and the η data are plotted in Figs. 4.18, 4.19 and 4.20 respectively. The IS at 0K and θ_D of this sample were determined as

$$IS(0) = 0.937(3) \text{ mm s}^{-1}$$

$$\theta_D = 242(5)\text{K}.$$

4.1.3 Iron Concentration Dependent Transition Temperatures in $MnSe_2$

From Mössbauer experiments we determined the Fe-concentration dependence of the transition temperature in $MnSe_2$, and the result is presented in Fig. 4.21. $MnSe_2$ was the only compound we examined in this way; the Mössbauer spectra of MnS_2 + $\frac{1}{2}$ at. % ^{57}Fe and $MnTe_2$ 2 at. % ^{57}Fe showed the presence of the corresponding Fe compound, showing that the solubility limits had been reached.

We also measured the Fe-concentration dependence of the Mössbauer parameters of $MnSe_2$ at 20K (Fig. 4.22), and the concentration dependence of H is plotted in Fig. 4.23, that of θ in Fig. 4.24. Only the data for the strongest absorbing site is plotted.

The Mössbauer spectra we measured fell into 3 distinct groups. The low-concentration samples (1 and 2%) showed two inequivalent Fe^{2+} sites (as mentioned in section 4.1.2.2)

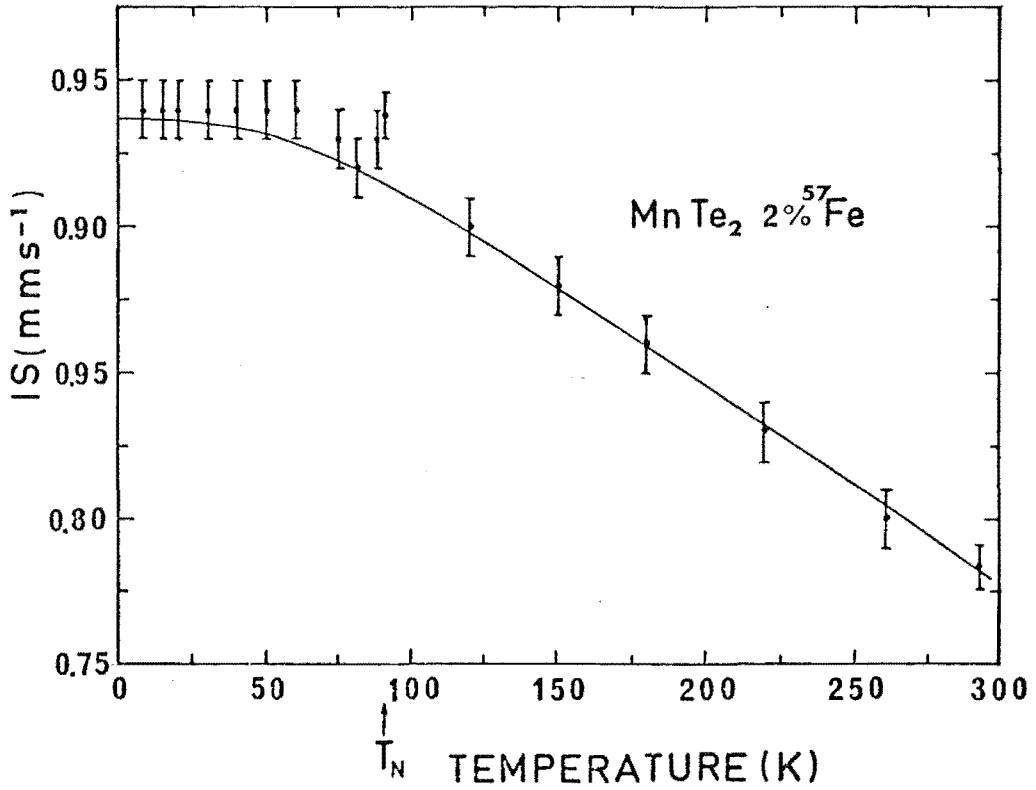

Figure 4.18 Temperature dependence of the isomer shift in $MnTe_2$.

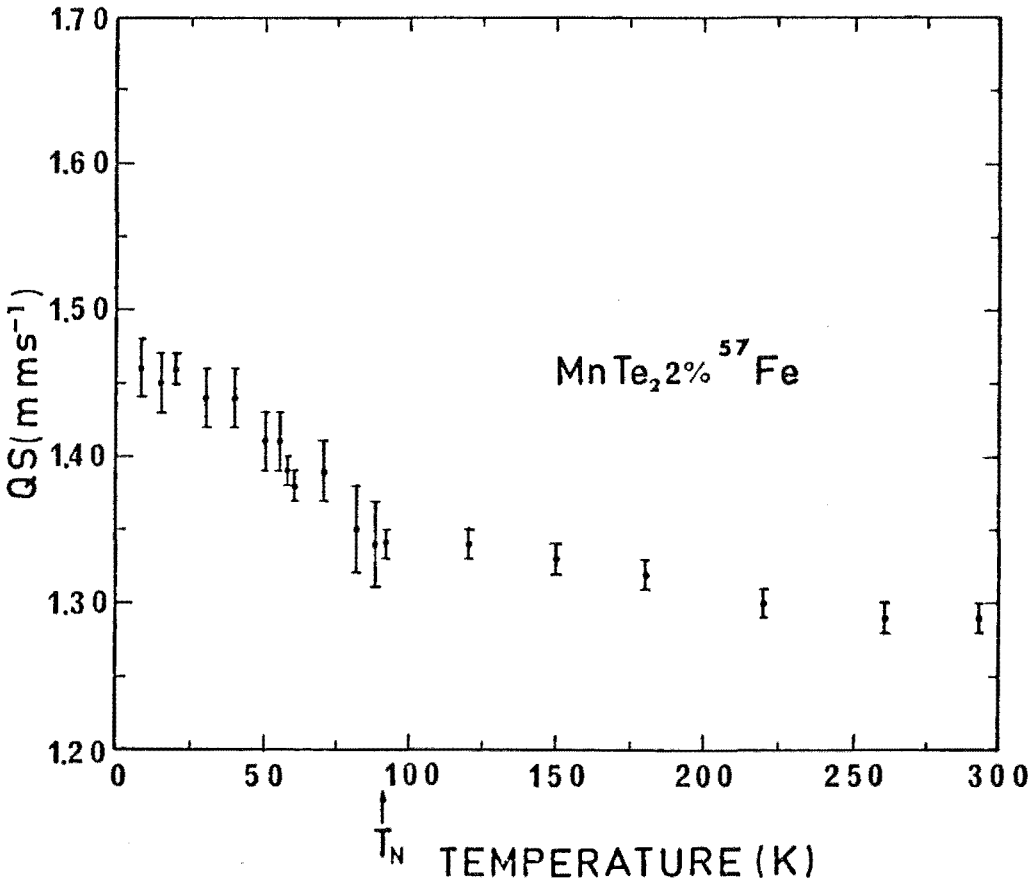

Figure 4.19 Temperature dependence of the quadrupole splitting in $MnTe_2$.

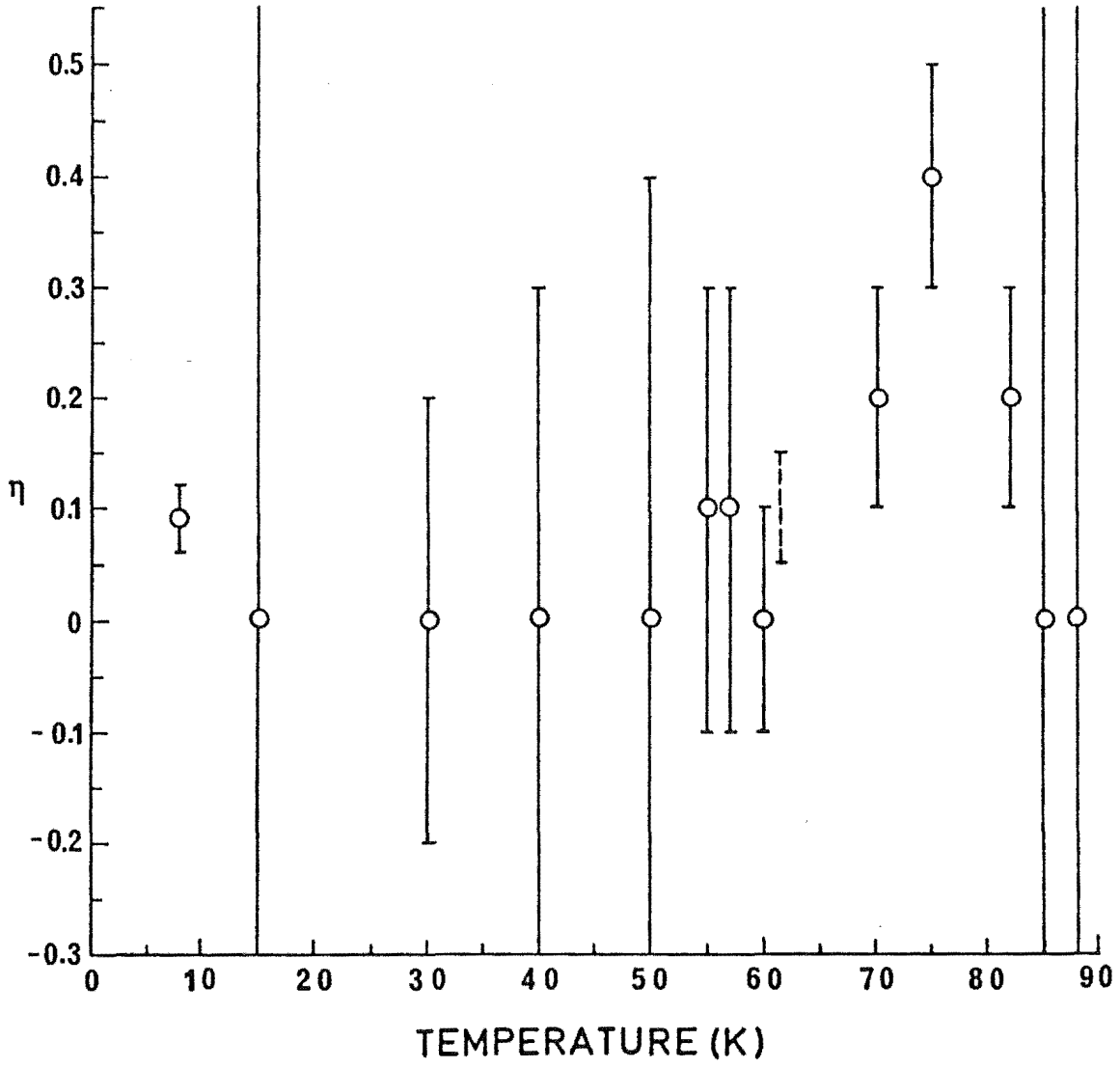

Figure 4.20 Temperature dependence of η in $MnTe_2$. Dashed vertical bar represents the range of η obtained from the ambiguous solutions.

Table 4.8 Mössbauer parameters of $MnTe_2$ below T_N.

Temperature (K)	H (tesla)	QS (mm s^{-1})	IS ($\pm$0.01) (mm s^{-1})	η	θ (degree)	Γ (mm s^{-1})	Fractional absorption
8(1)	9.7(1)	1.46(2)	0.94	0.09(3)	2(5)	0.32(2)	0.237(8)
15	9.6(1)	1.45(2)	0.94	0(3)	6(3)	0.32(2)	0.234(6)
20	9.3(1)	1.46(1)	0.94	0	2(4)	0.32(1)	0.293(6)
30	8.8(1)	1.44(2)	0.94	0.0(2)	6(3)	0.32(2)	0.231(8)
40	8.0(1)	1.44(2)	0.94	0.0(3)	7(2)	0.34(1)	0.218(4)
50	7.3(1)	1.41(2)	0.94	0.0(4)	11(2)	0.33(2)	0.224(6)
55	6.9(1)	1.41(2)	0.94	0.1(2)	12(2)	0.30(2)	0.240(8)
57	6.5(1)	1.39(1)	0.94	0.1(2)	13(2)	0.32(1)	0.230(4)
60	6.2(1)	1.38(1)	0.94	0.0(1)	12(2)	0.35(1)	0.206(4)
70	5.3(1)	1.39(2)	0.94	0.2(1)	10(3)	0.34(2)	0.204(4)
75	5.0(1)	1.34(4)	0.93	0.4(1)	16(3)	0.29(2)	0.236(8)
82	3.8(1)	1.35(3)	0.92	0.2(1)	13(2)	0.31(1)	0.216(4)
85	3.4(2)	1.39(4)	0.92	0.0(8)	15(7)	0.30(2)	0.21(1)
88	2.7(1)	1.34(3)	0.93	0(2)	16(9)	0.31(1)	0.216(4)
90.5	1.5(2)	1.34(1) 1.35(2)	0.93 0.93	0	17(6)	0.32(2) 0.31(9)	0.16(2) 0.05(2)

Table 4.9 Mössbauer parameters of $MnTe_2$ at $T \geqslant T_N$.

Temperature (K)	QS (mm s^{-1})	IS (mm s^{-1})	Γ (mm s^{-1})	Fractional absorption
91.5	1.34(1) 0.69(6)	0.938(8) 0.47(2)	0.272(4) 0.30(8)	0.202(2) 0.009(2)
95	1.34(1) 0.65(6)	0.935(8) 0.46(3)	0.268(4) 0.32(8)	0.205(2) 0.011(2)
120	1.34(1) 0.5(1)	0.90(1) 0.59(6)	0.255(4) 0.5(2)	0.201(2) 0.006(2)
150	1.33(1) 0.5(1)	0.88(1) 0.56(6)	0.250(6) 0.3(2)	0.197(4) 0.008(4)
180 *	1.32(1)	0.86(1)	0.246(6)	0.188(2)
220	1.30(1) 0.5(1)	0.83(1) 0.50(5)	0.243(6) 0.4(2)	0.178(4) 0.007(2)
260 *	1.29(1)	0.80(1)	0.238(4)	0.168(2)
293(1)	1.29(1) 0.48(7)	0.784(8) 0.54(4)	0.234(2) 0.7(2)	0.172(1) 0.006(1)

* Second pair could not be detected in the fit, probably because of its small line intensity.

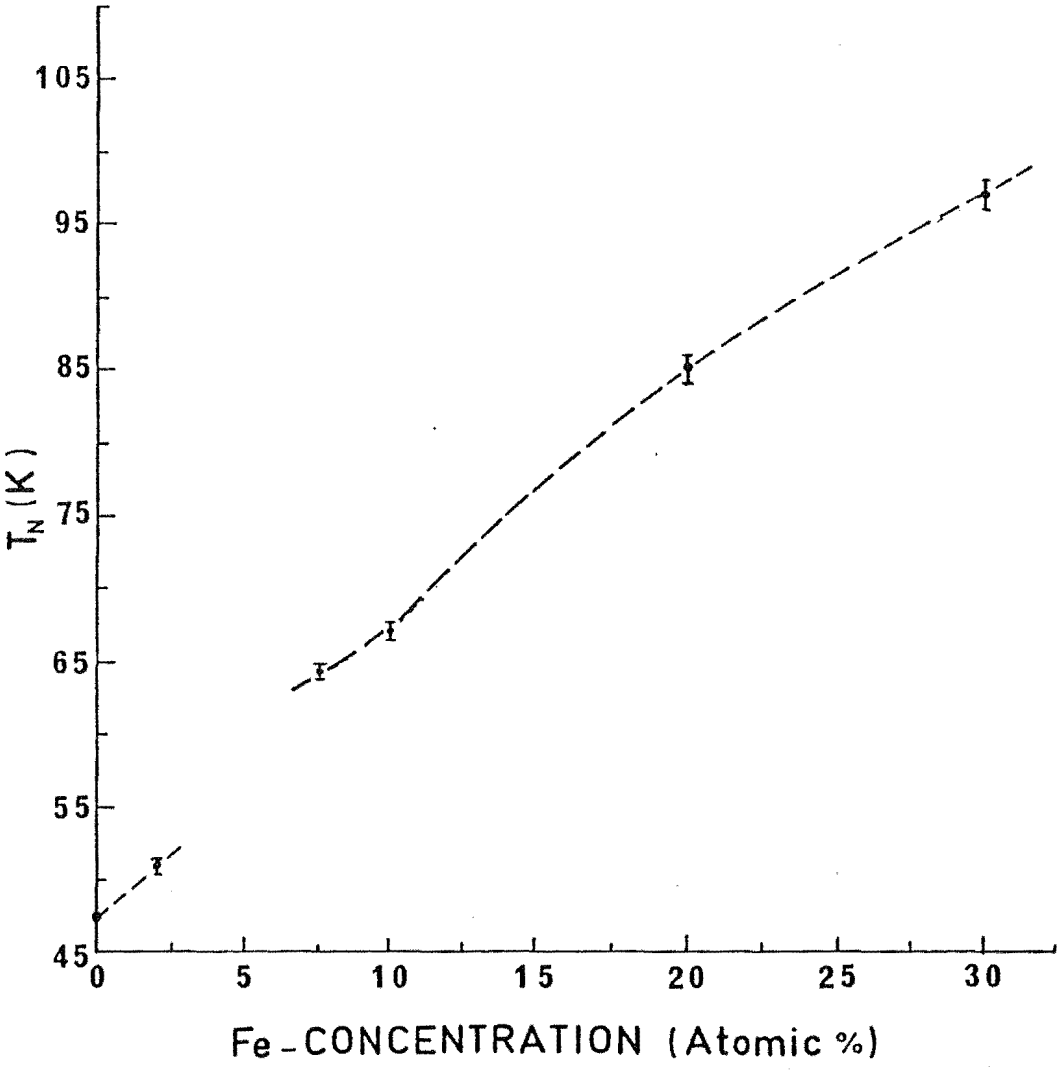

Figure 4.21 Iron concentration dependent Néel temperature of $MnSe_2$. The broken line is a guide to the eye only.

and accordingly were fitted with 2 bunches of lines with different magnetic fields. The 20 and 30 at. % Fe samples showed only a single bunch of lines; H and θ were quite different from their values in the 1 at. % and 2 at. % samples. The intermediate concentration samples (5, 7.5 and 10 at. % Fe) showed the combined effect of high and low concentrations i.e. the spectra were a superposition of three hyperfine structures corresponding to the two different spin arrangementsbeing present in the same sample. So these spectra were fitted with 3 bunches of lines. The 5 at. % and 7.5 at. % spectra clearly established that the lower as well as the higher concentration magnetic phase were present in these samples. Since a 3 bunch fit was quite complicated, due to the large number of variables, we constrained η to be equal to zero in each bunch to reduce the number of variables. The stick diagram for 1 at. % ^{57}Fe sample spectrum with 2 bunches of lines and for 30% Fe sample spectrum with one bunch of lines are drawn (as site III) in Fig. 4.22. The spectrum for the intermediate concentration samples was the sum of the spectra of these two groups. The fitted data are presented in Table 4.10.

4.2 ANALYSIS OF EXPERIMENTAL DATA

In this section we will show that the temperature dependence of the magnetic hyperfine field (H) and the hyperfine angle (θ) can be explained in terms of the crystal-

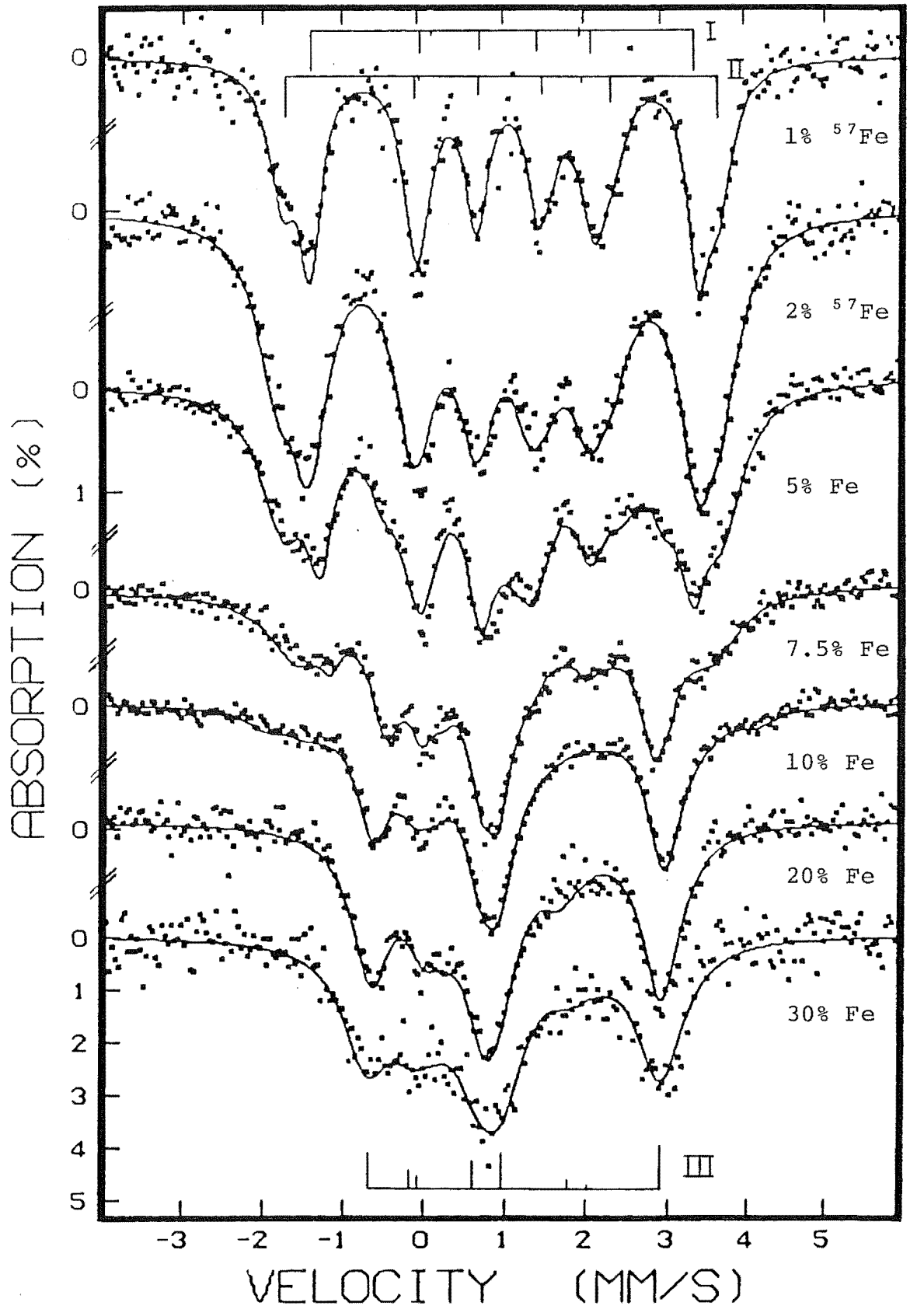

Figure 4.22 Iron concentration dependence of the Mössbauer spectra of $MnSe_2$ at 20K.

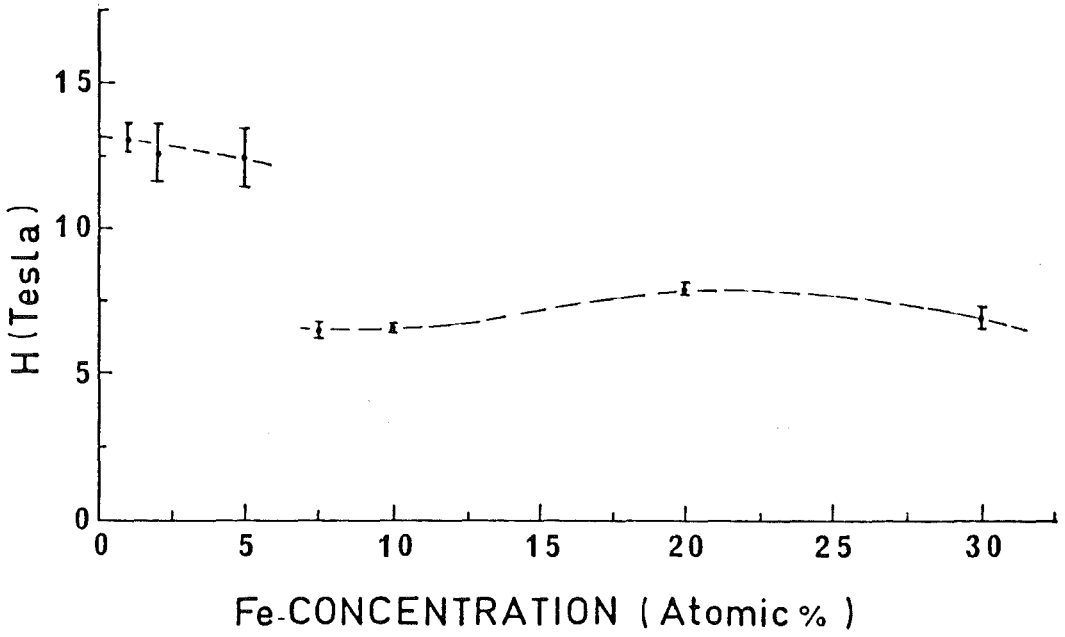

Figure 4.23 Iron concentration dependence of the hyperfine field in $MnSe_2$ at 20K.

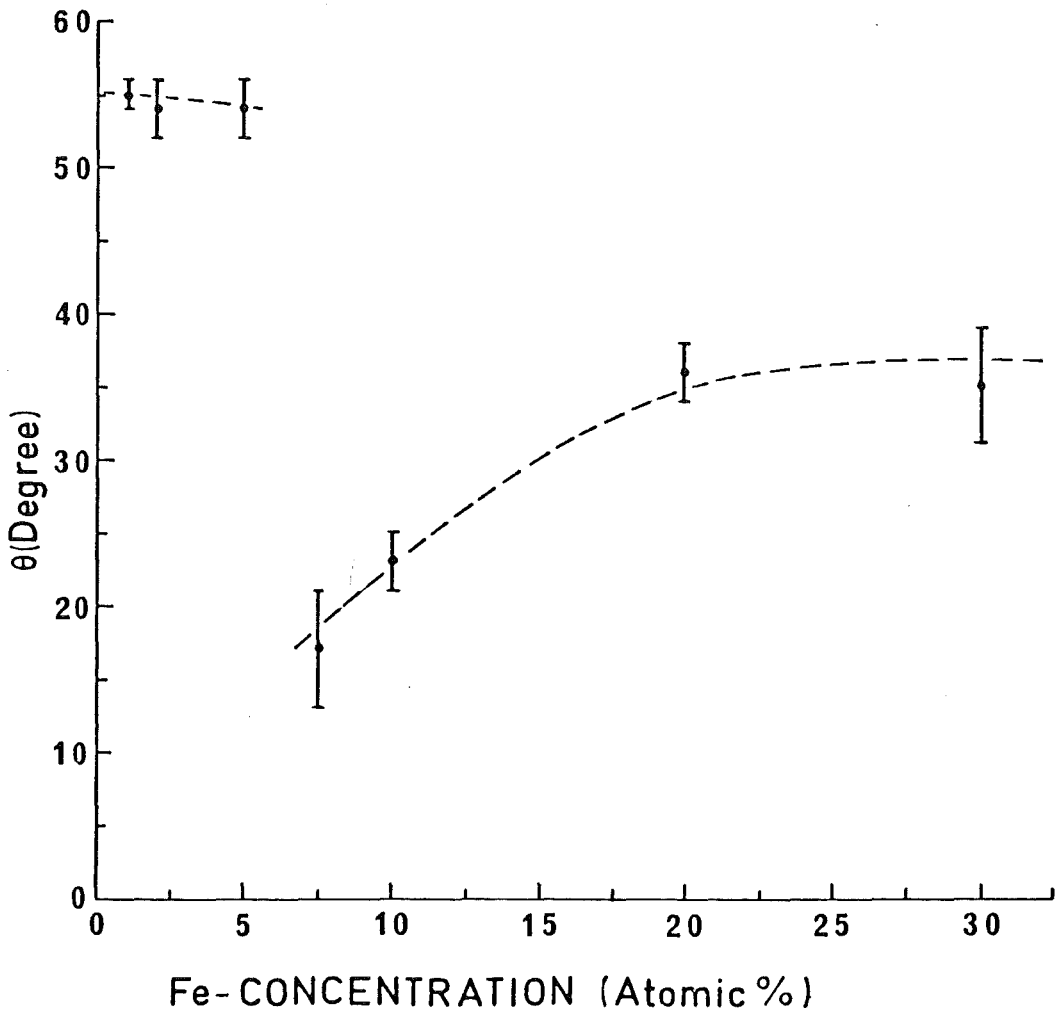

Figure 4.24 Iron concentration dependence of the hyperfine angle in $MnSe_2$ at 20K.

Table 4.10 Fe-concentration dependence of the Mössbauer parameters in $MnSe_2$ at 20K.

Fe-conc. (atomic %)	Magnetic site	H (tesla)	QS (mm s^{-1})	IS (mm s^{-1})	η	ϕ (degree)	θ (degree)	Γ (mm s^{-1})	Fractional absorption
1	I	13.1(5)	1.6(2)	0.97(2)	0.1(1)	90	55(1)	0.35(6)	0.053(3)
	II	15(1)	1.8(1)	0.99(2)	0.2(1)	90	58(2)	0.45(8)	0.033(3)
2	I	12.6(1.0)	1.81(5)	0.96(2)	0.1(1)	90	54(2)	0.62(6)	0.07(2)
	II	15.6(1.5)	1.7(2)	0.97(3)	0.2(1)	90	58(3)	0.60(8)	0.04(2)
5	I	12.4(1.0)	1.7(2)	0.97(3)	0(2)	90	54(2)	0.43(8)	0.056(8)
	II	14.9(5)	1.9(1)	1.00(2)	0.12(8)	90	60(2)	0.73(8)	0.053(6)
	III	6.4(1.0)	2.0(8)	1.02(5)	0.3(9)	90	20(50)	0.5(1)	0.027(4)
7.5	I	12(1)	1.3(4)	0.90(4)	0	0	58(4)	0.3(2)	0.017(4)
	II	13.5(6)	1.9(2)	0.93(4)	0	0	56(3)	0.9(1)	0.035(4)
	III	6.5(2)	1.88(4)	0.94(2)	0	0	17(4)	0.45(4)	0.066(4)
10	I	12.5(1.5)	1.4(6)	0.91(6)	0	0	53(6)	0.8(4)	0.019(8)
	II	13.5(2.5)	2.6(4)	1.17(8)	0	0	65(7)	0.60(4)	0.015(6)
	III	6.6(1)	1.86(3)	0.95(2)	0	0	23(2)	0.50(4)	0.139(6)
20	III	7.9(2)	1.49(4)	0.95(2)	0.30(8)	0	36(2)	0.57(4)	0.21(1)
30	III	6.9(4)	1.8(1)	0.93(2)	0.5(2)	0	35(4)	0.69(8)	0.11(1)

field theory presented in section 2.3. Using this formalism, a computer program has been written (Appendix C). Using this program we found the optimum set of values of H_c, $\langle r^{-3} \rangle$, $\Delta, \lambda, J'\langle S_i \rangle, \theta_{ex}$ and T_B for the compounds studied, such that the calculated H and θ fit the Mössbauer experimental data at all temperatures. Using the Brillouin function with $S = \frac{5}{2}$, and varying H_c, $\langle r^{-3} \rangle, \Delta, \lambda, J'\langle S_i \rangle$, θ_{ex} and T_B, we calculated several sets of values of the temperature dependence of H and θ for each of the samples selected for crystal-field analysis, these are plotted and after a visual comparison of the graphs of the temperature dependence of H and θ, we determined the best set of parameters. Uncertainties in these parameters are estimated by varying them and finding the effect on the values of H and θ. We observed that calculated values of H and θ are more sensitive to changes in H_c, $\langle r^{-3} \rangle$ and $J'\langle S_i \rangle$ than to changes in Δ and λ.

4.2.1 MnS_2 Sample

In Fig. 4.25 the temperature dependence of the magnetic hyperfine field is plotted. H is almost constant up to 40K and then decreases slightly with increasing temperature and drops sharply to zero at T_N (49K). This behaviour is expected for a first-order antiferromagnetic phase transition in MnS_2 as observed by Hastings et al.[8] and Westrum et al.[7]. Hastings et al. also calculated the extrapolated transition temperature (T_B) from the Brillouin function with $S = \frac{5}{2}$ as 65K. In this calculation we wished to see whether our data

is consistent with the neutron diffraction data[1] which determined that the spin direction was along [100] and makes an angle of 54.74° ($\cos^{-1}(1/\sqrt{3})$ with all four $\bar{3}$ axes i.e. <111>. Accordingly we tried to fit the hyperfine field (H) and angle (θ) with θ_{ex} fixed at 55°. This procedure was successful and the following set of parameters was determined.

$H_c = -50 \pm 1$ T

$\langle r^{-3} \rangle = 4.0 \pm 0.1$ a.u.

$3\Delta = -250 \pm 10$ cm^{-1}

$\lambda = -93 \pm 3$ cm^{-1}

$J'\langle S_i \rangle = -100 \pm 3$ cm^{-1}

$T_B = 63 \pm 2$K

The calculated curves, drawn as solid lines in Figs. 4.25 and 4.26, are in good agreement with the experimental data. The vertical dashed bars in Figs. 4.26 represent the range of θ determined from the ambiguous solutions and our calculated curve passed through the lower end of the bars which represents the lower asymmetry parameters and are consistent with our observed data. The adjustable parameters H_c, $\langle r^{-3} \rangle$ and λ are in reasonable agreement with the previously reported values. (In $MnCO_3$[27], $H_c = -49.5$ T, $\langle r^{-3} \rangle = 3.91$ a.u. and $\lambda = -88.6$ cm^{-1}; in CoO(I)[26], $H_c = -48.8$ T and $\langle r^{-3} \rangle = 4.4$ a.u and in NiO[47];

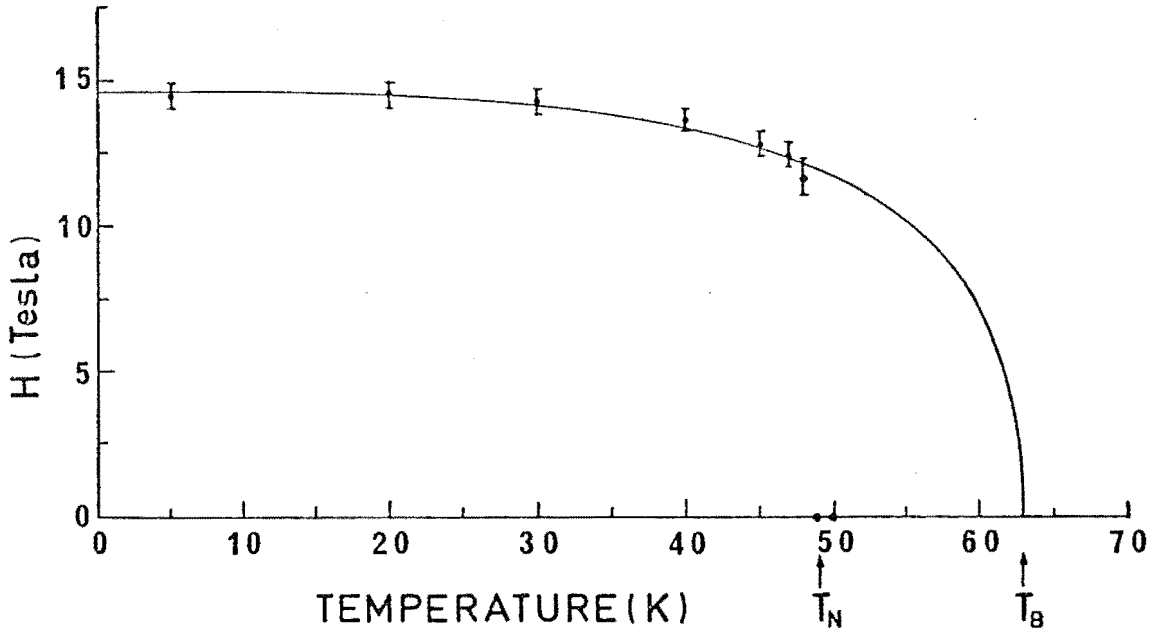

Figure 4.25 Temperature dependence of the hyperfine field at ^{57}Fe nuclei in MnS_2. The solid curve is calculated from crystal-field theory.

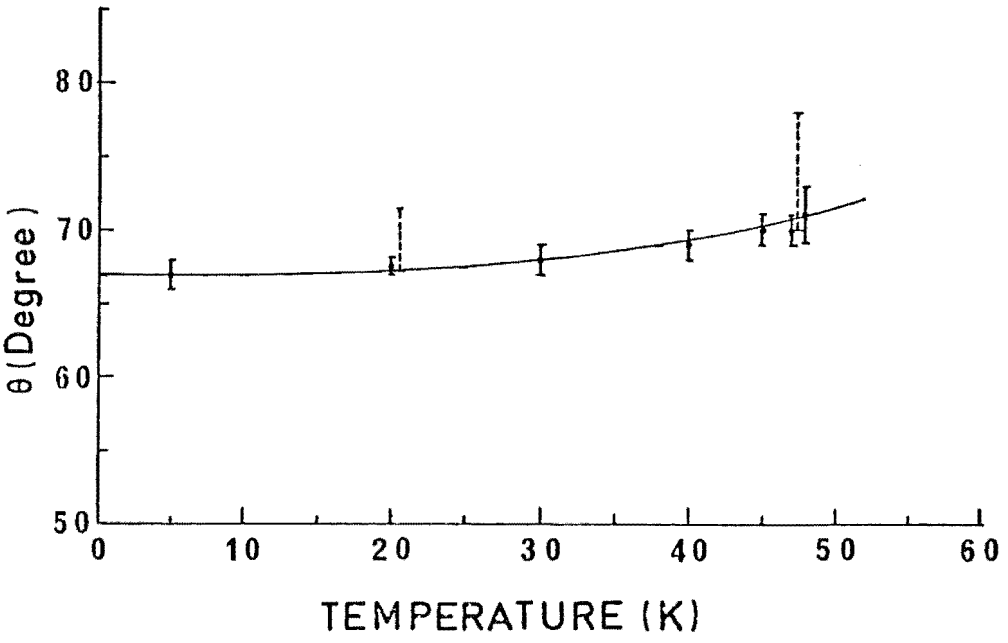

Figure 4.26 Temperature dependence of the hyperfine angle in MnS_2. Calculated curve is the solid line. Broken error bars indicate the range of θ values within the ambiguous solutions at 20K and 47K. θ_{ex} was taken as 55° at all temperatures.

H_c = -45.8 T, $\langle r^{-3} \rangle$ = 4.4 a.u). The calculated free-ion values are H_c = -55 T, $\langle r^{-3} \rangle$ = 4.55 a.u and λ = -103 cm^{-1}, so we observed a reduction of 10%, 14% and 11.4% respectively, which are in the acceptable ranges. Thus the spin-orbit coupling parameter λ is reduced by a covalency factor of $\alpha^2 \simeq 0.9$ from its free-ion value, which falls within the observed range of 0.6 - 0.9 for various ferrous compounds[28].

4.2.2 $MnSe_2$ 2% ^{57}Fe Sample

As mentioned in section 4.1.2.2, below T_N the Mössbauer spectra observed for this sample were a superposition of two hyperfine structures due to two Fe^{2+} sites. The temperature dependence of H and θ for each of these two sites is plotted in Figs. 4.27 to 4.30. The nature of the temperature dependence of H of these sites is the same; H is almost constant up to 40K with increasing temperatures, decreases slowly up to 50.5K and then suddenly drops to zero at T_N. This behaviour definitely supports the first-order magnetic transition as predicted by Corliss et al.[11] and observed by Itoh and Miyahara[10].

As for MnS_2 the spin direction had previously been determined as along [100] at 4.2K[1], so we again tried to fit our data for H and θ with θ_{ex} = 55° but this was not possible over the whole temperature range. However we found that if θ_{ex} was chosen to be 55° for our lowest temperature (5K) and then it was allowed to increase with temperature, a consistent set of parameters could be found. Under these

conditions the best set of parameters is:

$H_c = -51 \pm 1$ T

$\langle r^{-3} \rangle = 4.4 \pm 0.1$ a.u

$3\Delta = -207 \pm 40$ cm^{-1}

$\lambda = -88 \pm 5$ cm^{-1}

$T_B = 66 \pm 3K$

The plots of the temperature dependence of H and θ for both sites is shown in Figs. 4.27 through 4.30. In these figures, the calculated curves are drawn as solid lines, the broken curves in Figs. 4.28 and 4.30 represent the temperature dependence of θ_{ex} and the dashed vertical bars represent the range of θ determined from the ambiguous solutions at 20K and 40K. As can be seen the ambiguity range is comparable with the error range.

In this fitting all the parameters except $J'\langle S_i \rangle$ are kept the same for each site. We calculated the best values of $J'\langle S_i \rangle$ for site I and site II as -75(3) cm^{-1} and -100(3) cm^{-1} respectively and from these values the exchange constants J_1 and J_2 can be determined (Appendix D). The observed hyperfine angles (θ) at the lowest temperature (5K) are the same at each site within experimental accuracy. The calculated curve for θ for site II is outside the experimental error. Considerable effort has been spent to improve this fitting, but we could not obtain any closer

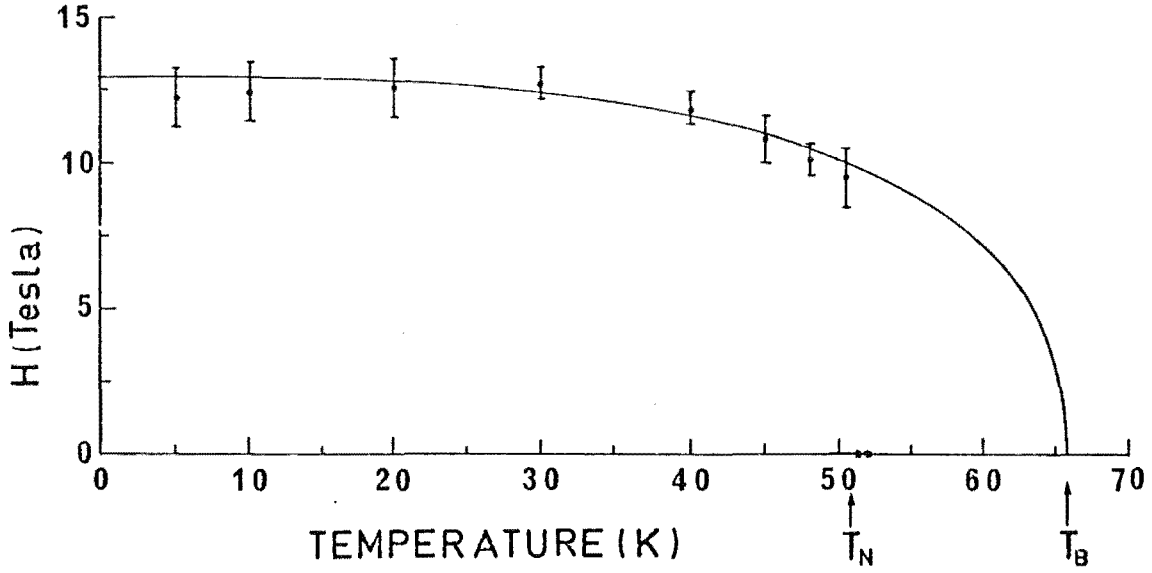

Figure 4.27 Temperature dependence of the hyperfine field at ^{57}Fe nuclei in $MnSe_2$ 2% ^{57}Fe (site I). The solid curve is calculated from crystal-field theory.

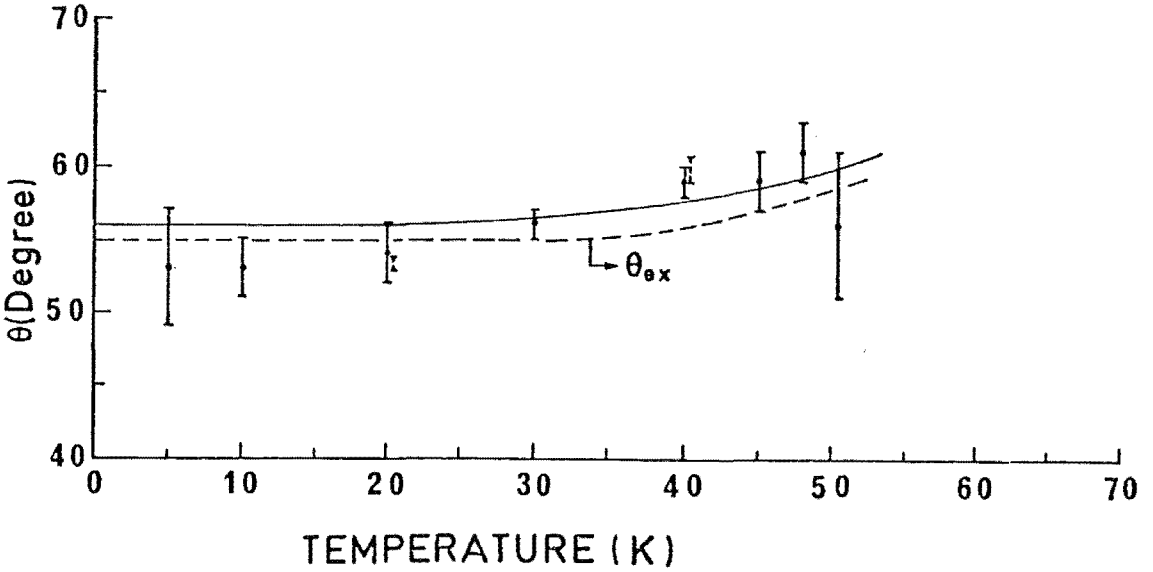

Figure 4.28 Temperature dependence of the hyperfine angle in $MnSe_2$ 2% ^{57}Fe (site I). Calculated curve is the solid line. Broken error bars indicate the range of θ values within the ambiguous solutions at 20K and 40K. Broken curve represents the exchange angle.

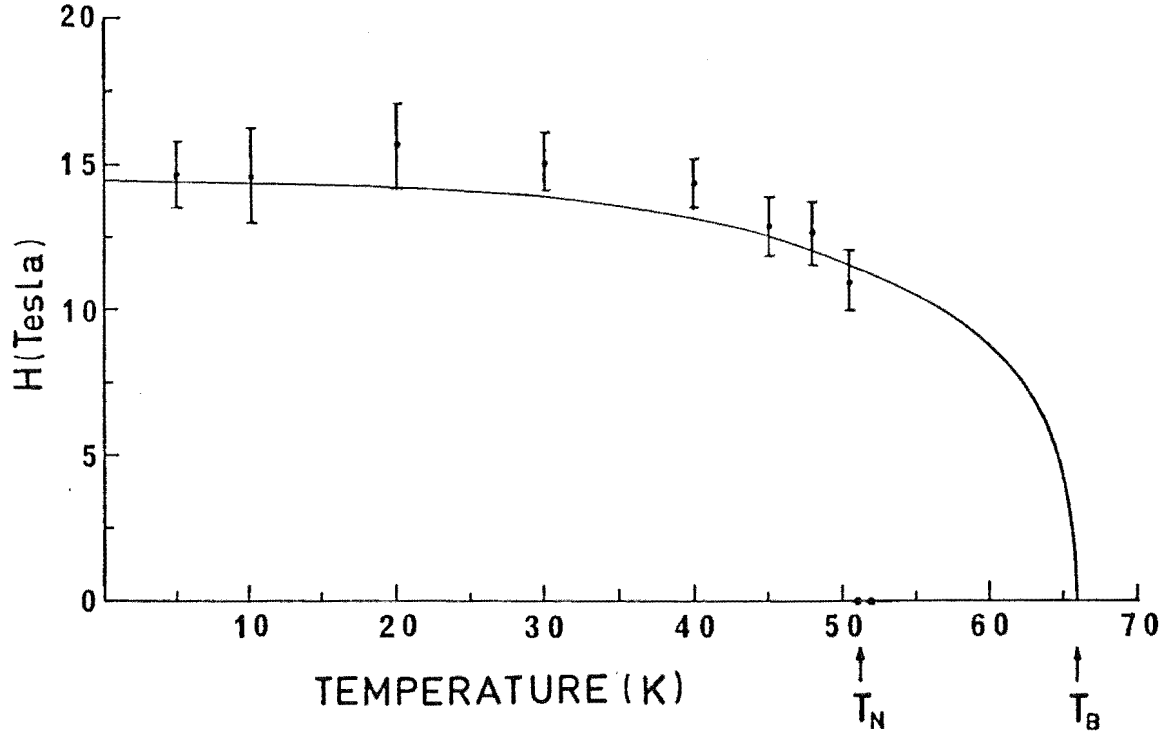

Figure 4.29 Temperature dependence of the hyperfine field at ^{57}Fe nuclei in $MnSe_2$ 2% ^{57}Fe (site II). The solid curve is calculated from crystal-field theory.

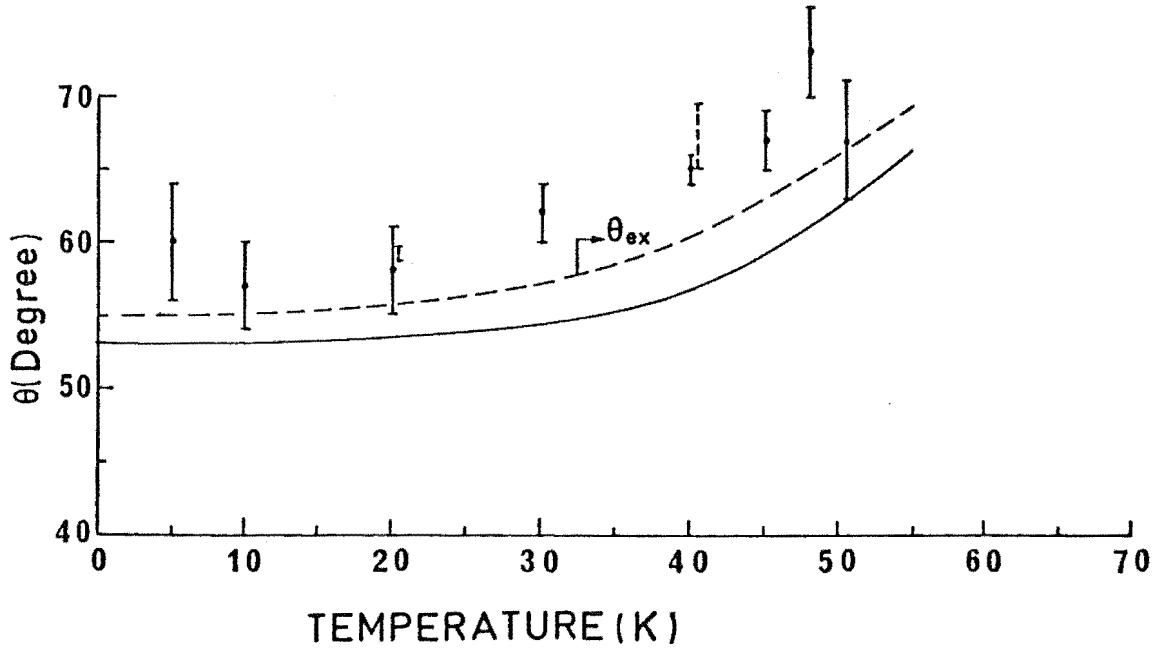

Figure 4.30 Temperature dependence of the hyperfine angle in $MnSe_2$ 2% ^{57}Fe (site II). Calculated curve is the solid line. Broken error bars indicate the range of θ values within the ambiguous solutions at 20K and 40K. Broken curve represents the exchange angle.

agreement with the experimental points. The value of θ_{ex} at 5K is consistent with the spin directions being along [100] as deduced by Hastings et al.[1].

Except for the $\theta(T)$ values for site II, the calculated curves are in reasonably good agreement with the experimental results. The calculated values of H_c, $\langle r^{-3} \rangle$ and λ showed a reduction of 7.8%, 3.4% and 17.7% respectively from their free-ion values, the spin-orbit coupling parameter λ being thus reduced by a covalency factor of $\alpha^2 \simeq 0.85$. T_B for this sample is determined as 66K which is 15K above the the transition temperature T_N.

4.2.3 $MnSe_2$ 20% Sample

The temperature dependences of H and θ in this sample are plotted in Figs. 4.31 and 4.32 respectively. The temperature dependent behaviour of the hyperfine field is completely different from that of the $MnSe_2$ 2% ^{57}Fe sample; the magnitude of H decreases with increasing temperature and becomes zero at T_N. The transition appears to be second order.

The spectrum at 80K near T_N (85K) was fitted with η set to zero only. If η was allowed to vary freely the fitting program would not converge - probably because of the lack of structure in the spectrum at this temperature. The crystal-field analysis was therefore carried out using the values of H and θ obtained with $\eta = 0$ at all the temperatures used, to maintain consistency of the data, and

also to include more data points near T_N.

The crystal-field parameters for this sample were determined in the same way as in the previous samples and the best parameters are the following,

$H_c = -42 \pm 1$ T

$\langle r^{-3} \rangle = 3.8 \pm 0.2$ a.u

$3\Delta = -250 \pm 20$ cm^{-1}

$\lambda = -85 \pm 5$ cm^{-1}

$J'\langle S_i \rangle = -25 \pm 3$ cm^{-1}

$\theta_{ex} = 36 \pm 4°$ (at 20K)

$T_B = 85 \pm 5$ (same as T_N).

The calculated curves are drawn as solid lines and the temperature dependence of θ_{ex} is also shown in Fig. 4.32 as a dashed line. The temperature variation, and the values, of θ and θ_{ex} are almost the same and the value of θ_{ex} ranges from ~ 34° to 49° below T_N, which does not represent any unique axis; so a multiaxes spin system is probably present in this crystal.

The calculated curves are in reasonably good agreement with our data and the values of H_c, $\langle r^{-3} \rangle$ and λ showed a reduction of 23.6%, 16.5% and 17.5% respectively from their free-ion values. λ is reduced by a covalency factor of $\alpha^2 \simeq 0.83$. Thus our parameters are within acceptable ranges.

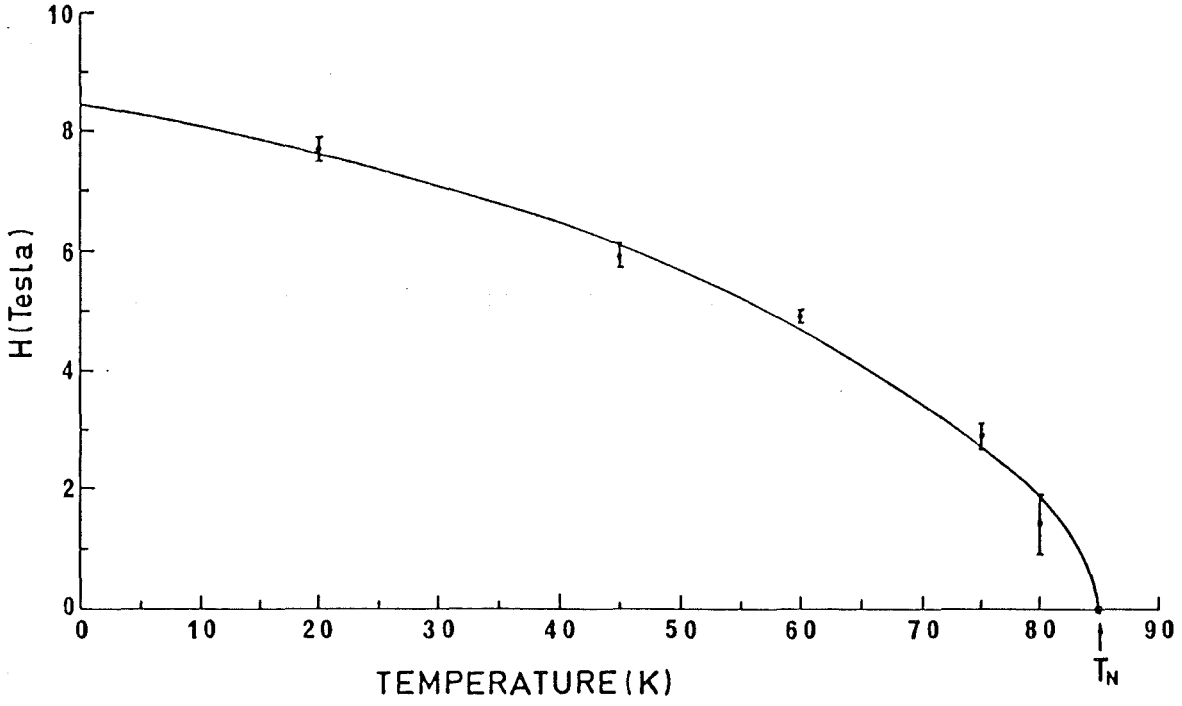

Figure 4.31 Temperature dependence of the hyperfine field at ^{57}Fe nuclei in $MnSe_2$ 20% Fe. The solid curve is calculated from crystal-field theory.

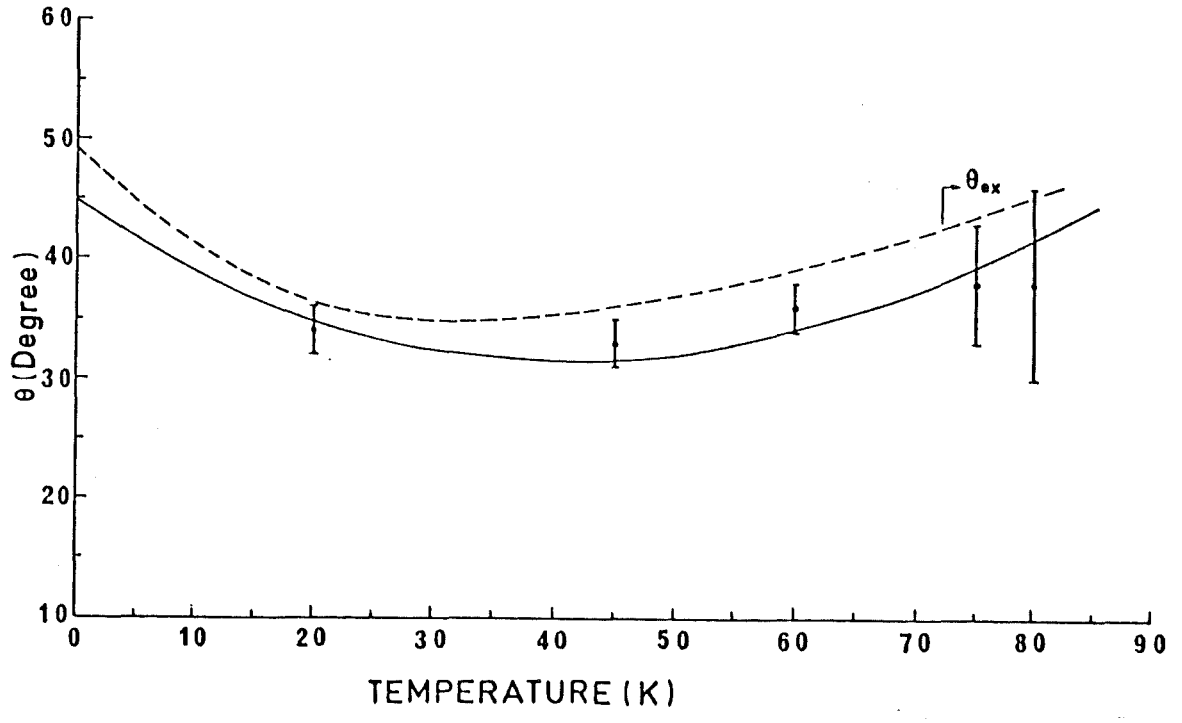

Figure 4.32 Temperature dependence of the hyperfine angle in $MnSe_2$ 20% Fe. Calculated curve is the solid line. Broken curve represents the exchange angle.

4.2.4 $MnTe_2$ 2% ^{57}Fe Sample

In this sample it can be seen that the variation of hyperfine field with respect to temperature is different from H in MnS_2 and in low Fe-content $MnSe_2$. H is almost constant up to 15K, decreases slowly up to 88K and then drops to zero at 91K (T_N) (Fig 4.33). We suspect that the transition is also first-order in $MnTe_2$. The temperature dependence of the hyperfine angle (θ) is plotted in Fig. 4.34. θ is 0° at 8K and increases slowly to 17° at 90.5K. The temperature dependence of the hyperfine field and the hyperfine angle data were fitted by a non-linear least-squares fitting program[41], assuming θ_{ex} increases linearly with temperatures between 0° at 8K and 30° at 85K. The calculated curves in the figures are in reasonably good agreement with the values determined from the Mössbauer spectra. The broken curve in Fig. 4.34 represents the temperature dependence of θ_{ex}.

We observed the following as a best set of parameters

$H_c = -45 \pm 1$ T

$\langle r^{-3} \rangle = 4.34 \pm 0.2$ a.u

$3\Delta = -276 \pm 30$ cm^{-1}

$\lambda = -95 \pm 5$ cm^{-1}

$J'\langle S_i \rangle = -20 \pm 1$ cm^{-1}

$\theta_{ex} = 0 \pm 3°$ at 8K

$T_B = 105 \pm 5$K

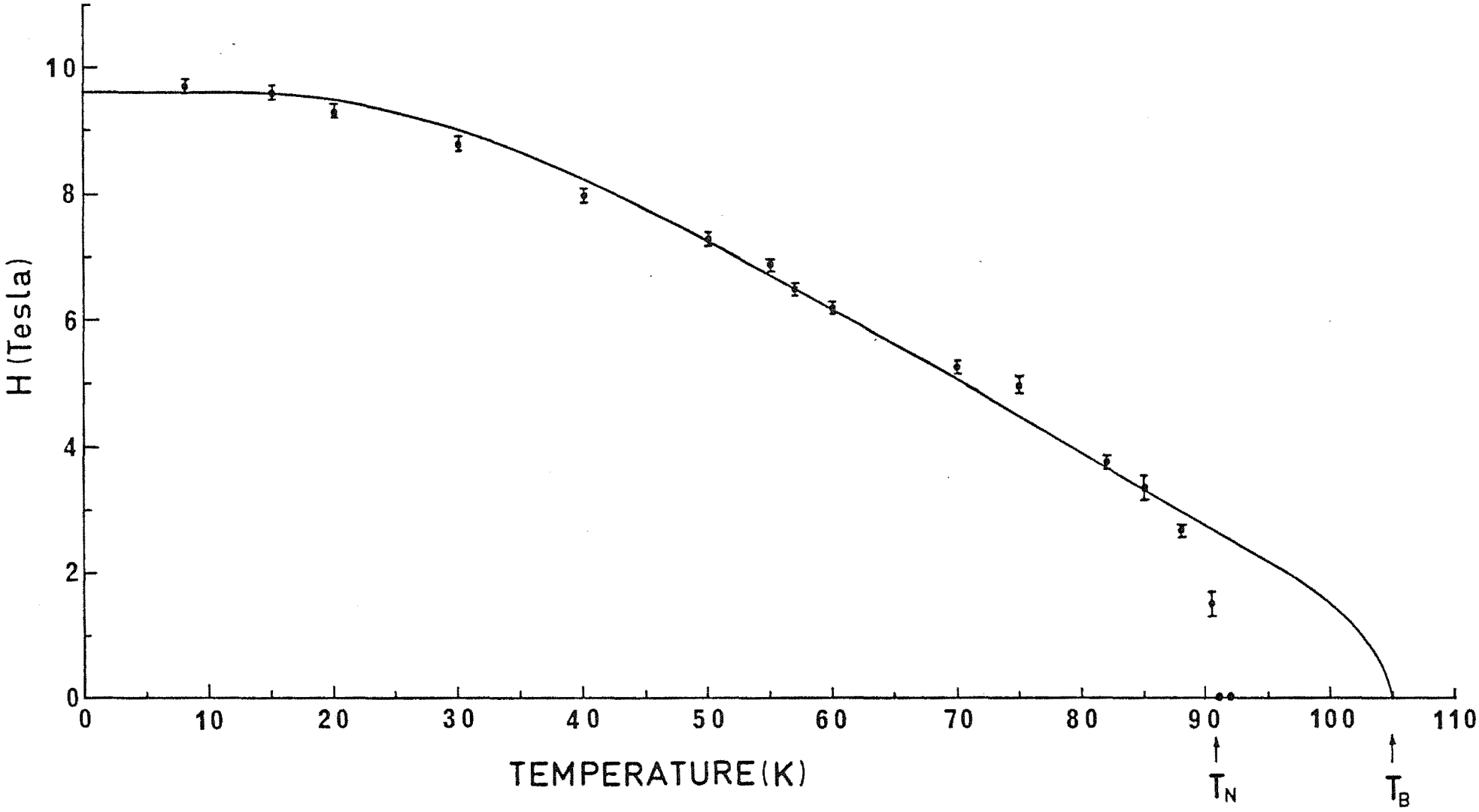

Figure 4.33 Temperature dependence of the hyperfine field at ^{57}Fe nuclei in $MnTe_2$. The solid curve is determined from crystal-field theory using a fitting program.

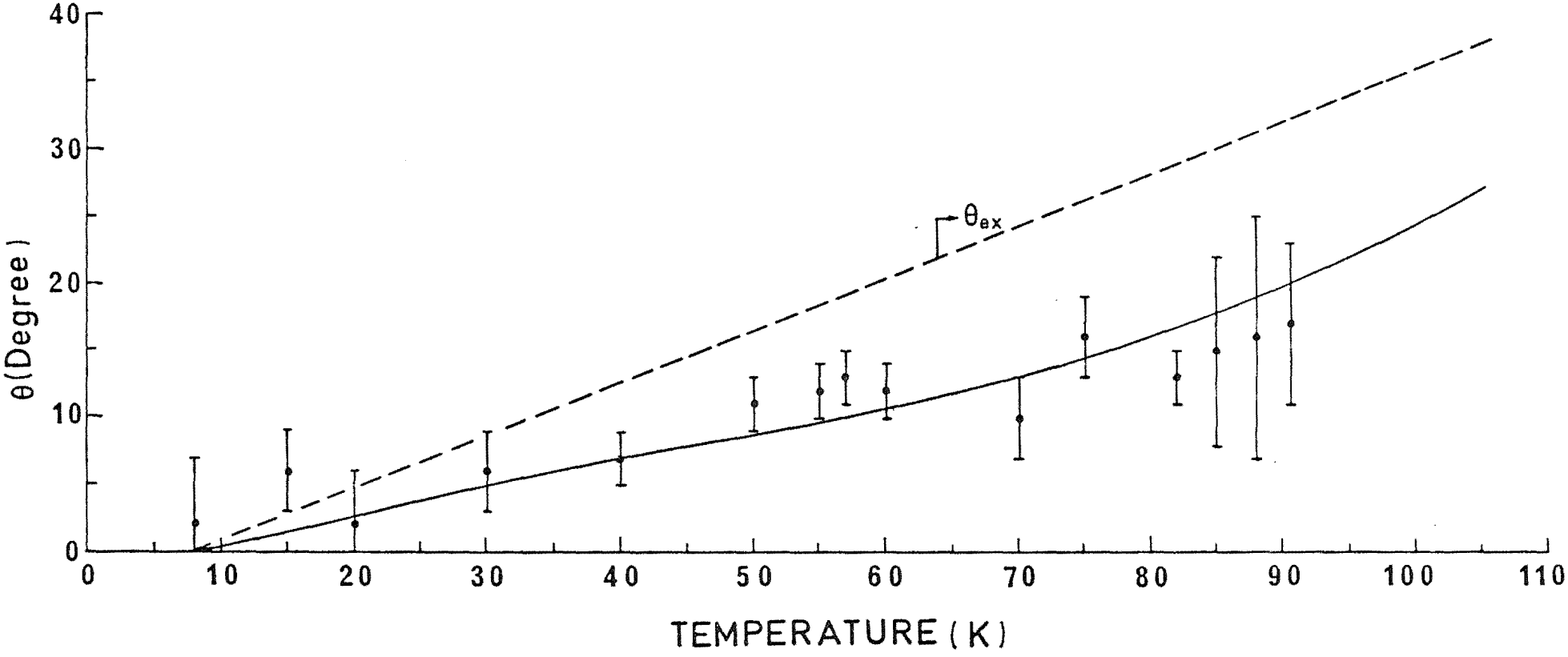

Figure 4.34 Temperature dependence of the hyperfine angle in $MnTe_2$. Calculated curve is the solid line. Broken curve represents the exchange angle which was assumed to increase linearly with temperatures.

In this substance, changing Δ and λ has a very small effect on the quality of the fit; the fit quality was much more sensitive to the values of H_c and $\langle r^{-3} \rangle$, and especially to the value of $J'\langle S_i \rangle$. The adjusted values of H_c, $\langle r^{-3} \rangle$ and λ showed a reduction of 18%, 4.6% and 7.8% respectively from their free-ion values and λ is reduced by a covalency-factor of 0.92. So these parameters are in fairly good agreement with the previous workers (see section 4.2.1).

Pasternak and Spijkervet[2] studied the ^{125}Te Mössbauer effect in $MnTe_2$ and measured the hyperfine angle θ between H and the z principal axis of the EFG as 30° at 4.2K and 0° at 77.3K. Hastings et al.[3] later proposed a multiaxis spin system with the spins pointing equally along the local <111> direction on the basis of this high-temperature data of θ. In our present investigation, we deduced the value of θ_{ex} at 8K and 77K to be 0° and ~ 27° respectively with the crystal z-axis along [111]. If we assume this axis coincides with the EFG z principal axis, then our result at 77K is definitely inconsistent with the model of Hastings et al.[3]. However, the low temperature data could be consistent, provided that principal EFG axis is not along the crystal z-axis along [111], which will give non-zero θ_{ex} and thus non-zero θ.

It is also possible that doping ^{57}Fe into $MnTe_2$ could change the magnetic structure, so that the spin direction of Mn^{2+} is different to its direction in the undoped material. Thus further work is necessary to resolve this inconsistency by studying samples containing different lower concentrations of iron.

4.3 DISCUSSION

The relations between the exchange field parameter $J'\langle S_i \rangle$ and the exchange constants J_1 and J_2 for MnS_2, $MnSe_2$ 2% ^{57}Fe and $MnTe_2$ are explained in Appendix D, where it is shown that $J'\langle S_i \rangle(MnS_2) = 4\sqrt{35}\ (J_1 - \frac{1}{2} J_2)$, $J'\langle S_i \rangle(MnSe_2$ site I$) = 4\sqrt{35}\ (J_1 - J_2)$, $J'\langle S_i \rangle(MnSe_2$ site II$) = 4\sqrt{35}\ (J_1 - \frac{1}{2} J_2)$ and $J'\langle S_i \rangle(MnTe_2) = 4\sqrt{35}\ (J_1 - 1.5\ J_2)$. Thus it can be seen, if we assume J_1 and J_2 are about the same in all 3 compounds, that $J'\langle S_i \rangle$ for MnS_2 should be approximately equal to the corresponding site II parameter of $MnSe_2$ 2% ^{57}Fe. We in fact observed that the two were equal ($-100\ cm^{-1}$). The expected magnitude of $J'\langle S_i \rangle$ for site I of $MnSe_2$ 2% ^{57}Fe should be less than the value of site II and our observed value is $-75\ cm^{-1}$. In $MnTe_2$, the magnitude of $J'\langle S_i \rangle$ is expected to be less than the above site I parameter and our observed value is $-20\ cm^{-1}$. For $MnSe_2$ 2% ^{57}Fe, solving two simultaneous equations, we calculate J_1 and J_2 as $-7.6 \pm 0.7K$ and $-3.0 \pm 0.7K$ respectively.

The observed $J'\langle S_i \rangle$ for $MnSe_2$ 20% Fe is $-25\ cm^{-1}$; its magnitude is much smaller than $J'\langle S_i \rangle$ for the two sites in 2% $MnSe_2$ ($-75\ cm^{-1}$, $-100\ cm^{-1}$). The spin system of this high Fe-concentration sample is unknown, but the observed value of $J'\langle S_i \rangle$, the high value of T_N (85K) and the general nature of H and θ variation with temperatures are quite similar to the corresponding values for $MnTe_2$, so it is possible that $MnSe_2$ 20% Fe has the same spin arrangement as $MnTe_2$.

It is possible that $J'\langle S_i \rangle$ should include the effects of third nearest neighbour interactions, which we have neglected.

CHAPTER 5

SUMMARY AND SUGGESTIONS FOR FURTHER WORK

5.1 SUMMARY

We have analysed hyperfine Mössbauer spectra of MnS_2, $MnSe_2$ and $MnTe_2$ by diagonalizing the 4 x 4 magnetic and quadrupole Hamiltonian matrix and fitting the spectra by a least-squares procedure. The temperature dependence of the isomer shift data has been explained successfully using the Debye model and the Debye temperatures determined.

The temperature dependence of the magnetic hyperfine field and of its direction relative to the EFG z axis for the ^{57}Fe nucleus in ferrous ions in various samples were measured. We calculated values of the Mössbauer parameters by assuming the expectation value of the Mn^{2+} spin followed a Brillouin function as the temperature increased. The temperature dependences of the hyperfine field (H) and the hyperfine angle (θ) data were calculated by taking account of spin-orbit coupling, a Heisenberg exchange interaction and the trigonal crystalline field parameter. The calculated and experimental results agreed in general very closely, and the crystal-field parameters are in reasonable agreement with those reported by previous workers for similar ferrous compounds. The results of these data are summarized in Table 5.1.

From these fittings, the exchange angles at lowest temperatures were obtained and conclusions drawn regarding

Table 5.1 Summary of the values of T_N and of parameters obtained from the crystal-field calculations.

Parameters	Free-ion value	MnS_2	$MnSe_2$ 2% ^{57}Fe		$MnSe_2$ 20% Fe	$MnTe_2$
			Site I ($\frac{2}{3}$)	Site II ($\frac{1}{3}$)		
H_c(T)	-55	-50(1)	-51(1)		-42(1)	-45(1)
$\langle r^{-3} \rangle$(a.u)	4.55	4.0(1)	4.4(1)		3.8(2)	4.34(20)
3Δ (cm^{-1})		-250(10)	-207(40)	same	-250(20)	-276(30)
λ(cm^{-1})	-103	-93(3)	-88(5)		-85(5)	-95(5)
$J'\langle S_i \rangle$(cm^{-1})		-100(3)	-75(3)	-100(3)	-25(3)	-20(1)
θ_{ex} (deg.)		55(5)	55(5)		36(4)	0(3)
T_N(K)		49.0(5)	51.0(5)	same	85(1)	91.0(5)
T_B(K)		63(2)	66(3)		85(5)	105(5)

the spin direction of the compounds studied. In low Fe-content MnS_2 and in $MnSe_2$ our results are consistent with the spin direction deduced by neutron diffraction data. In $MnTe_2$, the spin arrangement observed from ^{125}Te and ^{57}Fe Mössbauer data apparently disagree at high temperature; more work is required to discover the cause of the disagreement. From the calculated exchange parameter data of low Fe-content $MnSe_2$, the nearest (J_1) and the next nearest (J_2) neighbour exchange constants are determined.

Iron concentration dependence of the hyperfine parameters in $MnSe_2$ at 20K were measured and the Néel temperatures of these samples were determined. A change in the spin arrangement in Fe-doped $MnSe_2$ was detected at Fe concentrations > 2 at. %.

5.2 SUGGESTIONS FOR FURTHER WORK

It is possible to calculate eQ and η from our crystal field parameters; it would be interesting to perform this calculation in order to understand the complete picture of the exchange interactions.

The spin arrangement in the high Fe-content $MnSe_2$, and the reason for the variation of hyperfine fields with Fe-concentrations are not clear, so further work is clearly desirable to explore these mechanisms.

APPENDIX A

HAMILTONIAN HYPERFINE MATRIX FOR ^{57}Fe AND TRANSITION PROBABILITIES

The matrix of the Hamiltonian described in eqn. (2.2) for the first excited state of ^{57}Fe nucleus in the $|\frac{3}{2}\ m_I>$ basis is

m_I' \ m_I	$\frac{3}{2}$	$\frac{1}{2}$	$-\frac{1}{2}$	$-\frac{3}{2}$
$\frac{3}{2}$	a_{11}	a_{12}	a_{13}	0
$\frac{1}{2}$	a_{21}	a_{22}	a_{23}	a_{13}
$-\frac{1}{2}$	a_{13}	a_{32}	a_{33}	a_{12}
$-\frac{3}{2}$	0	a_{13}	a_{21}	a_{44}

where

$$a_{11} = 3A - \tfrac{3}{2}\alpha \cos\theta$$

$$a_{22} = -3A - \tfrac{1}{2}\alpha \cos\theta$$

$$a_{33} = -3A + \tfrac{1}{2}\alpha \cos\theta$$

$$a_{44} = 3A + \tfrac{3}{2}\alpha \cos\theta$$

$$a_{12} = -\frac{\sqrt{3}}{2}\alpha \sin\theta(\cos\phi - i \sin\phi)$$

$$a_{21} = -\frac{\sqrt{3}}{2}\alpha \sin\theta(\cos\phi + i \sin\phi)$$

$$a_{23} = -\alpha \sin\theta\ (\cos\phi - i \sin\phi)$$

$$a_{32} = -\alpha \sin\theta \,(\cos\phi + i \sin\phi)$$

$$a_{13} = \sqrt{3}\ A\eta$$

with

$$A = \frac{e^2qQ}{4I(2I-1)} = \frac{e^2qQ}{12}$$

and

$$\alpha = g_{\frac{3}{2}}\ \mu_N H$$

By diagonalizing the 4 x 4 matrix, it is possible to obtain the energy eigenvalues E_i (i = 1,2,3,4) of the first excited state of ^{57}Fe and the corresponding eigenvectors

$$|\phi_i\rangle = C^{\frac{3}{2}}_{(\frac{3}{2},i)}\left|\tfrac{3}{2}\ \tfrac{3}{2}\right\rangle + C^{\frac{1}{2}}_{(\frac{3}{2},i)}\left|\tfrac{3}{2}\ \tfrac{1}{2}\right\rangle + C^{-\frac{1}{2}}_{(\frac{3}{2},i)}\left|\tfrac{3}{2}\ -\tfrac{1}{2}\right\rangle$$

$$+ C^{-\frac{3}{2}}_{(\frac{3}{2},i)}\left|\tfrac{3}{2}\ -\tfrac{3}{2}\right\rangle$$

On the other hand the ground state of the ^{57}Fe nucleus has no quadrupole moment, so the Hamiltonian matrix in the $|\frac{1}{2}\ m_I\rangle$ basis is

m_I / m_I'	$\frac{1}{2}$	$-\frac{1}{2}$
$\frac{1}{2}$	b_{11}	b_{12}
$-\frac{1}{2}$	b_{21}	b_{22}

where

$$b_{11} = -\tfrac{1}{2}\ \beta \cos\theta$$

$$b_{22} = \tfrac{1}{2}\ \beta \cos\theta$$

$$b_{12} = -\tfrac{1}{2}\beta \sin\theta\,(\cos\phi - i\sin\phi)$$

$$b_{21} = -\tfrac{1}{2}\beta \sin\theta\,(\cos\phi + i\sin\phi)$$

with

$$\beta = g_{\frac{1}{2}}\,\mu_N H$$

and the eigenstates are linear combination of $|\tfrac{1}{2}\ \pm\tfrac{1}{2}>$ with eigenvalues E_j $(j = 1,2)$, so that

$$|\phi_j> = C^{\frac{1}{2}}_{(\frac{1}{2},j)}|\tfrac{1}{2}\ \tfrac{1}{2}> + C^{-\frac{1}{2}}_{(\frac{1}{2},j)}|\tfrac{1}{2}\ -\tfrac{1}{2}>$$

In terms of the state eigenvector coefficients the transition probability for a polycrystalline sample is (25)

$$P'(\tfrac{3}{2},i;\tfrac{1}{2},j) = \frac{4\pi}{3}\{|C^{\frac{1}{2}*}_{(\frac{1}{2},j)}\,C^{\frac{3}{2}}_{(\frac{3}{2},i)} + 3^{-\frac{1}{2}}C^{\frac{1}{2}*}_{(\frac{1}{2},j)}\,C^{-\frac{1}{2}}_{(\frac{3}{2},i)}$$

$$+ C^{-\frac{1}{2}*}_{(\frac{1}{2},j)}\,C^{-\frac{3}{2}}_{(\frac{3}{2},i)} + 3^{-\frac{1}{2}}\,C^{-\frac{1}{2}*}_{(\frac{1}{2},j)}\,C^{\frac{1}{2}}_{(\frac{3}{2},i)}|^2$$

$$+ |C^{\frac{1}{2}*}_{(\frac{1}{2},j)}\,C^{\frac{3}{2}}_{(\frac{3}{2},i)} - 3^{-\frac{1}{2}}\,C^{\frac{1}{2}*}_{(\frac{1}{2},j)}\,C^{-\frac{1}{2}}_{(\frac{3}{2},i)}$$

$$- C^{-\frac{1}{2}*}_{(\frac{1}{2},j)}\,C^{-\frac{3}{2}}_{(\frac{3}{2},i)} + 3^{-\frac{1}{2}}C^{-\frac{1}{2}*}_{(\frac{1}{2},j)}\,C^{\frac{1}{2}}_{(\frac{3}{2},i)}|^2$$

$$+ \tfrac{4}{3}|C^{\frac{1}{2}*}_{(\frac{1}{2},j)}C^{\frac{1}{2}}_{(\frac{3}{2},i)} + C^{-\frac{1}{2}*}_{(\frac{1}{2},j)}C^{-\frac{1}{2}}_{(\frac{3}{2},i)}|^2\}.$$

The magnetic field can be chosen to be in the xz plane, such that $\phi = 0$. In our fitting program, the above matrices were combined into a 6 x 6 matrix and relabelled as

$\mathcal{H}$ =

m_I' \ m_I	$\frac{3}{2}$	$\frac{1}{2}$	$-\frac{1}{2}$	$-\frac{3}{2}$	$\frac{1}{2}$	$-\frac{1}{2}$
$\frac{3}{2}$	A(1)	A(2)	A(4)	A(7)		
$\frac{1}{2}$		A(3)	A(5)	A(8)		
$-\frac{1}{2}$			A(6)	A(9)		
$-\frac{3}{2}$				A(10)		
$\frac{1}{2}$					A(15)	A(20)
$-\frac{1}{2}$						A(21)

where

A(1) = 0.101565*CC*EFG2

A(2) = 0.0586385*DD

A(3) = 0.033855*CC-EFG2

A(4) = 0.57735*EFG2*ETA

A(5) = 0.06771*DD

A(6) = -0.033855*CC-EFG2

A(8) = A(4)

A(9) = A(2)

A(10) = -0.101565*CC + EFG2

A(15) = -0.05924*CC

A(20) = -0.05924*DD

A(21) = -A(15)

with

```
EFG2 = EFG/2.0
CC = FIELD*COS(THETA)
```

and

```
DD = FIELD*SIN(THETA).
```

APPENDIX B

PROGRAM TO CALCULATE X-RAY DIFFRACTION LINE POSITIONS

This Fortran program calculates the X-ray diffraction line positions for a pyrite-type crystal. The systematic absence rule for this structure is: reflection absent if h,k or ℓ odd and the reflecting planes have indices (hk0),(h0ℓ) or (0kℓ)[4].

```
C      PROGRAM TO CALCULATE PYRITE STRUCTURE X-RAY DIFFRACTION
C      LINE POSITION
C      TWOTHE IS THE ANGLE TWICE THETA IN DEGREES
C      SINTHE IS THE SIN OF THETA IN RADIANS
C      H,K AND L ARE THE MILLER INDICES.
C      A AND LAMBDA (ANGSTROM); LATTICE PARAMETER AND
C      WAVELENGTH OF RADIATION RESPECTIVELY.
       DIMENSION TWOTHE(63),SINTHE(63)
       INTEGER H(63),K(63),L(63)
       REAL LAMBDA
       DATA H/1,5*2,3,2,2*3,4,2*3,2*4,3,3*4,5,4,5,3*4,5,2*6,5,2*6,
      12*5,3*6,4,6,5,7,4*6,2*7,2*6,8,6,8,7,2*8,3*6,8,7,6,7,2*8/
       DATA K/1,0,2*1,2*2,1,3*2,0,2,3,2*2,3,2,2*3,1,3,2,2*4,2*3,0,1,3,
      12*2,4,3,2,2*3,4,3,4,1,2*4,3,4,2,3,2*5,0,5,1,3,2*2,5,2*6,3,3*5,2*4/
       DATA L/1,2*0,1,0,2*1,2,0,1,0,2,1,0,1,2*2,0,2*1,2,1,0,1,3,1,2*0,2,
      10,2*1,3,2,0,1,4,2,3,1,0,1,3,2*2,1,0,1,0,2,1,3,0,1,3,0,3*1,4,2,0,1/
  500 READ(5,501,END=506)A,LAMBDA,TITLE
  501 FORMAT(F6.4,5X,F7.5,5X,6A5)
       WRITE(6,502)TITLE
  502 FORMAT(1H0,6A5/)
       WRITE (6,*/) A,LAMBDA
       DO 503 J=1,63
       SINTHE(J)=LAMBDA*SQRT( H(J)**2+K(J)**2+L(J)**2)/(2*A)
       IF(SINTHE(J).GT.1.0)SINTHE(J)=1.0
  503 TWOTHE(J)=(2.0*180.0/3.14159)*ARSIN(SINTHE(J))
       WRITE(6,504)
  504 FORMAT(1X,'TWOTHE',5X,'SINTHE',5X,'H',5X,'K',5X,'L'/)
       WRITE(6,505) ((TWOTHE(J),SINTHE(J),H(J),K(J),L(J)), J=1,63)
  505 FORMAT(1X,F8.4,3X,F6.4,3I6/)
       GO TO 500
  506 STOP
       END
```

APPENDIX C

PROGRAM TO CALCULATE TEMPERATURE DEPENDENCE OF THE HYPERFINE MAGNETIC FIELD AND ITS DIRECTION

This appendix contains a listing of the Fortran program used to calculate the temperature dependence of the hyperfine magnetic field using a Brillouin function with $S = \frac{5}{2}$. The reduced magnetisation σ can be written as

$$\sigma = B_S\left(\frac{3S}{S+1} \cdot \frac{\sigma}{\tau}\right) \qquad \text{(C.1)}$$

where

$$\tau = \frac{T}{T_N} \text{ , reduced temperature}$$

and B_S is called the function[50]

$$B_S'(x) = \frac{2S+1}{2S} \coth\left(\frac{2S+1}{2S} x\right) - \frac{1}{2S} \coth\left(\frac{x}{2S}\right)$$

Eqn. (C.1) can be written as

$$\sigma = B_S\left(\frac{2.142857}{\tau}\sigma\right)$$

or

$$x = A_x B_S(x)$$

where

$$x = \frac{2.142857}{\tau}\,\sigma$$

and

$$A_x = 2.142857 \frac{T_N}{T}$$

In this program subroutine SYMVEC[48] was used to find eigenvalues and eigenvectors of a 15 x 15 real symmetric matrix.

```
 $SET AUTOBIND LINEINFO RESET FREE
 $BIND = FROM CODE/SYMVEC
FILE  5(KIND=REMOTE)
FILE  6(KIND=REMOTE,MAXRECSIZE=22)
FILE  10(KIND=REMOTE)
C     THIS PROGRAM CALCULATES THE TEMPERATURE DEPENDENCE
C     OF THE HYPERFINE MAGNETIC FIELD AND ITS DIRECTION.
      DIMENSION A(15,15),V(15,15),VALUES(15),DX(15),DZ(15)
      REAL LX(15),LZ(15),SX(15),SZ(15)
      DATA II/0.0/
C     READ INPUT PARAMETERS:
C     THETA:EXCHANGE ANGLE IN DEGREES
C     TEMP:TEMPERATURE IN DEGREE KELVIN
C     TN:NEEL TEMPERATURE OR TB OF THE SAMPLE IN K.
C     HC:CONTACT-TERM EFFECTIVE FIELD FOR FERROUS ION IN TESLA.
C     R3:EXPECTATION VALUE R**(-3) OF THE 3D6 ELECTRON IN A.U.
C     DEL:TRIGONAL FIELD SPLITTING PARAMETER IN PER CM.
C     ZETA:SPIN-ORBIT INTERACTION PARAMETER IN PER CM.
C     EXCH:EXCHANGE FIELD PRODUCED BY NEIGHBORING
C     CATIONS IN PER CM.
  800 WRITE(10,100,END=900)
  100 FORMAT(' WRITE THETA')
      READ(5,/,END=900)THETA
      WRITE(10,200)
  200 FORMAT(' WRITE TEMP')
      READ(5,/)TEMP
      WRITE(10,350)
  350 FORMAT(' WRITE TN')
      READ(5,/)TN
      WRITE(10,299)
  299 FORMAT(' WRITE HC')
      READ(5,/)HC
      WRITE(10,400)
  400 FORMAT(' WRITE R3')
      READ(5,/)R3
      WRITE(10,500)
  500 FORMAT(' WRITE DEL')
      READ(5,/)DEL
      WRITE(10,600)
  600 FORMAT(' WRITE ZETA')
      READ(5,/)ZETA
      WRITE(10,700)
  700 FORMAT(' WRITE EXCH')
      READ(5,/)EXCH
      WRITE(6,*/)THETA,TEMP,HC,R3,DEL,ZETA,EXCH
C     BRILLOUIN FUNCTION CALCULATION
      IF(TEMP.LT.TN) GO TO 240
      BS=0.0
      GO TO 300
  240 AX=2.142857*TN/TEMP
      X=0.5*AX
C     LL COUNTS THE ITERATIONS
      LL=0.0
  250 XA=X/AX
      LL=LL+1
      IF(LL.GT.100) GO TO 260
      BS=1.2/(TANH(1.2*X))-0.2/(TANH(0.2*X))
      IF(ABS((XA-BS)/XA).LE.0.002) GO TO 300
      X=AX*BS
      GO TO 250
  260 WRITE(6,270)
```

```
  270 FORMAT(' TOO MANY ITERATIONS')
  300 CONTINUE
      EXCH=EXCH*B5
      THETA=THETA*ARCOS(-1)/180.0
      B=0.666667*DEL
      BB=0.353553*ZETA
      C=EXCH*COS(THETA)
      D=0.5*ZETA
      S=EXCH*SIN(THETA)
      CC=0.25*ZETA
      SS=0.433013*ZETA
      DD=-2.0*C
      A(6,3)=1.22474*S
      A(6,6)=0.333333*DEL
      A(1,1)=DD+A(6,6)+D
      A(2,2)=DD-B
      A(3,1)=S
      A(3,2)=BB
      A(3,3)=-C+A(6,6)+CC
      A(4,4)=DD+A(6,6)-D
      A(5,2)=S
      A(5,4)=A(3,2)
      A(5,5)=-C-B
      A(6,5)=SS
      A(7,6)=A(6,3)
      A(7,7)=C+A(6,6)-CC
      A(8,5)=A(6,3)
      A(8,7)=A(6,5)
      A(8,8)=-B
      A(9,4)=S
      A(9,8)=A(6,5)
      A(9,9)=-C+A(6,6)-CC
      A(10,7)=S
      A(10,10)=-DD+A(6,6)-D
      A(11,8)=A(6,3)
      A(11,10)=A(3,2)
      A(11,11)=C-B
      A(12,9)=A(6,3)
      A(12,11)=A(6,5)
      A(12,12)=A(6,6)
      A(13,11)=S
      A(13,13)=-DD-B
      A(14,12)=A(6,3)
      A(14,13)=A(3,2)
      A(14,14)=C+A(6,6)+CC
      A(15,14)=S
      A(15,15)=-DD+A(6,6)+D
      IF(II.EQ.0.0) GO TO 22
      WRITE(6,19)
   19 FORMAT(/' INPUT ARRAY ELEMENTS:')
      DO 20 I=1,15
      DO 20 J=1,15
   20 IF(A(I,J).NE.0)WRITE(6,21)I,J,A(I,J)
   21 FORMAT(1X,'A(',I2,',',I2,') = ',G13.6)
   22 CALL SYMVEC(15,15,A,VALUES,V)
      DO 30 I=1,15
   30 WRITE(6,31)I,VALUES(I),(V(J,I),J=1,15)
   31 FORMAT(/' EIGENVALUE',I3,'=',G13.6,
     1'AND HAS EIGENVECTOR : ',3(/,5(1X,G13.6)))
C     TEMPERATURE DEPENDENCE OF THE EXPECTATION VALUE
   32 Z=1.414214
      ZA=2.828427
```

```
      AA=0.707107
      E=2.449489
      EE=1.224745
      Y=1.73205
      YY=57.2957795
      YA=3.464102
      P=12.5169*R3
      PP=0.447032*R3
      Q=3.674235
      FF=1.788129*R3
      ZZ=0.695008*TEMP
      ELX=0.0
      ELZ=0.0
      ESX=0.0
      ESZ=0.0
C     BLINE IS THE SUM OF THE PARTITION FUNCTION
      BLINE=0.0
      DO 50 J=1,15
      EXPON=EXP(-VALUES(J)/ZZ)
      LX(J)=-AA*(V(1,J)*V(2,J)+V(2,J)*(V(1,J)+V(4,J))+V(3,J)*V(5,J)
     1+V(4,J)*V(2,J)+V(5,J)*(V(3,J)+V(9,J))+V(6,J)*V(8,J)+V(7,J)*
     2V(11,J)+V(8,J)*(V(6,J)+V(12,J))+V(9,J)*V(5,J)+V(10,J)*V(13,J)+
     3V(11,J)*(V(7,J)+V(14,J))+V(12,J)*V(8,J)+V(13,J)*(V(10,J)+
     4V(15,J))+V(14,J)*V(11,J)+V(15,J)*V(13,J))
      ELX=ELX+LX(J)*EXPON
      LZ(J)=V(1,J)**2+V(3,J)**2-V(4,J)**2+V(6,J)**2+V(7,J)**2-
     1V(9,J)**2+V(10,J)**2-V(12,J)**2-V(14,J)**2-V(15,J)**2
      ELZ=ELZ+LZ(J)*EXPON
      SX(J)=V(1,J)*V(3,J)+V(2,J)*V(5,J)+V(3,J)*(V(1,J)+EE*V(6,J))
     1+V(4,J)*V(9,J)+V(5,J)*(V(2,J)+EE*V(8,J))+EE*V(6,J)
     2*(V(3,J)+V(7,J))+V(7,J)*(EE*V(6,J)+V(10,J))+EE*
     3V(8,J)*(V(5,J)+V(11,J))+V(9,J)*(V(4,J)+EE*V(12,J))+
     4V(10,J)*V(7,J)+V(11,J)*(EE*V(8,J)+V(13,J))+
     5EE*V(12,J)*(V(9,J)+V(14,J))+V(13,J)*V(11,J)+V(14,J)*
     6(EE*V(12,J)+V(15,J))+V(15,J)*V(14,J)
      ESX=ESX+SX(J)*EXPON
      SZ(J)=-(V(1,J)**2)*2.0-(V(2,J)**2)*2.0-V(3,J)**2-(V(4,J)**2)*2.0
     1-V(5,J)**2+V(7,J)**2-V(9,J)**2+(V(10,J)**2)*2.0+V(11,J)**2+
     2(V(13,J)**2)*2.0+V(14,J)**2+(V(15,J)**2)*2.0
      ESZ=ESZ+SZ(J)*EXPON
   50 BLINE=BLINE+EXPON
      ELX=ELX/BLINE
      ELZ=ELZ/BLINE
      ESX=ESX/BLINE
      ESZ=ESZ/BLINE
C     HLX,HLZ ARE X & Z COMP OF ORBITAL FIELD
C     HL IS THE ORBITAL FIELD
      HLX=P*ELX
      HLZ=P*ELZ
      HL=SQRT(HLX**2+HLZ**2)
      IF(HLZ.EQ.0.0)GO TO 130
      THEHL=YY*ATAN(HLX/HLZ)
  130 THEHL=90.0
      HDX=0.0
      HDZ=0.0
      DO 60 J=1,15
      EXPON=EXP(-VALUES(J)/ZZ)
      DX(J)=2.0*PP*(V(1,J)*(-Z*V(2,J)+3.0*V(3,J)
     1+4.0*Z*V(4,J)+4.0*V(5,J))
     2+V(2,J)*(Z*V(4,J)+6.0*V(5,J)-4.0*V(9,J))
     3+V(3,J)*(2.0*V(4,J)-AA*V(5,J)+Q*V(6,J)
```

```
     4+2.0*E*V(8,J)+ZA*V(9,J))
     1+3.0*V(4,J)*V(9,J)
     5+V(5,J)*(3.0*E*V(8,J)+AA*V(9,J)
     6-2.0*E*V(12,J))
     7+V(6,J)*(Q*V(7,J)+E*V(9,J)+2.0*E*V(11,J))
     8+V(7,J)*(3.0*V(10,J)+AA*V(11,J)+E*V(12,J)
     9+4.0*V(13,J)-ZA*V(14,J))
     1+V(8,J)*(3.0*E*V(11,J)-2.0*E*V(14,J))
     2+V(9,J)*Q*V(12,J)
     3+V(10,J)*(Z*V(13,J)+2.0*V(14,J)-4.0*Z*V(15,J))
     4+V(11,J)*(6.0*V(13,J)-AA*V(14,J)-4.0*V(15,J))
     5+V(12,J)*Q*V(14,J)
     6-Z*V(13,J)*V(15,J)
     7+3.0*V(14,J)*V(15,J))-FF*SX(J)
      DZ(J)=PP*(V(1,J)*(-12.0*V(1,J)-8.0*Z*V(9,J))
     1+V(2,J)*ZA*V(3,J)
     2-V(3,J)*(6.0*V(3,J)+8.0*Y*V(12,J))
     3-V(4,J)*(12.0*V(4,J)+ZA*V(5,J))
     4+V(5,J)*YA*V(6,J)
     5-V(6,J)*8.0*Y*V(14,J)
     6+V(7,J)*(6.0*V(7,J)+YA*V(8,J)-8.0*Z*V(15,J))
     7-V(8,J)*YA*V(9,J)
     8-(V(9,J)**2)*6.0
     9+V(10,J)*(12.0*V(10,J)+ZA*V(11,J))
     1-V(11,J)*YA*V(12,J)
     2-V(13,J)*ZA*V(14,J)
     3+(V(14,J)**2)*6.0
     4+(V(15,J)**2)*12.0)-FF*SZ(J)
C      HDX,HDZ ARE THE X & Z COMP OF THE DIPOLAR FIELD
C      HD IS THE DIPOLAR FIELD
       HDX=HDX+DX(J)*EXPON
   60  HDZ=HDZ+DZ(J)*EXPON
       HDX=HDX/BLINE
       HDZ=HDZ/BLINE
       HD=SQRT(HDX**2+HDZ**2)
       IF(HDZ.EQ.0.0)GO TO 140
       THEHD=YY*ATAN(HDX/HDZ)
  140  THEHD=90.0
C      HSX,HSZ ARE X & Z COMP OF FERMI CONTACT FIELD
C      HS:FERMI CONTACT FIELD
       HSX=0.5*HC*ESX
       HSZ=0.5*HC*ESZ
       HS=SQRT(HSX**2+HSZ**2)
       IF(HSZ.EQ.0.0)GO TO 150
       THEHS=YY*ATAN(HSX/HSZ)
  150  THEHS=90.0
C      HX,HZ ARE THE X & Z COMP OF HYPERFINE FIELD
C      HHF IS THE HYPERFINE FIELD
C      THEHF IS THE HYPERFINE ANGLE
       HX=HLX+HDX+HSX
       HZ=HLZ+HDZ+HSZ
       HHF=SQRT(HX**2+HZ**2)
       IF(HZ.EQ.0.0)GO TO 160
       THEHF=YY*ATAN(HX/HZ)
       GO TO 204
  160  THEHF=90.0
  204  WRITE(6,*/)HHF,THEHF,HX,HZ
       GO TO 800
  900  STOP
       END
```

APPENDIX D

RELATIONS BETWEEN THE EXCHANGE PARAMETER AND THE EXCHANGE CONSTANTS J_1 AND J_2

The molecular field (Heisenberg) model for the exchange interactions between the spins S_i and its neighbours S_{Fe} can be written as

$$\mathcal{H}_{ex} = -2J \sum_i \underline{S}_i \cdot \underline{S}_{Fe}$$

where J is the exchange integral. The sum can be divided into nearest neighbour (J_1) and second nearest neighbour (J_2) contributions, and rearranged as

$$\mathcal{H}_{ex} = -2J_1 \sum_{nn} \underline{S}_i \cdot \underline{S}_{Fe} - 2J_2 \sum_{2nn} \underline{S}_i \cdot \underline{S}_{Fe}$$

$$= (-2J_1 \sum_{nn} \underline{S}_i - 2J_2 \sum_{2nn} \underline{S}_i) \cdot \underline{S}_{Fe}$$

where

$$\underline{S}_i = \langle S_i \rangle \underline{M}_i = \sqrt{\tfrac{5}{2} \cdot \tfrac{7}{2}}\, B_S(T) \underline{M}_i \quad \text{(i.e. } \sqrt{S(S+1)}\, B_S(T) \underline{M}_i\text{)}$$

and

$\underline{M}_i$ = a unit vector in the direction of the ith spin

and

$B_S(T)$ = Brillouin function.

MnS_2

Nearest neighbour (nn) are 4 parallel and 8 antiparallel to spin axis. Let spin axis direction at Fe site be given

by $\underline{M}$ (a unit vector)

$$\therefore \quad \underline{M}_i = +\underline{M} \text{ for 4nn's and } -\underline{M} \text{ for 8nn's}$$

$$\therefore -2J_1 \sum_{nn} \underline{S}_i = -2J_1 \frac{\sqrt{35}}{2} B_s(T) \quad (4\underline{M} - 8\underline{M})$$

$$= 4\sqrt{35}\ J_1\ B_s(T)\underline{M}$$

Second nearest neighbour (2nn) are 4 parallel and 2 antiparallel, giving

$$-2J_2 \sum_{2nn} \underline{S}_i = -2\sqrt{35}\ J_2\ B_s(T)\underline{M}$$

So exchange field

$$H_{ex} = 4\sqrt{35}\ B_s(T)\,(J_1 - \tfrac{1}{2}J_2)\,\underline{M}.\underline{S}_{Fe}$$

$\underline{M}$ was assumed in xz plane

$$\therefore \underline{M}.\underline{S}_{Fe} = S_z \cos\theta_{ex} + S_x \sin\theta_{ex}$$

where θ_{ex} is the exchange angle

$$H_{ex} = 4\sqrt{35}\ B_S(T)\,(J_1 - \tfrac{1}{2}J_2)\,(S_z \cos\theta_{ex} + S_x \sin\theta_{ex})$$

The program (listed in Appendix C) used

$$H_{ex} = J'\langle S_i \rangle B_s(T)\ (S_z \cos\theta_{ex} + S_x \sin\theta_{ex})$$

so for MnS_2

$$J'\langle S_i\rangle = 4\sqrt{35}\ (J_1 - \frac{1}{2} J_2)$$

<u>$MnSe_2$ 2% ^{57}Fe</u>

<u>Site I</u>: <u>nn</u> same as in MnS_2,

<u>2nn</u> are 5 parallel, 1 antiparallel

$$\therefore -2 J_2 \sum_{2nn} \underline{S_i} = -4\sqrt{35}\ J_2\ B_s(T)\underline{M}$$

and

$$H_{ex} = 4\sqrt{35}\ B_s(T)(J_1 - J_2)(S_z \cos\theta_{ex} + S_x \sin\theta_{ex})$$

gives

$$J'\langle S_i\rangle = 4\sqrt{35}\ (J_1 - J_2)$$

<u>Site II</u>: $J'\langle S_i\rangle$ same as in MnS_2, i.e.

$$J'\langle S_i\rangle = 4\sqrt{35}\ (J_1 - \frac{1}{2} J_2)$$

using the observed values of $J'\langle S_i\rangle$ (for both sites), it is possible to determine J_1 and J_2 from two equations,

$$-75 = 4\sqrt{35}\ (J_1 - J_2)$$

$$-100 = 4\sqrt{35}\ (J_1 - \frac{1}{2} J_2)$$

i.e.

$$J_1/k = -7.6K$$

$$J_2/k = -3.04K$$

so

$$J_1 = 2.5\ J_2$$

$\underline{MnTe_2}$

The spin arrangement is:

nn: 4 along $[1\bar{1}\bar{1}]$, 4 along $[\bar{1}1\bar{1}]$ and 4 along $[\bar{1}\bar{1}1]$

(with respect to the cubic axes).

Along these directions unit vectors can be written as

$$\frac{1}{\sqrt{3}}(1,\bar{1},\bar{1}),\ \frac{1}{\sqrt{3}}(\bar{1},1,\bar{1})\ \&\ \frac{1}{\sqrt{3}}(\bar{1},\bar{1},1) \quad \text{respectively,}$$

$$\therefore\ -2J_1 \sum_{nn} \underline{S}_i = -\sqrt{35}\ J_1\ B_s(T) \sum_{nn} \underline{M}_i = -\sqrt{35}\ J_1\ B_s(T)\left(-\frac{4}{\sqrt{3}}\right)(1,1,1)$$

$$\therefore \text{ nn term in } H_{ex} = 4\sqrt{35}\ J_1\ B_s(T)\ \frac{(1,1,1)}{\sqrt{3}}$$

2nn: All spins are parallel, so this equals

$$-2\ J_2 \sum_{2nn} \underline{S}_i = -2\ \frac{\sqrt{35}}{2}\ J_2\ B_s(T) \sum_{2nn} \underline{M}_i$$

$$= -6\sqrt{35}\ J_2\ B_s(T)\ \frac{(1,1,1)}{\sqrt{3}}$$

$$\therefore H_{ex} = 4\sqrt{35}\ B_s(T)(J_1 - 1.5\ J_2)S_z$$

(no S_x term since the axis is along z i.e. [111])

Thus

$$J'\langle S_i\rangle = 4\sqrt{35}\ (J_1 - 1.5\ J_2)\ .$$

REFERENCES

1. J.M. Hastings, N. Elliott and L.M. Corliss, Phys. Rev. 115 13 (1959).

2. M. Pasternak and A.L. Spijkervet, Phys. Rev. 181 574 (1969).

3. J.M. Hastings, L.M. Corliss, M. Blume and M. Pasternak, Phys. Rev. B1 3209 (1970).

4. N. Elliott, J. Am. Chem. Soc. 59 1958 (1937).

5. J.S. Smart, "Effective Field Theories of Magnetism", Saunders, Philadelphia and London (1966) Chapter 8.

6. Y. Nishihara and S. Ogawa, Int. Conf. on the Application of the Mössbauer effect, Kyoto, Japan (1978).

7. E.F. Westrum Jr. and F. Gronvold, J. Chem. Phys. 52 3820 (1970).

8. J.M. Hastings and L.M. Corliss, Phys. Rev. B14 1995 (1976).

9. M.S. Lin and H. Hacker Jr. Solid State Commun. 6 687 (1968).

10. H. Itoh and S. Miyahara, J. Phys. Soc. Japan 42 469 (1977).

11. L.M. Corliss and J.M. Hastings, J. Phys. (Paris) 25 557 (1964).

12. A. Sawaoka and S. Miyahara, J. Phys. Soc. Japan 20 2087 (1965).

13. M. Pasternak, Phys. Rev. 184 523 (1969).

14. O. Okada and T. Miyadai, J. Phys. Soc. Japan 43 343 (1977).

15. G. van Kalkeren, R. Block and L. Jansen, Physica 85B 259(1977) and 93B 195 (1978).

16. O. Okada, J. Phys. Soc. Japan 48 391 (1980).

17. R.L. Mössbauer, Zeitscrift fur Physik 151 124 (1958) and Naturwissenschaften 45 538 (1958).

18. N.N. Greenwood and T.C. Gibb, "Mössbauer Spectroscopy", Chapman and Hall (1971).

19. G.M. Bancroft, "Mössbauer Spectroscopy: An Introduction for Inorganic Chemists and Geochemists", McGraw Hill (1973).

20. G.K. Wertheim, "Mössbauer Effect: Principle and Application", Academic Press Inc. (1964).

21. L. May, "An Introduction to Mössbauer Spectroscopy" Plenum Press (1971).

22. U. Gonser, "Mössbauer Spectroscopy", Springer-Verlag (1975).

23. H. Frauenfelder, "The Mössbauer Effect", W.A. Benjamin Inc. (1962).

24. V.I. Goldanski and R.H. Herber; "Chemical Application of Mössbauer Spectroscopy", Academic Press N.Y. (1968).

25. W. Kundig, Nucl. Instrum. Methods, 48 219 (1967).

26. H.N. Ok and J.G. Mullen, Phys. Rev. 168 563 (1968).

27. D.C. Price, I. Maartense and A.H. Morrish, Phys. Rev. B9 281 (1974).

28. R. Ingalls, Phys. Rev. 133 A787 (1964).

29. B. Bleaney and K.W.H. Stevens, Rep. Prog. Phys. 16 108 (1953).

30. C.E. Johnson, Proc. Phys. Soc. London 92 748 (1967).

31. Y. Hazony, Phys. Rev. B3 711 (1971).

32. R.E. Watson and A.J. Freeman, Phys. Rev. 123 2027 (1961).

33. M.F. Bent, B.I. Persson and D.G. Agresti, Comput. Phys. Commun. 1 67 (1969).

34. L.L. Sparks, R.L. Powell and W.L. Hall, "Cryogenic Thermocouple Tables", NBS Report 9712 (1968).

35. National Bureau of Standards, Certificate of Calibration- Iron Foil Mössbauer Standard 1541 (1972).

36. C.B. Bargeron, M. Avinor and H.G. Drickamer, Inorg. Chem. 10 1338 (1971).

37. S. Furuseth and A. Kjekshus, Acta Chem. Scand. 19 1405 (1965).

38. W. Blitz and F. Wiechman, Z. Anorg. Allg. Chem. 228 268 (1936).

39. M. Avinor and G. DePasquali, J. Inorg. Nucl. Chem. 32 3404 (1970).

40. S. Furberg, Acta Chem. Scand. 7 693 (1953).

41. Written by R.J. Pollard, Department of Physics, University of Canterbury (1981).

42. P.A. Montana and M.S. Seehra, Solid State Commun. 20 897 (1976).

43. V.K. Garg, Y.S. Liu and S.P. Puri, J. Appl. Phys. 45 70 (1974).

44. A.A. Temperley and H.W. Lefevre, J. Phys. Chem. Solids 27 85 (1966).

45. J. van Dongen Torman, R. Jagannathan and J.M. Trooster, Hyper. Inter. 1 135 (1975).

46. G.K. Wertheim, D.N.E. Buchanan and H.J. Guggenheim, Phys. Rev. B2 1392 (1970).

47. J.D. Siegwarth, Phys. Rev. 155 285 (1967).

48. Burroughs Corporation, U.S.A. AA345998 (1972).

49. L.R. Walker, G.K. Wertheim and V. Jaccarino, Phys. Rev. Lett. 68 98 (1961).

50. T.C. Gibb, "Principles of Mössbauer Spectroscopy", Chapman and Hall, London (1976) P112.